

AD-A093 888

HONEYWELL SYSTEMS AND RESEARCH CENTER MINNEAPOLIS MN

F/G 1/3

TWO-AXIS, FLUIDICALLY CONTROLLED THRUST VECTOR CONTROL SYSTEM F--ETC(U)

JUL 80 R B BEALE, R V BURTON, N E MILLER

F33615-76-C-3070

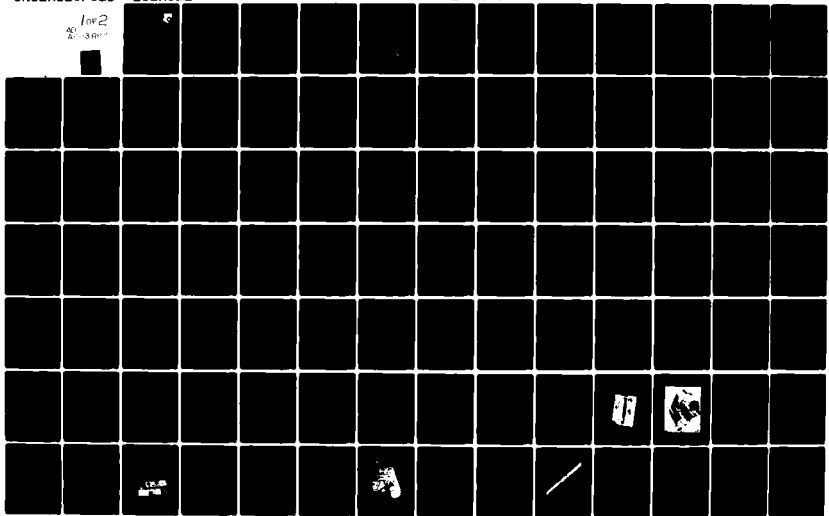
UNCLASSIFIED

805RC22

AFWAL-TR-80-3080

NL

10x2  
20x30mm



**LEVEL II**

2  
b.s.

AFWAL-TR-80-3080



**TWO-AXIS, FLUIDICALLY CONTROLLED  
THRUST VECTOR CONTROL SYSTEM  
FOR AN EJECTION SEAT**

R.B. Beale  
R.V. Burton  
N.E. Miller

Honeywell Systems and Research Center  
2600 Ridgway Parkway  
Minneapolis, Minnesota 55413

July 1980

TECHNICAL REPORT AFWAL-TR-80-3080  
Final report for Period 1 April 1976 to 1 October 1979

Approved for public release; distribution unlimited

FLIGHT DYNAMICS LABORATORY  
AIR FORCE WRIGHT AERONAUTICAL LABORATORIES  
AIR FORCE SYSTEMS COMMAND  
WRIGHT-PATTERSON AIR FORCE BASE, OHIO 45433

DDIC  
JAN 19 1981  
C

AD A093888

DDC FILE COPY

81 1 19 022

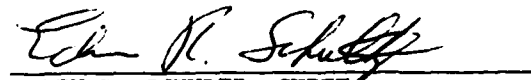
NOTICE

When Government drawings, specification, or other data are used for any purpose other than in connection with a definitely related Government procurement operation, the United States Government thereby incurs no responsibility nor any obligation whatsoever; and the fact that the government may have formulated, furnished, or in any way supplied the said drawings, specifications, or other data, is not to be regarded by implication or otherwise as in any manner licensing the holder or any other person or corporation, or conveying any rights or permission to manufacture use, or sell any patented invention that may in any way be related thereto.

This report has been reviewed by the Office of Public Affairs (ASD/PA) and is releasable to the National Technical Information Service (NTIS). At NTIS, it will be available to the general public including foreign nations.

This technical report has been reviewed and is approved for publication.

  
MARVIN C. WHITNEY  
Project Engineer

  
EDWIN R. SCHULTZ, CHIEF  
Crew Escape & Subsystems Branch  
Vehicle Equipment Division

FOR THE COMMANDER

  
AMBROSE B. NUTT  
Director  
Vehicle Equipment Division

"If your address has changed, if you wish to be removed from our mailing list or if the addressee is no longer employed by your organization please notify AFWAL/FIER, W-PAFB, OH 45433 to help us maintain a current mailing list."

Copies of this report should not be returned unless return is required by security considerations, contractual obligations, or notice on a specific document.

19 REPORT DOCUMENTATION PAGE		READ INSTRUCTIONS BEFORE COMPLETING FORM	
1. REPORT NUMBER	2. GOVT ACCESSION NO.	3. RECIPIENT'S CATALOG NUMBER	
18 AFWAL TR-80-3080 1 ✓	AD-A093 888		
4. TITLE (and Subtitle)		5. TYPE OF REPORT & PERIOD COVERED	
9 Two-Axis, Fluidically Controlled Thrust Vector Control System for an Ejection Seat		Final Report 1 April 76 - 1 October 79	
7. AUTHOR(s)		14 PERFORMING ORG. REPORT NUMBER	
R. B. Beale, R. V. Burton, N. E. Miller		80SRC22 ✓	
9. PERFORMING ORGANIZATION NAME AND ADDRESS		8. CONTRACT OR GRANT NUMBER(s)	
Honeywell Systems and Research Center 2600 Ridgway Parkway Minneapolis, Minnesota 55413		F33615-76-C-3070 ✓	
11. CONTROLLING OFFICE NAME AND ADDRESS		10. PROGRAM ELEMENT, PROJECT, TASK AREA & WORK UNIT NUMBERS	
Flight Dynamics Laboratory (AFWAL/FIER) AF Wright Aeronautical Laboratories, AFSC Wright-Patterson Air Force Base, Ohio 45433		16 2402/03 01 117-1	
14. MONITORING AGENCY NAME & ADDRESS (if different from Controlling Office)		12. REPORT DATE	
AFWAL/FIER Wright-Patterson Air Force Base, Ohio 45433		11 Jul 1980	
16. DISTRIBUTION STATEMENT (of this Report)		13. NUMBER OF PAGES	
Approved for public release; distribution unlimited		150	
17. DISTRIBUTION STATEMENT (of the abstract entered in Block 20, if different from Report)		15. SECURITY CLASS. (of this report)	
		Unclassified	
18. SUPPLEMENTARY NOTES		15a. DECLASSIFICATION DOWNGRADING SCHEDULE	
19. KEY WORDS (Continue on reverse side if necessary and identify by block number)			
Ejection Seat	Trajectory	TVC	Simulator
Stabilization	Parachute	Nozzle	Ball & Socket
Fluidic	Simulation	Actuator	Friction
Vortex	Thrust Vector	Servo valve	Servo Table
Rate Sensor	Control		Rate Table
20. ABSTRACT (Continue on reverse side if necessary and identify by block number)			
A two-axis, hydrofluidic, thrust vector control (TVC) system was designed to stabilize an ejection seat during the critical rocket burn portion of the trajectory which should reduce the g loads on the crewmember and result in higher trajectories. The dynamic performance of a seat with a fluidic TVC system was analytically evaluated against established ejection seat requirements and physiological limits. This analysis showed that pitch rates were reduced by 60 percent and yaw rates by 90 percent when			

compared with a seat with no stabilizing system. Breadboard hardware was fabricated and tested with the components meeting requirements. A prototype integrated fluidic circuit and a moveable nozzle was then designed, fabricated and tested. The prototype system did not meet all the requirements due to a null bias instability in the fluidic amplifier which was caused by a nozzle asymmetry in the fluidic amplifier mold.

The FTVC System included a vortex rate sensor, fluidic lag-lead compensator, and a four-stage fluidic servovalve. These components will use hot gas pressurized oil to drive a hydrostatically supported, piston actuated ball and socket nozzle with 20 deg of deflection of a 3500 lb thrust rocket. Initial nozzle breakaway friction was 170 in-lb. Operating stiction was 135 in-lb and running friction was 80 in-lb.

A digitally controlled hydraulic servotable was built to simulate ejection seat trajectories. It performed with  $1/3^\circ$  accuracy, 16 Hz bandwidth, and 447 ft-lb torque.

FOREWORD

This report describes the work performed by the Honeywell Systems and Research Center, Minneapolis, Minnesota on a fluidically controlled, thrust vector control system for an ejection seat. This work was sponsored by the Flight Dynamics Laboratory, Air Force Wright Aeronautical Laboratories, Air Force Systems Command, Wright-Patterson Air Force Base, Ohio. Work was authorized under Contract F33615-76-C-3070, Project No. 2402, Task No. 240203. Marvin C. Whitney of the Crew Escape and Subsystems Branch, AFWAL/FIER, was the Air Force Program Manager. This research work is part of an effort to stabilize an ejection seat during rocket burning in both the pitch and yaw axes. The period covered is from 1 April 1976 to 1 October 1979 and the report was submitted on 27 May 1980.

Robert B. Beale served as the Principal Investigator for the technical work and was assisted by Robert V. Burton and Norman E. Miller.

Accession For	
NTIS GRA&I	<input checked="" type="checkbox"/>
DTIC TAB	<input type="checkbox"/>
Unannounced	<input type="checkbox"/>
Justification	
By	
Distribution/	
Investigator/	
Date	

## DEFINITIONS

STAPAC--Vernier TVC in the pitch axis

Open Loop--Control system feedback disconnected, no TVC

Uncontrolled--No TVC

No TVC--Fixed rocket nozzle position

RMS--Root mean squared amplitude

DC Gain--Control system gain at very low frequency

## CONTENTS

Section		Page
1	INTRODUCTION	1
	Benefits of Two-Axis TVC	2
	Escape System Performance Results	3
	Component Description	8
2	ESCAPE SYSTEM REQUIREMENT ANALYSIS	11
	Baseline Design Performance	11
	Baseline Design Summary	11
	Comparison of TVC and the Uncontrolled Seat	18
	Comparison of TVC and STAPAC	25
	Component Design Requirements	29
	Design Analysis	36
	Summary of Design Analysis	36
	Low Speed System Design	41
	High Speed System Design	50
3	FTVC SYSTEM DESIGN AND TEST RESULTS	65
	System Description	65
	Fluidic Controller	72
	Description	72
	Test Results	75
	Fabrication	85
	Nozzle Servo System	88
	Description	88
	Test Results	90
	Design Analysis	99
	Hydraulic Power Supply	104
	Size Estimate	105
	Operating Fluid	105

Section		Page
4	ROCKET NOZZLE AND ACTUATOR DESIGN AND TEST	106
	Design and Performance Summary	106
	Bearing Friction Tests	107
	Hydrostatic Bearing Assembly	110
	Hydrostatic Bearing Design	112
	Hydrostatic Bearing Analysis	114
	Seal Pressure	114
	Bearing Friction	116
	Actuator Design	119
	Rocket Motor Design	119
5	ESCAPE SYSTEM FLIGHT SIMULATOR	126
	Simulator Description	126
	Escape System Simulation Description	129
	Precision Servo Table	130
	Digital Controller	135
6	CONCLUSIONS	136
	REFERENCES	137

## LIST OF ILLUSTRATIONS

Figure		Page
1a	Low Speed Altitude Trajectory	5
1b	Low Speed Pitch Rate History	5
1c	Low Speed Yaw Rate History	6
2a	High Speed Altitude Trajectory	6
2b	High Speed Pitch Rate History	7
2c	High Speed Yaw Rate History	7
3	Escape System TVC Assembly	9
4	Pitch Axis TVC System	17
5	Rocket Thrust Response	17
6	Comparison of TVC and the Uncontrolled Seat at 600 Knots	19
7	Comparison of TVC and the Uncontrolled Seat at 240 Knots	20
8	TVC and Open-Loop Performance at Zero Knots	22
9	TVC and Open-Loop Performance at 240 Knots, Mode I	23
10	TVC and STAPAC Performance at Zero Knots	27
11	TVC and STAPAC Comparison at High Speed	28
12	TVC and STAPAC Pitch Attitude History at 240 Knots, Mode I	30
13	Control System Frequency Response Requirement	32
14	Ejection Seat Linearized Pitch Axis Frequency Response at 600 Knots	34
15	Linearized Pitch Axis Frequency Response at Zero Knots	35
16	Rocket Thrust Time Responses	37
17	Seat Geometry	37
18	Effect of Pitch Attitude Bias at Zero Knots	42
19	Effect of Pitch Attitude Bias at 240 Knots, Mode I	43
20	Effect of Thrust Level at Zero Knots	46

Figure		Page
21	Effect of Thrust Level at 240 Knots, Mode I	48
22	Effect of Pitch Attitude Bias at 600 Knots	50
23	Effect of Pitch Attitude Bias at 240 Knots, Mode II	52
24	Effect of Thrust Level at 600 Knots	57
25	Effect of Thrust Level at 240 Knots, Mode II	59
26	Effect of Drogue Attach Point at 600 Knots	61
27	Effect of Drogue Attach Point at 240 Knots, Mode II	63
28	Assembled Attitude Controllers	66
29	Breadboard FTVC System	67
30	Single Axis FTVC Block Diagram	68
31	FTVC Design Goal Dynamic Response	68
32	Fluidic Attitude Control System Schematic	69
33	FTVC System Operating Schematic	70
34	Fluidic Controller Disassembled	72
35	One-Axis Fluidic Rate Sensor and Amplifier	73
36	Detail of Fluidic Attitude Controller	74
37	Controller Instrumented with Flow Meters and Valves for Impedance Matching	76
38	Controller Null Bias Stability	78
39	Vortex Rate Sensor Gain Factor (UTTAS Design)	79
40	Dynamic Response--Breadboard VRS/Controller	81
41	VRS/Controller Start-Up--Zero Rate Applied	82
42	Start-Up Transient Test Controller Turned on Before Rate Input	83
43	Start-Up Transient Test Controller Turned on After Rate Input	84
44	Mold and Wax Form of the Under Side of the Controller Circuit	86

Figure		Page
45	Mold and Wax Form of the Upper Side of the Controller Circuit	87
46	Block Diagram, Basic Hydrofluidic Servo	88
47	Schematic of Nozzle Hydrofluidic Servoactuator	90
48	Scale Factor--ACH104A1022 Hydrofluidic Servoactuator	92
49	Dynamic Response--ACH104A Hydrofluidic Servoactuator	93
50	Nozzle Servo Test Apparatus	94
51	Servocascade Test Apparatus	95
52	ACH 104 Servo Feedback Transducer Characteristic	96
53	Typical P-Q Envelope for a Fluid Power Amplifier (High Pressure Data)	97
54	P-Q Envelope for 24110024-00 Three-Stage Servocascade at 1500 psi Supply Pressure	98
55	Blocked Actuator Port Pressure Gain--24110024-001 Servocascade	98
56	P-Q Envelope for Four-Stage Actuator Power Fluid Amplifier	99
57	No-Load Flow Gain, Four-Stage Servocascade at 2000 psi Supply Pressure	100
58	Blocked Actuator Port Pressure Gain, Four-Stage Servocascade at 2000 psi Supply Pressure	101
59	Electroformed Four-Stage Servocascade	102
60	Estimated Dynamic Response--Hydrofluidic Servoactuator	104
61	Nozzle Bearing and Actuator Test Fixture	107
62	Hydrostatic Ball and Socket Nozzle with Hydraulic Actuators	108
63	Hydrostatic Bearing Test Fixture	109
64	Hydrostatic Bearing Friction Test	110
65	Nozzle Friction Test	111
66	Actuator Piston Seal Friction	111
67	Free-Body Diagram of Axial Forces	114

Figure		Page
68	Projected Axial Area Geometry	116
69	Friction Forces as a Function of Lubrication Pressure	117
70	Rocket Nozzle Actuator	120
71	Actuator Displacement Selection	121
72	Pressure and Thrust versus Time at Sea Level and 70°F	124
73	Propellant Weight and Total Impulse at 70°F versus Grain Length	125
74	Escape System Flight Simulator	127
75	Simulated Escape Test System Diagram	128
76	Pitch Attitude Trajectories	129
77	Yaw Attitude Trajectories	130
78	Hydraulic Rate Table for Fluidic Controller Tests	131
79	Hydraulic Rate Table Power and Control System	132
80	Hydraulic Power Supply	133
81	Table Frequency Response	134

## LIST OF TABLES

Table		Page
1	Escape System Performance Summary	4
2	Simulation Results	12
3	Control System Performance Requirements	14
4	Event Sequence	14
5	Simulated Seat Characteristics	15
6	Aeromedical Summary--600 Knots, 95th Percentile Pilot	26
7	Maximum g Loads--240 Knots, Mode I, 5th Percentile Pilot	30
8	Control System Requirements	31
9	Mode I Simulation Results, 5th Percentile Pilot	39
10	Comparison of Simplified and Complete Control Law Models	41
11	Thrust Effect on Acceleration Force (0 Knots, 5th Percentile Pilot)	48
12	Effect of Attitude Bias on Roll Attitude and Acceleration Forces (600 Knots, 5th Percentile Pilot)	54
13	Effect of Attitude Biases on Acceleration Forces (600 Knots, 5th Percentile Pilot)	55
14	FTVC System Operating Parameters	71
15	Procedure for Selecting Controller Orifices	77
16	Nozzle Servo Adjustments	96
17	Procedure for Assembling the Hydrostatic Bearing	113
18	Motor Performance Parameters (at Sea Level and 70°F)	121
19	General Specifications	122
20	Ballistics (at Sea Level)	123
21	Properties and Ballistics of TP-H8239 Type Propellant at 70°F	124
22	Precision Servo Table Performance Specifications	134

## SECTION 1

### INTRODUCTION

This report describes the design and bench test of a two-axis, hydrofluidic, thrust vectoring control (TVC) system for stabilizing ejection seats. This report is of greater detail than the previous report of the same subject.<sup>1</sup> The new SAFEST 6 DOF model<sup>2</sup> simulated escape system trajectories from 0 to 600 knots at all attitudes required in military specifications. The results show that the two-axis system reduces unsafe g loads by 30 percent compared to STAPAC<sup>3</sup> and 60 percent compared to a seat with no TVC. This reduction is the result of reducing maximum yaw angles by a factor of 10. Maximum pitch rates are also reduced by 30 and 60 percent at high speed. In all cases, the pitch and yaw rates are reduced to near zero at the onset of line stretch. This performance will have a significant impact on pilot injuries due to flailing, sideways g loads, and line entanglement.

This report also describes unique, compact attitude stabilization controllers and a hydraulically actuated nozzle. The controllers that have no moving parts are low in cost, require no maintenance, and obtain their power from the main rocket. The controller also contains a four-stage position servovalve which has no moving parts.

---

<sup>1</sup>R. B. Beale, "Fluidic Thrust Vector Control for the Stabilization of Man/Ejection Seat Systems," AFFDL-TR-75-105, Honeywell, Inc., Minneapolis, Minnesota, September 1975.

<sup>2</sup>I. L. Clinkenbeard and E. O. Cartwright, "Study and Design of an Ejection System for VTOL Aircraft," AFFDL-TR-70-1, Air Force Flight Dynamics Laboratory, Wright-Patterson Air Force Base, Dayton, Ohio, May 1970.

<sup>3</sup>H. R. Moy, "Advanced Stabilized Ejection Seat Development Program," SEG-TR-67-51, Aeronautical Systems Division, AFSC, Wright-Patterson Air Force Base, Dayton, Ohio, January 1968.

These components have been demonstrated in the field on helicopter stability augmentation systems.<sup>4</sup> The production fabrication technique is well established. The nozzle provides 20 deg of deflection of 3,500 lb thrust with less than 170 in-lb actuation torque. The two-axis TVC system performance is compared with STAPAC and a seat with no TVC. Many escape system trajectories are shown to analyze effects of controller attitude reference, rocket thrust level, and drogue attach point.

Fluidic component designs were verified by bench tests. The experimental dynamic response and integration accuracy closely matched the design goals. The nozzle friction and actuation torque were demonstrated to be 1/10th that of state-of-the-art nozzles.

#### BENEFITS OF TWO-AXIS TVC

The primary benefit of two-axis TVC is reduction of unsafe g loads due to yaw instability during high speed deceleration. Stabilizing seat attitude also reduces line entanglement and increases recovery altitude. Unsafe g loads are reduced by controlling yaw since a man can take 2.33 times more safe g load in the X direction than he can from the side.<sup>5</sup> The escape system is designed to slow the man down as fast as his body will allow. If the seat can be counted on not to yaw, neck injuries to pilots can be reduced.

---

<sup>4</sup>Darroll Bengston, Thomas Dickovich, and Robert Helfenstein, "Roll-Axis Hydrofluidic Stability Augmentation System Development," USAAMRDL-TR-75-43, Honeywell, Inc., Minneapolis, Minnesota, September 1975.

<sup>5</sup>Military Specification MIL-S-9479B (USAF), General Specification for Aircraft Upward Ejection Seat Systems, March 1971.

At low speed, main rocket TVC improves trajectory height. This is especially true if any cg misalignment occurs. However, TVC is detrimental to recovery during upside-down ejections since it stabilizes in an upside-down attitude. TVC also reduces line entanglement at low speed. The trajectory with no TVC shows the seat being pitched forward by the recovery chute. This is also accompanied by 360 deg of yaw.

The full benefits of TVC are not used, however, in these high deceleration systems. This TVC system can recover from high sink rates with much less altitude if a vertical seeking sensor and a longer burn time are used. The vertical sensor would simply interface with the pitch and yaw attitude references. The worst case condition, 450 knots with 30 deg dive angle, would require only 200 ft altitude, one second burn time, and 10 g deceleration. The 250 knot, 45 deg dive, 180 deg roll condition would require only 160 ft altitude. These benefits are worth looking into in the future.

#### ESCAPE SYSTEM PERFORMANCE RESULTS

A brief summary of TVC performance is listed in Table 1. TVC performance is compared with STAPAC and a seat with no TVC. It is clear from the table that yaw is controlled very well at all speeds. Pitch attitude is also controlled accurately until the recovery chute is deployed. The pitch rates are high at low speed because the seat is held steady in an upright position until the recovery chute jerks it around. The seat with no TVC pitches continuously during chute deployment causing considerable loss of altitude. As mentioned before, this behavior will cause line entanglement. The lack of attitude stability of the uncontrolled seat is very evident in Figure 1a. The attitude error causes system failure in that case. FTVC and STAPAC take full advantage of the rocket thrust before the recovery chute overpowers it.

The pitch and yaw rate histories are shown in Figures 1b and 1c. FTVC fully stabilizes the seat before line stretch occurs. That feature reduces unsafe g loads at high speed Mode I conditions, evident in Table 1. At these low speeds, the FTVC system keeps yaw angles within 2 deg. Figures 2a through 2c show high speed performance. The altitude trajectories in Figure 2a are all very similar. The drogue has primary influence over average seat attitude and, hence, altitude. Figure 2b shows that the seat oscillates in pitch because neither the drogue nor the seat is stable in this attitude. The TVC system does a good job of stabilizing the oscillations and hence reducing the spinal component of the g loads. However, the system would be much more effective if the seat

Table 1. Escape System Performance Summary

Velocity	Maximum Pitch Rate during Rocket Burn		Pitch Rate at Line Stretch		Maximum Yaw Rate during Rocket Burn		Yaw Rate at Line Stretch		Maximum Yaw Angle during Rocket Burn		Unsafe g Load				
	No TVC	STAPAC	No TVC	STAPAC	No TVC	STAPAC	No TVC	STAPAC	No TVC	TVC	No TVC	STAPAC			
0	537.	658.	837.	-358.	-2.	249.	22.	119.	115.	0.	113.	22.7	1.3	0	0
100	422.	684.	860.	-323.	-3.	168.	22.	105.	101.	0.	104.	20.3	1.3	0	0
240(I)	332.	1145.	1292.	-307.	17.	-32.	44.	92.	82.	-1.	87.	13.5	1.0	.353	.133
240(II)	261.	275.	120.	-238.	15.	107.	82.	697.	125.	-1.	69.	19.8	1.5	.003	0
400	638.	186.	265.	-356.	28.	-265.	159.	988.	20.	2.	39.	10.9	1.5	.008	.004
600	1012.	394.	606.	-735.	-141.	-337.	76.	1186.	-216.	6.	-34.	27.0	3.9	.117	.050

95th percentile pilot

3500 lb thrust

Drogue 6 in above cg

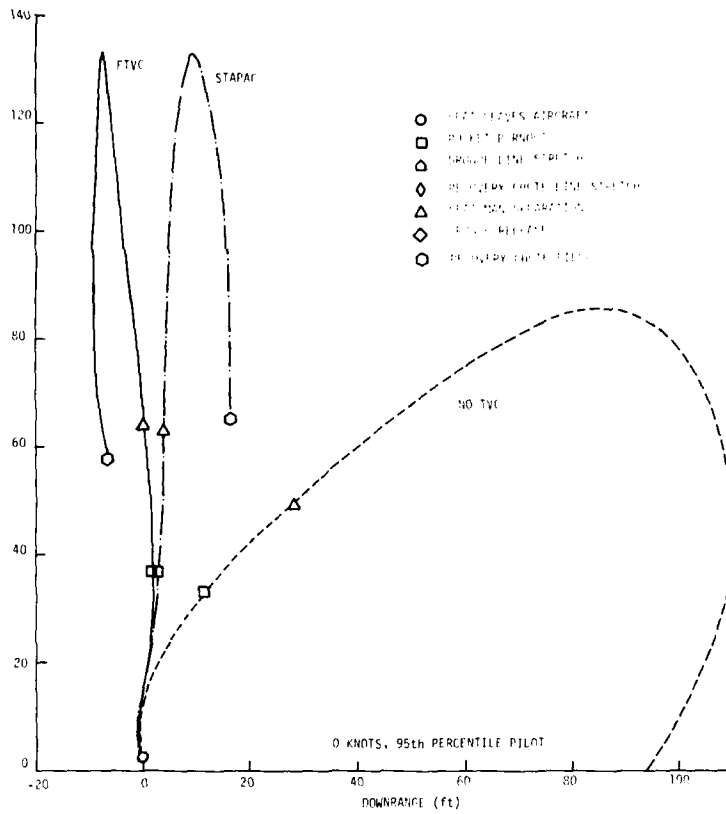


Figure 1a. Low Speed Altitude Trajectory

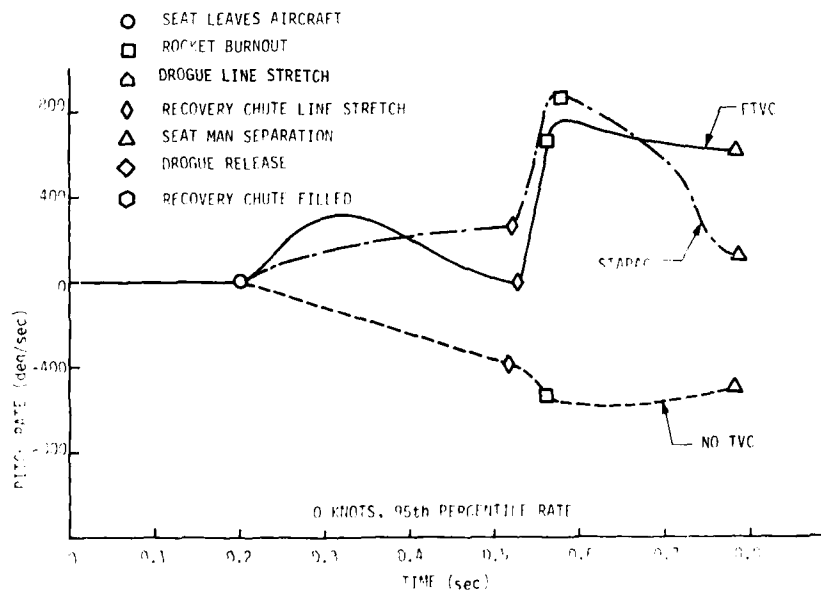


Figure 1b. Low Speed Pitch Rate History

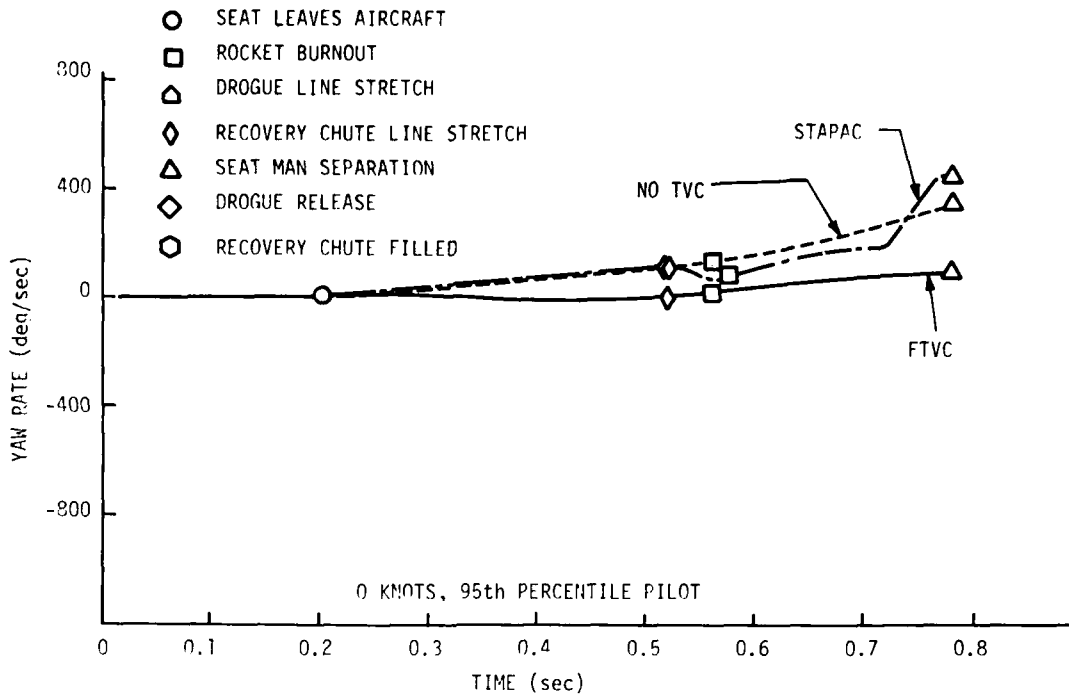


Figure 1c. Low Speed Yaw Rate History

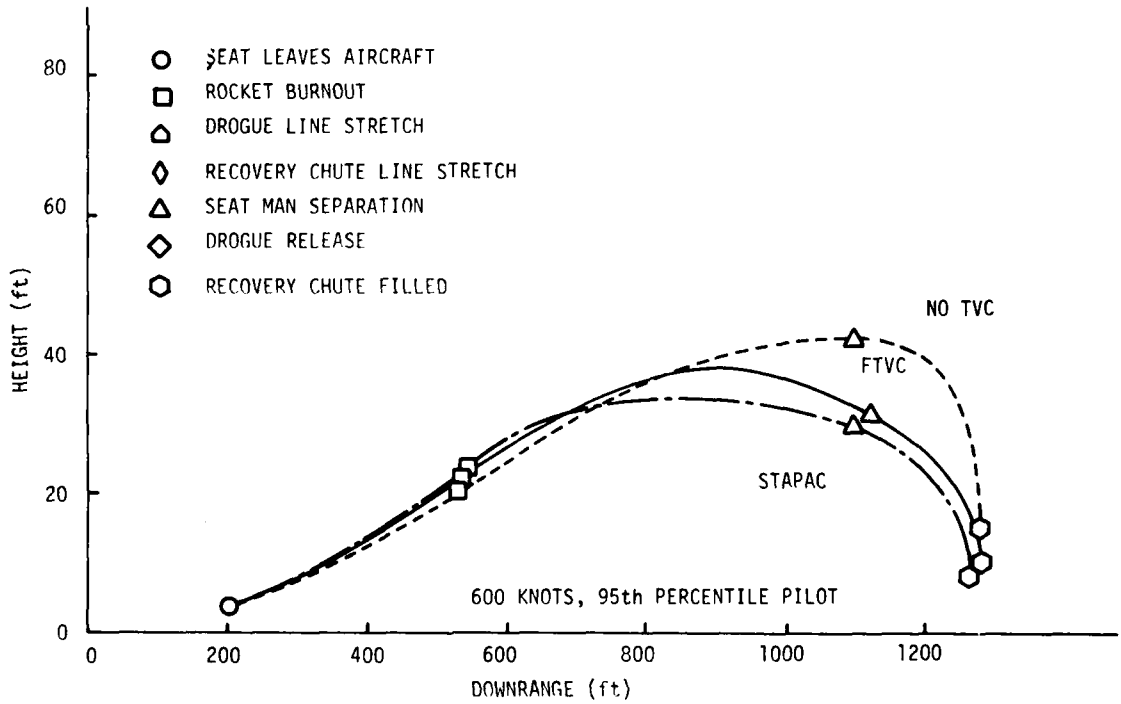


Figure 2a. High Speed Altitude Trajectory

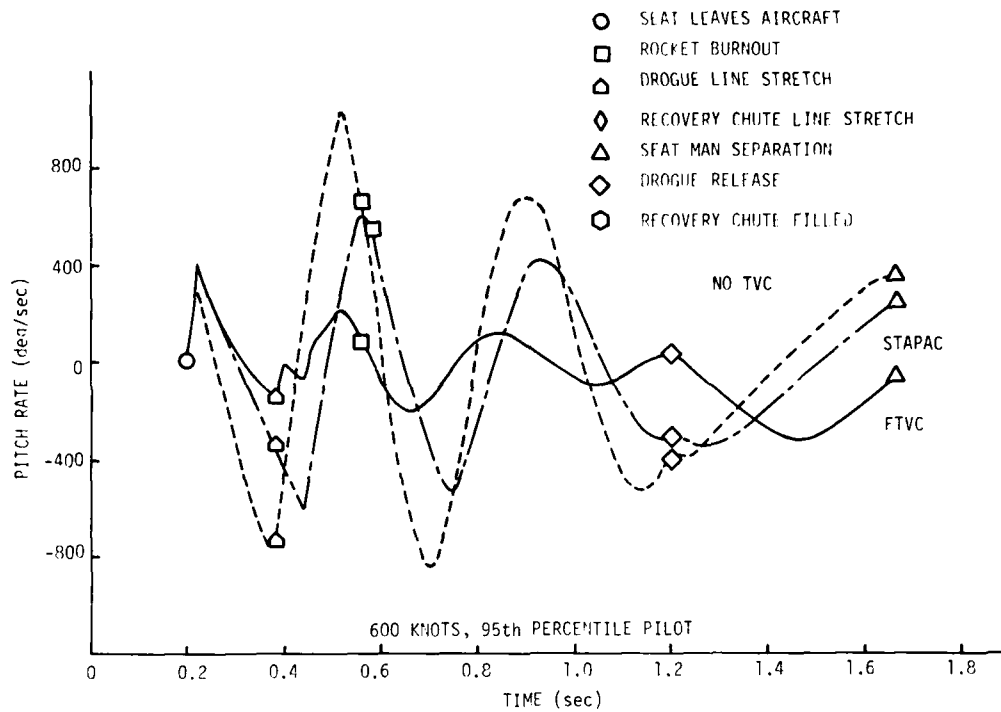


Figure 2b. High Speed Pitch Rate History

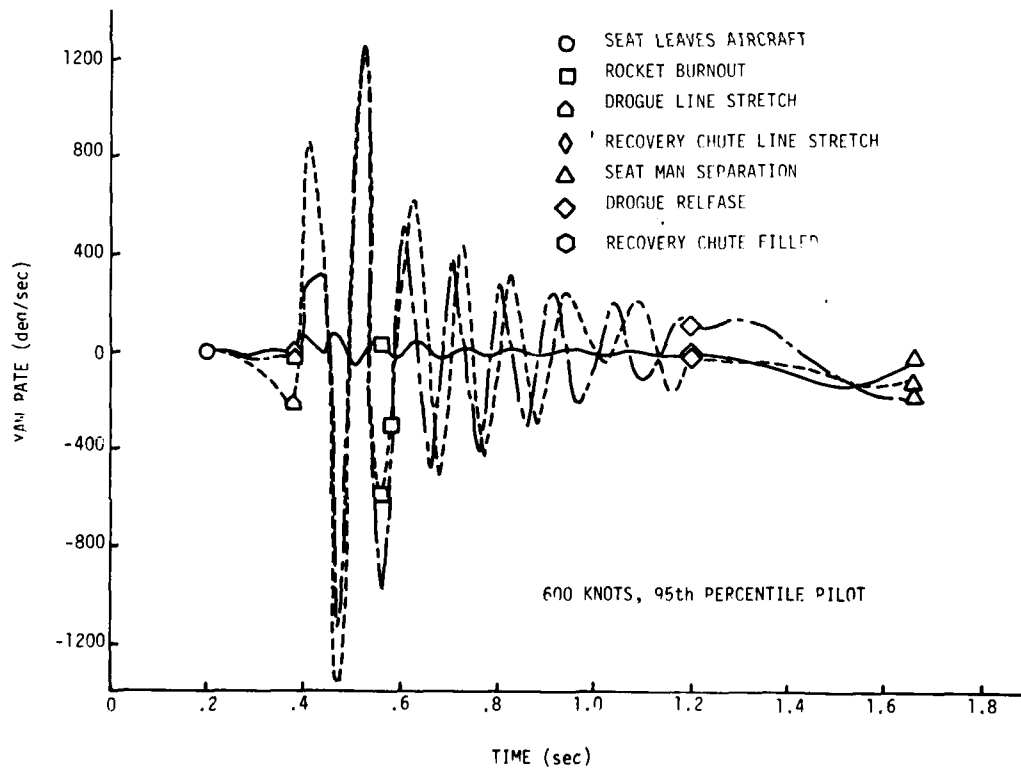


Figure 2c. High Speed Yaw Rate History

itself could be designed with a zero aero moment at zero angle of attack. This could be done with more surface area near the head rest. This is important because the pilot can take three times more g's in the x direction than he can in the spinal or z direction.

Figure 2c shows the most dramatic effect of the two-axis TVC system. The FTVC system reduces yaw rates and angles by a factor of 10. This reduction is even more important to g loads. The pilot can take five times more g's in the x direction than he can in the sideways or y direction.

The stability demonstrated in these figures will reduce line entanglement as well as bodily injury due to oscillating g loads. The high g load listed in Table 1 at 600 knots is caused by the higher drogue attach point chosen to obtain more altitude. This small increase in the angle of attack increases the g loads in the spinal direction.

#### COMPONENT DESCRIPTION

We chose components for the FTVC system that have been proven in the field in other applications. The integrated fluidic circuit board, described in Figure 3, was developed for helicopter flight controls. The manufacturing process, developed for helicopter flight controls, was tested on 40 U.S. Army helicopters. The Army experienced unusual reliability and near zero maintenance requirements.

The hydrostatically supported nozzle leads the state-of-the-art in actuator power required. It has been tested for a wide range of missile applications including ICBM's and ABM's. Combined with the fluidic controls, the system contains very few moving parts.

The integrated fluidic circuit is a complete attitude stabilization system. It contains a rate sensor, integrator, and a position control valve. The control valve drives the nozzle with hydraulic piston actuators. Position transducers on the actuator shaft feed back pressure signals proportional to nozzle angle. Three lines are required for this signal.

The control system gets its power from the hot gas main rocket. During years of shelf life, the system remains full of oil with no pressure. When the rocket is fired, the

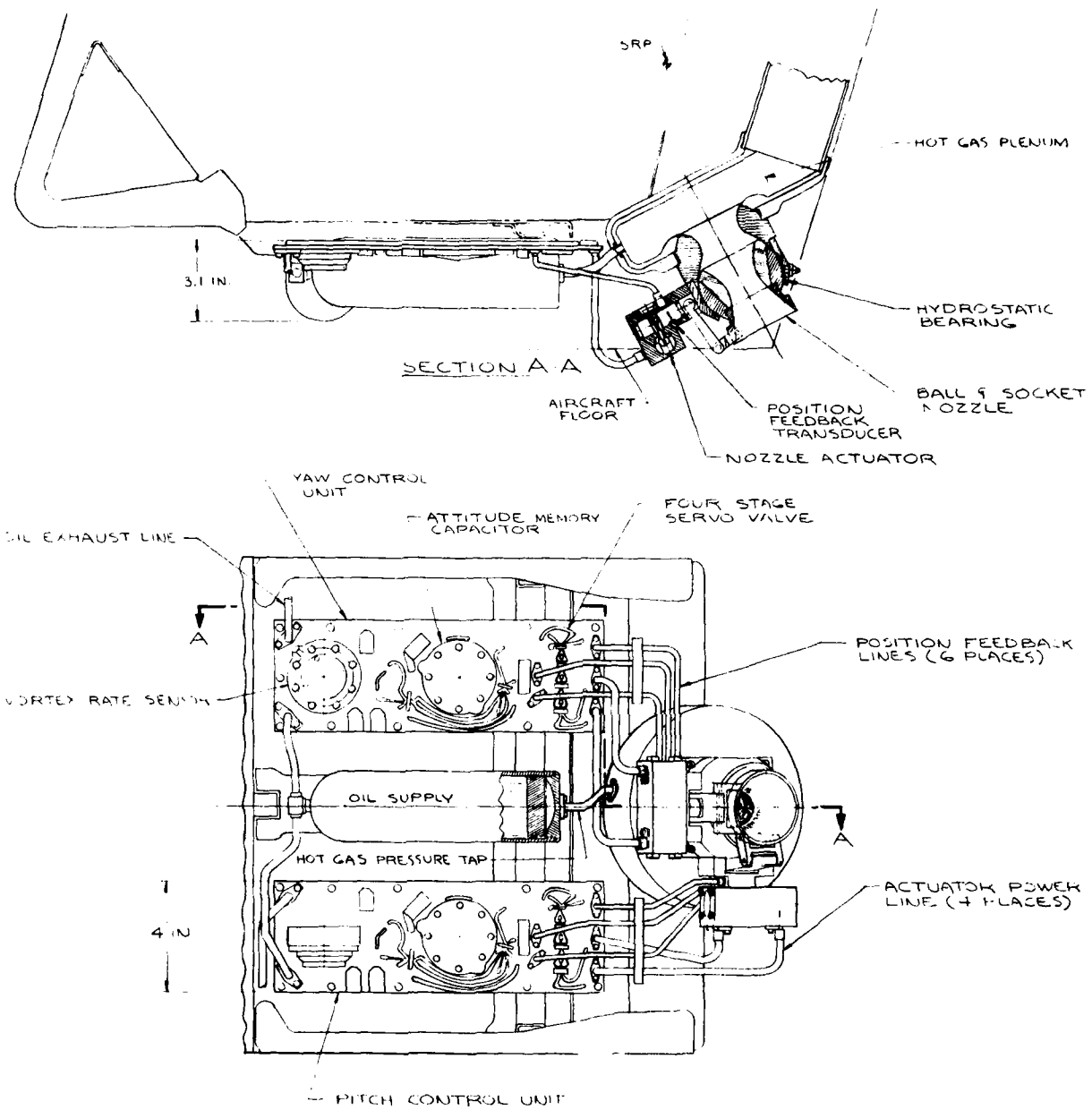


Figure 3. Escape System TVC Assembly

oil is pushed through the fluidic system. The main disadvantage of this system is that it takes a great deal of flow rate. However, the mission is so short that the amount of oil required is reasonable.

We built a prototype control system and tested the dynamic response of the components. They met all the specifications except null bias stability. The performance results are described in Section 3. Null bias correction requires tighter tolerances on amplifier mold machining.

The nozzle does not fit easily on the seat. There is interference of the nozzle with the existing seat structure. The large manifold behind the nozzle is needed to reduce gas velocities and erosion. The gas turns two corners. That unusual feature will require development in the future.

## SECTION 2

### ESCAPE SYSTEM REQUIREMENT ANALYSIS

Simulated seat trajectories were used to determine design and performance requirements for the thrust vector controlled escape system. Design parameters such as pitch attitude bias, thrust level, and drogue attach point were used to minimize pilot g loads and maximize recovery heights. A baseline design was chosen and compared with STAPAC and the uncontrolled seat. Detailed component performance requirements were obtained from the trajectory results and linear frequency response analysis. The design analysis section shows the effect of variations in the design parameters.

#### BASELINE DESIGN PERFORMANCE

A baseline design was chosen to meet both high and low speed requirements. This section compares the performance of that design with STAPAC and a seat with no TVC. The baseline design choice was a compromise between low and high speed requirements and a trade between g loads versus trajectory height. The choice was made for illustration purposes and was somewhat arbitrary. The design analysis, described later in this section, shows other viable alternatives.

#### Baseline Design Summary

For illustration purposes, we chose baseline escape system parameters of 60 deg pitch attitude bias, 3500 lb thrust, and drogue attach point 9 in above the cg. This system reduces unsafe g loads by improving yaw stability. The performance results are summarized in Table 2. Other design and performance parameters are summarized in Tables 3 through 5.

The benefits of TVC are most evident at higher air speeds. These results can be seen in Table 2. At low speed, the benefits of TVC are greater trajectory height and improved seat attitude stability. Seat stability will reduce line entanglement at all speeds. Above 100 knots in Mode I, the TVC attitude bias reduces the g loads due to recovery chute jerk. The control capability of TVC is not fully utilized in Mode I since the recovery chute force dominates and turns the seat 180 deg. This is necessary, though, to minimize chute deployment time.

Table 2. Simulation Results

Velocity	Initial Altitude	Dive Angle	Roll Angle	Sink Rate (ft/min)	Pilot Model	Recovery Height			Maximum Pitch Rate			Pitch Rate at Line Stretch		
						No TVC	TVC	STAPAC	No TVC	TVC	STAPAC	No TVC	TVC	STAPAC
0	0	0	0	0	5th	32.	75.	68.	339.	1049.	1100.	-339.	-8.	328.
100	0	0	0	0	5th	58.	64.	62.	317.	1102.	1179.	-317.	-8.	237.
240(I)	0	0	0	0	5th	53.	73.	68.	426.	1584.	1766.	-313.	1.	20.
240(II)	0	0	0	0	5th	47.	<141.	118.	256.	309.	325.	-237.	11.	322.
400	0	0	0	0	5th	39.	95.	16.	779.	206.	260.	-366.	33.	-260.
600	0	0	0	0	5th	-4.	17.	-3.	1093.	418.	662.	-708.	-137.	-407.
120	0	0	60	0	5th	-4.	0	-10.	326.	1139.	1167.	-326.	-10.	195.
150	200	0	180	0	5th	81.	51.	59.	307.	1237.	1334.	-307.	-14.	137.
150	300	0	0	10000	5th	207.	192.	196.	625.	908.	1031.	-433.	-8.	299.
200	500	60	0	0	5th	256.	278.	274.	321.	1407.	1549.	-298.	-1.	61.
450	500	30	0	0	5th	-33.	14.	-26.	837.	225.	400.	-337.	15.	-400.
200	550	60	60	0	5th	285.	304.	297.	322.	1415.	1531.	-303.	-3.	58.
250	600	45	180	0	5th	-127.	-151.	<-190.	258.	301.	187.	-193.	20.	164.
0	0	0	0	0	95th	-2.	57.	<66.	537.	658.	837.	-358.	-2.	249.
100	0	0	0	0	95th	43.	63.	63.	-422.	684.	860.	-323.	-3.	168.
240(I)	0	0	0	0	95th	49.	71.	66.	332.	1145.	1292.	-307.	17.	-32.
240(II)	0	0	0	0	95th	53.	124.	96.	261.	275.	120.	-238.	15.	107.
400	0	0	0	0	95th	41.	74.	20.	638.	186.	265.	-356.	28.	-265.
600	0	0	0	0	95th	15.	10.	9.	1012.	394.	606.	-735.	-141.	-337.
120	0	0	60	0	95th	-17.	-1.	-12.	485.	725.	786.	-328.	-5.	132.
150	200	0	180	0	95th	83.	49.	57.	424.	846.	959.	-313.	3.	80.
150	300	0	0	10000	95th	182.	172.	183.	576.	303.	630.	-432.	21.	188.
200	500	60	0	0	95th	231.	252.	249.	317.	933.	1094.	-302.	19.	4.
450	500	30	0	0	95th	-6.	-6.	-7.	823.	199.	359.	-411.	11.	-359.
200	550	60	60	0	95th	261.	278.	273.	401.	940.	1054.	-310.	17.	-3.
250	600	45	180	0	95th	-152.	-149.	-130.	264.	267.	79.	-206.	23.	21.

Table 2. Simulation Results (concluded)

Velocity	Initial Altitude	Maximum Yaw Rate			Yaw Rate at Line Stretch			Maximum Yaw Angle			Maximum Radical			Unsafe Radical		
		No TVC	TVC	STAPAC	No TVC	TVC	STAPAC	No TVC	TVC	STAPAC	No TVC	TVC	STAPAC	No TVC	TVC	STAPAC
0	0	102.	131.	189.	62.	4.	180.	11.8	6.2	.88	.84	.84	0	0	0	0
100	0	225.	138.	188.	59.	4.	188.	11.1	6.4	1.04	.84	.84	.027	.001	0	0
240(I)	0	1027.	170.	229.	38.	3.	219.	20.2	7.8	3.37	2.41	2.41	.448	.164	.246	.246
240(II)	0	336.	102.	737.	108.	4.	271.	16.0	2.5	1.63	1.47	1.47	.005	0	.003	.003
400	0	317.	183.	797.	-64.	3.	192.	12.8	6.2	2.03	2.19	2.19	.032	.013	.013	.013
600	0	1390.	582.	1233.	-301.	-4.	-226.	47.9	9.8	3.11	2.85	2.85	.186	.108	.086	.086
120	0	443.	147.	331.	71.	3.	235.	20.0	6.7	1.45	1.08	1.08	.053	.018	.003	.003
150	200	510.	166.	190.	46.	4.	201.	10.2	7.7	2.11	1.44	1.44	.136	.059	.080	.080
150	300	114.	124.	172.	69.	5.	172.	11.8	4.4	1.77	.85	.85	.065	0	0	0
200	500	798.	170.	203.	38.	3.	204.	13.4	7.2	2.86	1.62	1.87	.310	.112	.147	.147
450	500	905.	214.	98.	-69.	2.	-30.	37.3	4.3	2.28	1.63	1.52	.058	.029	.008	.008
200	550	983.	176.	298.	39.	3.	254.	12.5	7.5	2.75	1.63	1.93	.307	.117	.172	.172
250	600	330.	145.	769.	78.	4.	277.	11.2	2.4	1.62	1.02	1.53	.006	0	.005	.005
0	0	132.	22.	119.	115.	0.	113.	22.7	1.3	.82	.82	.80	0	0	0	0
100	0	103.	22.	105.	101.	0.	104.	20.3	1.3	.94	.88	.94	0	0	0	0
240(I)	0	96.	44.	92.	82.	-1.	87.	13.5	1.0	3.24	1.69	2.22	.353	.133	.239	.239
240(II)	0	457.	82.	697.	125.	-1.	69.	19.8	1.5	1.45	.80	1.06	.003	0	0	0
400	0	795.	159.	988.	20.	2.	39.	10.9	1.5	1.58	1.10	1.46	.008	.001	.004	.004
600	0	1309.	76.	1186.	-216.	6.	-34.	27.0	3.9	2.69	1.69	1.67	.117	.050	.032	.032
120	0	133.	27.	131.	131.	1.	132.	34.9	2.0	1.29	1.01	1.11	.010	0	.005	.005
150	200	91.	30.	103.	86.	0.	103.	18.7	1.2	1.97	1.16	1.32	.070	.015	.030	.030
150	300	143.	15.	99.	138.	0.	99.	23.8	1.3	1.34	.83	.80	.011	0	0	0
200	500	85.	31.	94.	80.	-1.	94.	15.3	1.1	2.52	1.47	1.90	.191	.079	.159	.159
450	500	443.	169.	63.	-51.	3.	-26.	14.7	5.8	1.80	1.21	1.30	.020	.003	.004	.004
200	550	104.	34.	109.	84.	0.	109.	22.7	1.3	2.41	1.47	1.91	.159	.082	.159	.159
250	600	458.	86.	717.	92.	-1.	98.	17.3	1.4	1.49	.79	1.24	.003	0	.001	.001

Table 3. Control System Performance Requirements

Parameter	Value	
	Pitch Axis	Yaw Axis
Maximum Nozzle Deflection	20 deg	10 deg
Maximum Slew Rate	700 deg/sec	700 deg/sec
Rate Sensor Time Delay	0.010 sec	0.010 sec
Lead Time Constant	0.10 sec	0.10 sec
Lag Time Constant	2.5 sec	2.5 sec
Actuator Time Constant	0.010 sec	0.010 sec
DC Gain	1.25	1.25
Control Attitude Bias	60 deg	-
TVC Initialization Time	0.18 sec	0.18 sec
Drogue Bridal Attach Point to SRP		
x		-.55 ft
y		±.51 ft
z		-1.54 ft

Table 4. Event Sequence

Event	Time (sec)	
	Mode I	Mode II
Catapult Ignition	0.0	0.0
Rocket Ignition	0.18	0.18
Drogue Deployment	-	0.19
Recovery Chute Deployment	0.20	1.04
Drogue Release	-	1.19
Seat/Man Separation	0.78	1.66

Table 5. Simulated Seat Characteristics

Parameter	Value	
	5th Percent Pilot	95th Percent Pilot
Weight (lb)	311.00	382.00
Reference Area (ft <sup>2</sup> )	6.38	6.94
Reference Length (ft)		
Longitudinal	2.85	2.97
Lateral	2.85	2.97
cg to SRP (ft)		
x	0.455	0.511
y	0.012	0.010
z	-0.775	-0.790
Inertia (slug-ft <sup>2</sup> )		
I <sub>xx</sub>	16.317	19.958
I <sub>yy</sub>	16.779	20.379
I <sub>zz</sub>	5.456	6.725
I <sub>xy</sub>	-0.338	-0.446
I <sub>xz</sub>	-0.882	4.061
I <sub>yz</sub>	0.595	0.295
Nominal Thrust Vector to		
Seat back (z axis)	47 deg	47 deg
Nozzle Position to SRP (ft)		
x	-0.369	-0.369
y	0	0
z	0.029	0.029

At higher speeds, there is a greater need for stability due to the aerodynamic oscillations and high g loads. The benefits of TVC are fully utilized in stabilizing the seat during the drogue phase. Maximum yaw angle is reduced by factors of 10 or more. This results in a significant reduction of unsafe g loads. The reduction at 600 knots is not apparent in Table 2. The higher g load is caused by the higher drogue attach point. The larger seat angle causes the g loads to increase in the spinal or z direction, offsetting the reduction in the side or y direction. The drogue was raised to obtain more trajectory height and more stability. This tradeoff is discussed further in the design analysis of a later subsection.

The two parameters in Table 2, maximum radical and unsafe radical, measure pilot g load. The first of these simply measures the maximum g force as a percentage of the maximum g force a human can endure without suffering injury. The second parameter, unsafe radical, measures the average amount, in percent, by which the g specification is exceeded. Reference 5 describes the method used to compute these parameters.

The control system performance requirements were determined from the trajectory analysis. They are listed in Table 3. The values are consistent with those obtained in a previous study.<sup>1</sup> The control system block diagram is shown in Figure 4.

The above results were obtained with the SAFEST ejection seat simulation.<sup>2</sup> The simulated seat characteristics and event time sequence are shown in Tables 4 and 5. The thrust time curve for the rocket is shown in Figure 5.

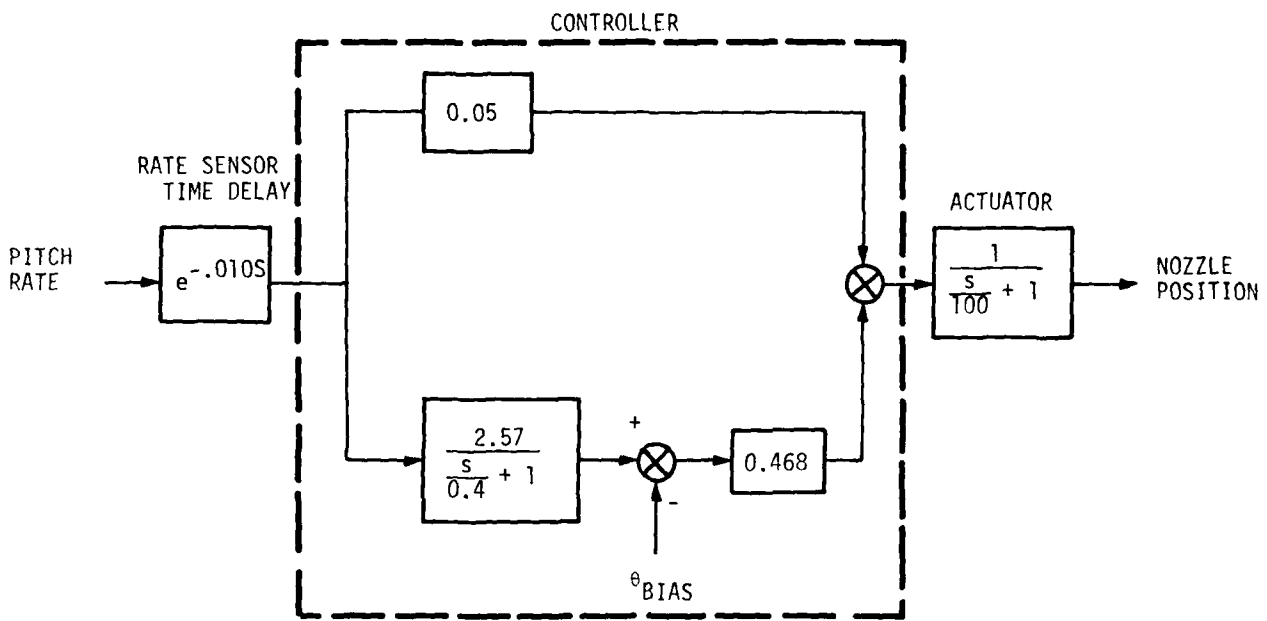


Figure 4. Pitch Axis TVC System

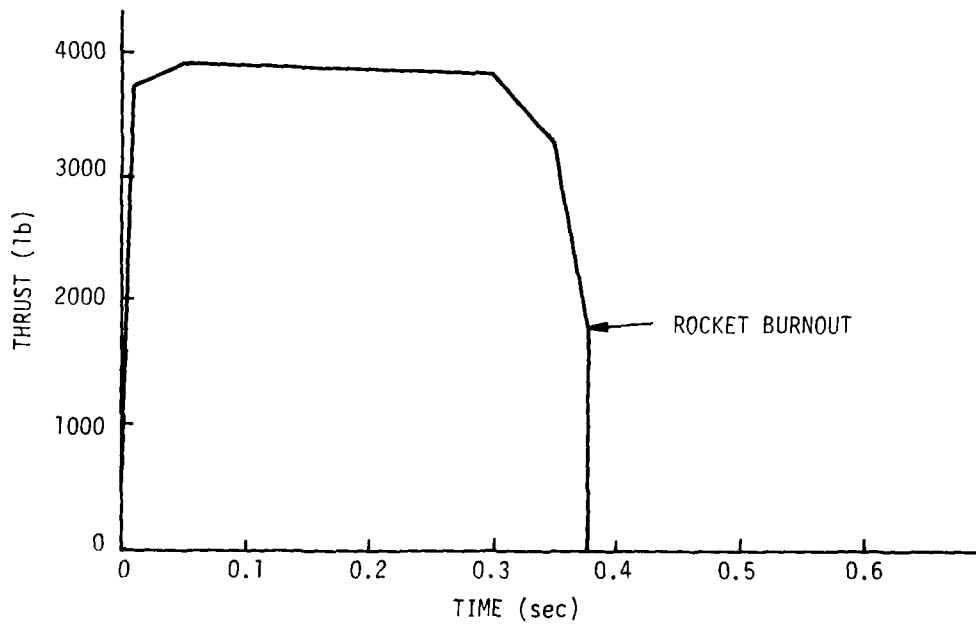


Figure 5. Rocket Thrust Response

### Comparison of TVC and the Uncontrolled Seat

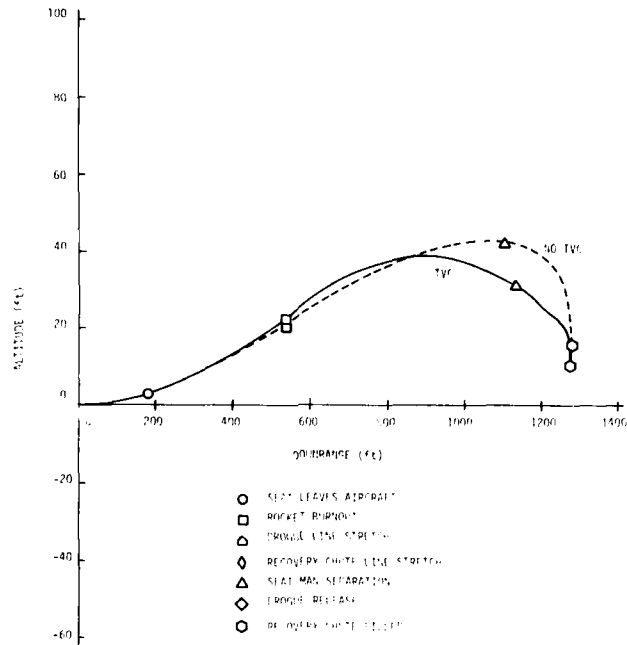
The improvement in stability is greatest in Mode II ejections, especially at high speed. The TVC system improves stability by working with the drogue to overcome the destabilizing effect of the aerodynamic forces. The aerodynamic forces pitch the seat forward and turn it around in opposition to the drogue which tries to stabilize the seat facing into the wind. The TVC system helps the drogue out by producing a control torque to counteract the aerodynamic forces.

The improvement in stability is most evident at 600 knots (Figure 6). The uncontrolled seat oscillates wildly in both pitch and yaw. With TVC the amplitude of the pitch oscillation is reduced by a factor of five and the yaw oscillation is virtually eliminated. The pitch oscillation is not completely damped out because the TVC system does not have enough control authority to totally overcome the aerodynamic forces at this speed.

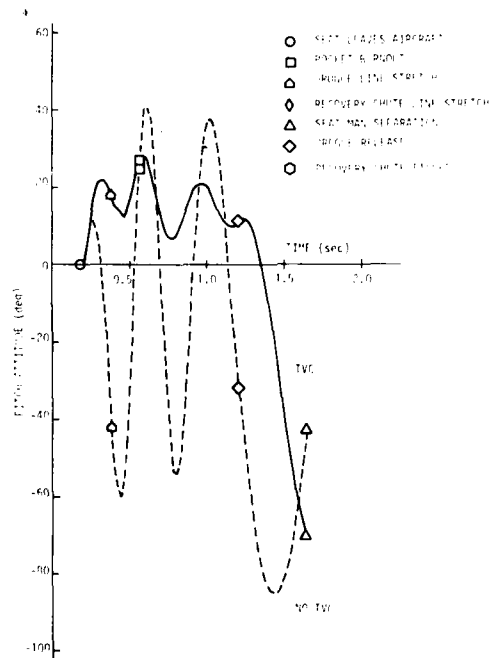
There is considerable improvement in yaw stability at 240 knots. The improvement in pitch stability is less dramatic (Figure 7). This is because drogue line stretch occurs later in the trajectory. The rocket burns out before the TVC system has a chance to stabilize the seat/drogue combination.

The TVC system easily stabilizes the seat in Mode I ejections (Figures 8 and 9). Pitch attitude is stabilized at the control bias angle (60 deg) and yaw offset is held to 1 deg throughout rocket burn. The seat then pitches up and yaws to the right in response to the forces generated by the recovery chute. Without TVC the seat is unstable throughout the trajectory and starts yawing to the right and pitching forward at launch. The lack of attitude control increases g loads and reduces trajectory height.

The TVC system reduces pilot g loads. Comparison of the data in the column titled "unsafe radical" in Table 2 shows that the uncontrolled seat exceeds the g specification by more than the TVC system in every case. The biggest difference occurs in a Mode I ejection at 240 knots. At this speed the TVC system only exceeds the g specification by 16 percent compared to 45 percent for the uncontrolled seat. The average difference in Mode I ejections is 9 percent; in Mode II ejections it is 3 percent.

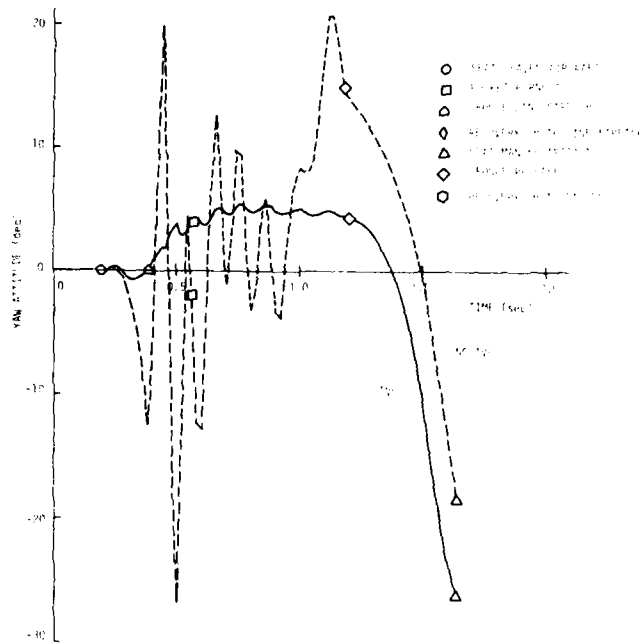


a) Altitude Trajectory



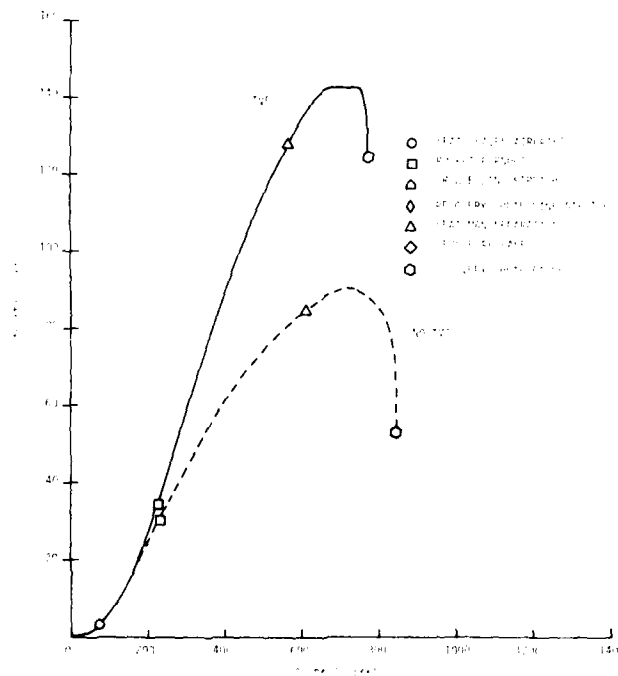
b) Pitch Attitude History

Figure 6. Comparison of TVC and the Uncontrolled Seat at 600 Knots



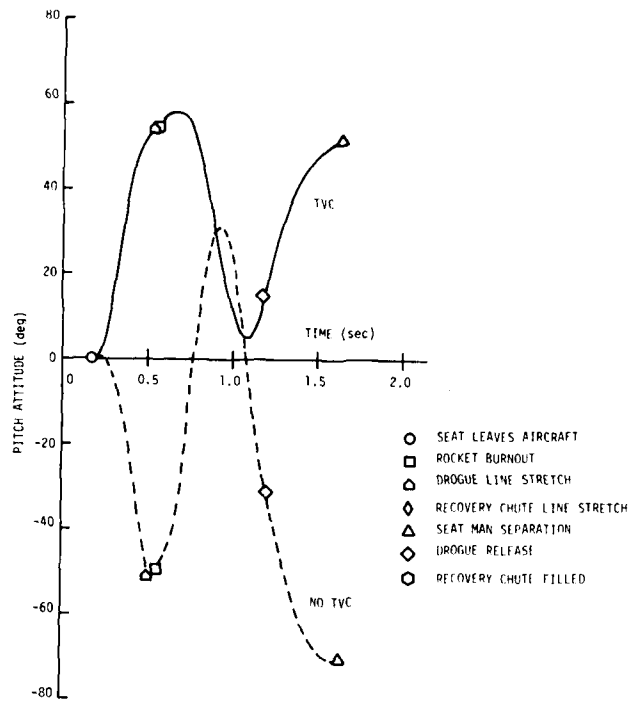
c) Yaw Attitude History

Figure 6. Comparison of TVC and the Uncontrolled Seat at 600 Knots (concluded)

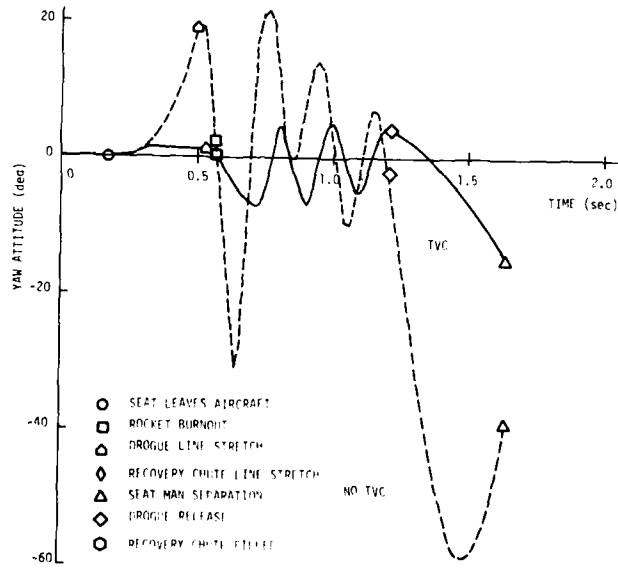


a) Altitude Trajectory

Figure 7. Comparison of TVC and the Uncontrolled Seat at 240 Knots

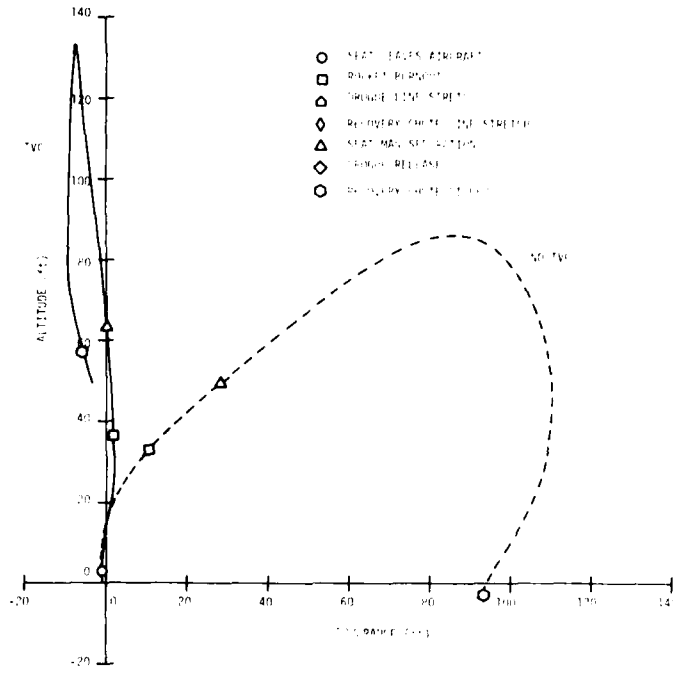


b) Pitch Attitude History

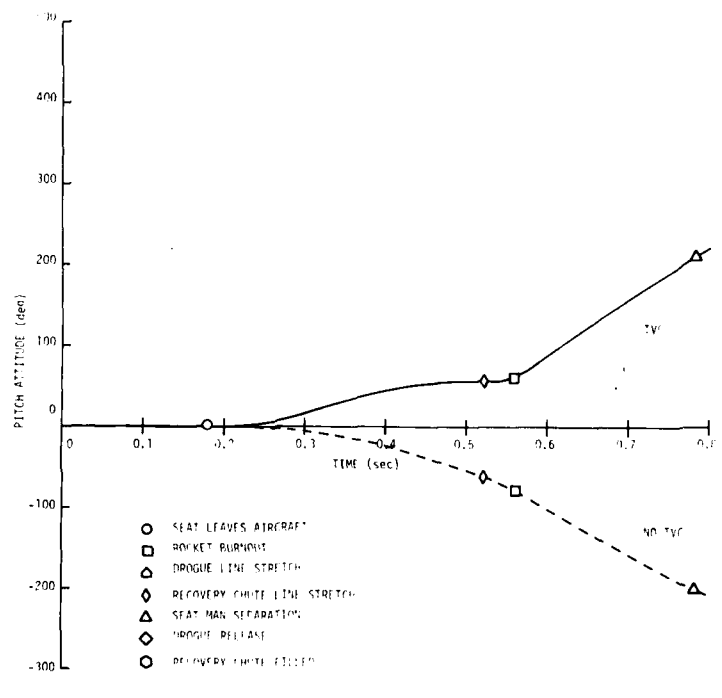


c) Yaw Attitude History

Figure 7. Comparison of TVC and the Uncontrolled Seat at 240 Knots (concluded)

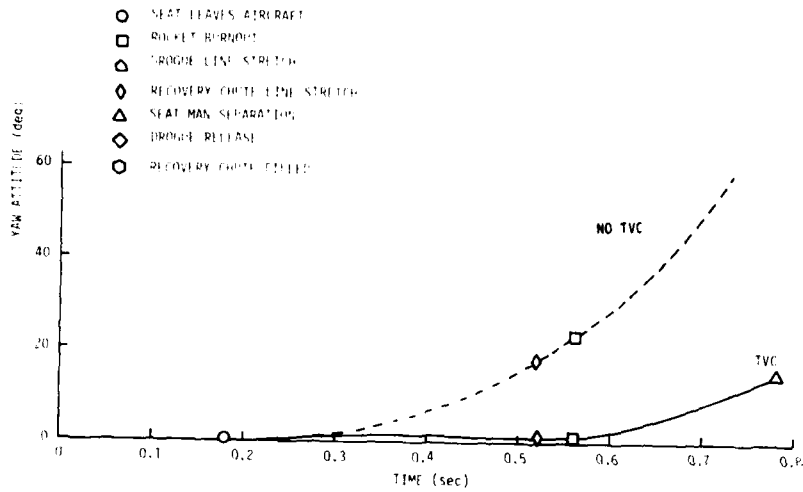


a) Altitude Trajectory



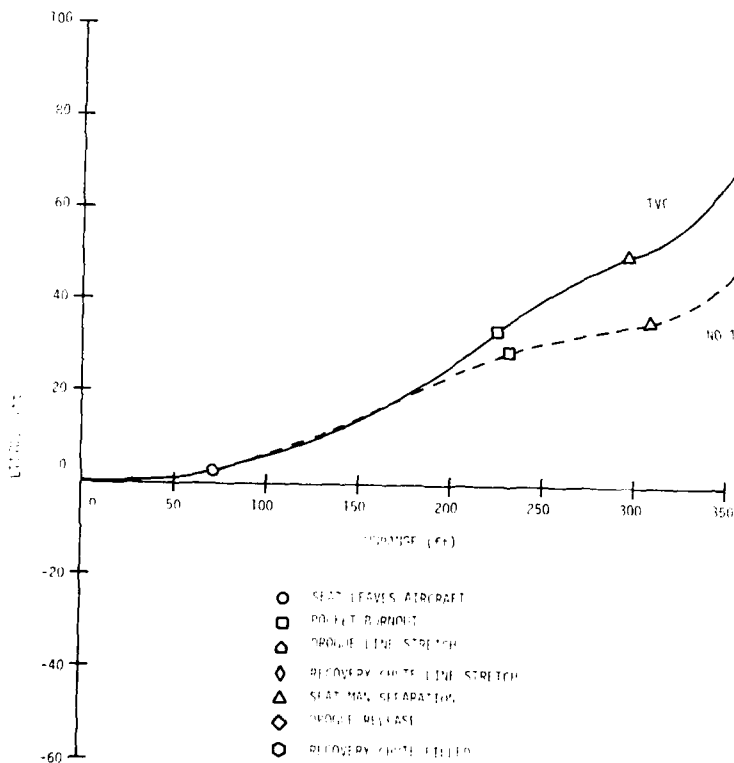
b) Pitch Attitude History

Figure 8. TVC and Open-Loop Performance at Zero Knots



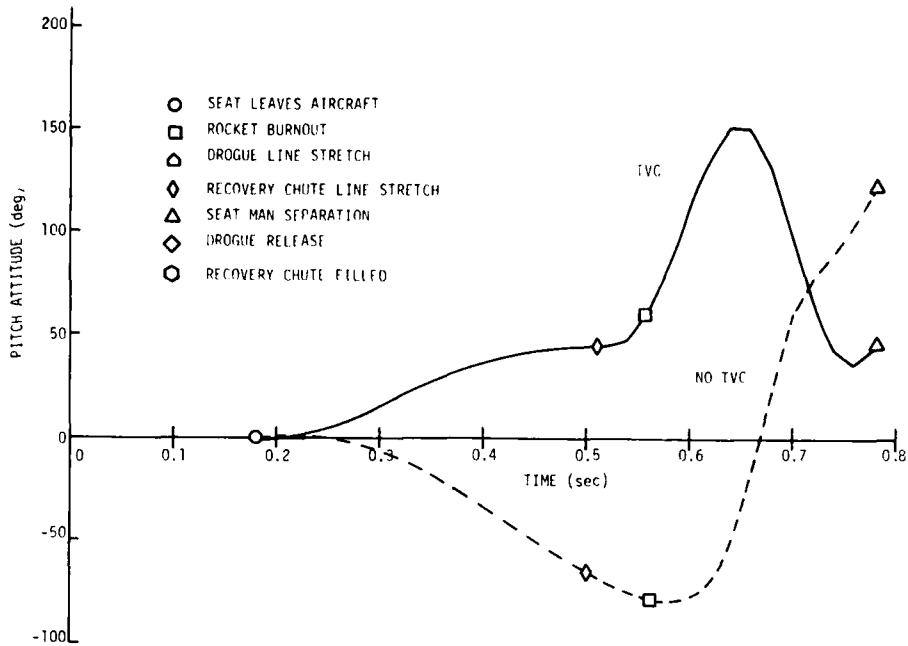
c) Yaw Attitude History

Figure 8. TVC and Open-Loop Performance at Zero Knots (concluded)

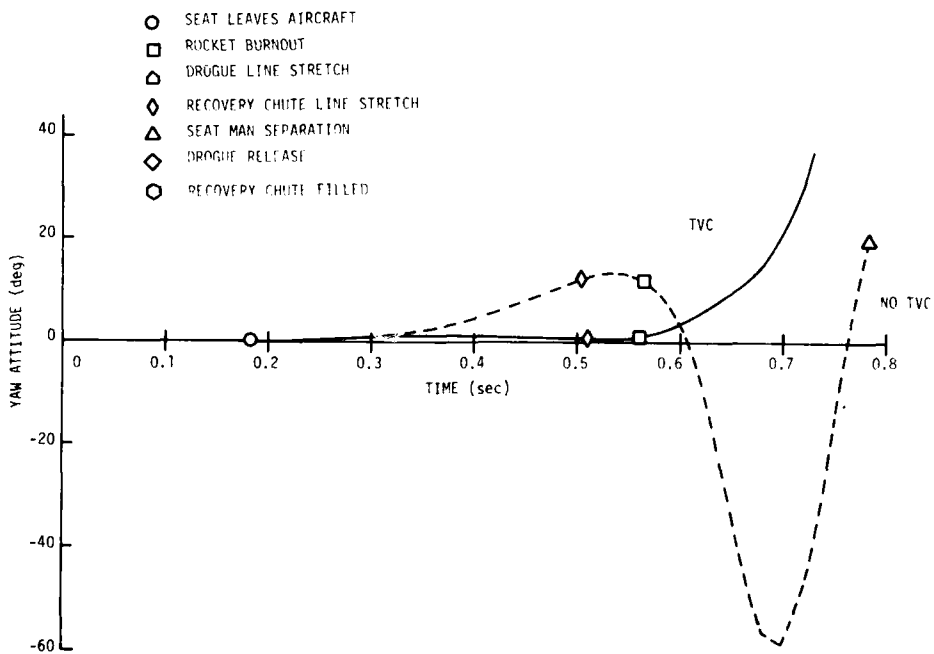


a) Altitude Trajectory

Figure 9. TVC and Open-Loop Performance at 240 Knots, Mode I



b) Pitch Attitude History



c) Yaw Attitude History

Figure 9. TVC and Open-Loop Performance at 240 Knots, Mode I (concluded)

The g loads are lower with TVC because TVC stabilizes the seat in an upright, forward facing position so that the aerodynamic and parachute deceleration forces are applied to the pilot in the eyeballs out direction. This reduces the size of the g radical since the pilot can withstand roughly twice as many g's in this direction as in the spinal and lateral directions. The data in Table 6 show how TVC affects the g load distribution in a typical ejection. Note how TVC reduces the g radical by shifting more of the total g load to the x axis.

The effect of TVC on recovery height is also shown in Table 2. In almost every case the TVC system gets more height than the uncontrolled seat, with the exception of the cases with an initial roll angle of 180 deg. The TVC system gains height over the uncontrolled seat by keeping the thrust vector in a vertical attitude. It does this by maintaining a positive pitch angle during rocket burn. The sample trajectories presented in Figures 6 through 9 demonstrate this behavior. Note that at 0 knots the uncontrolled seat pitches forward so far during rocket burn that it causes the seat to crash into the ground before the recovery chute opens.

#### Comparison of TVC and STAPAC

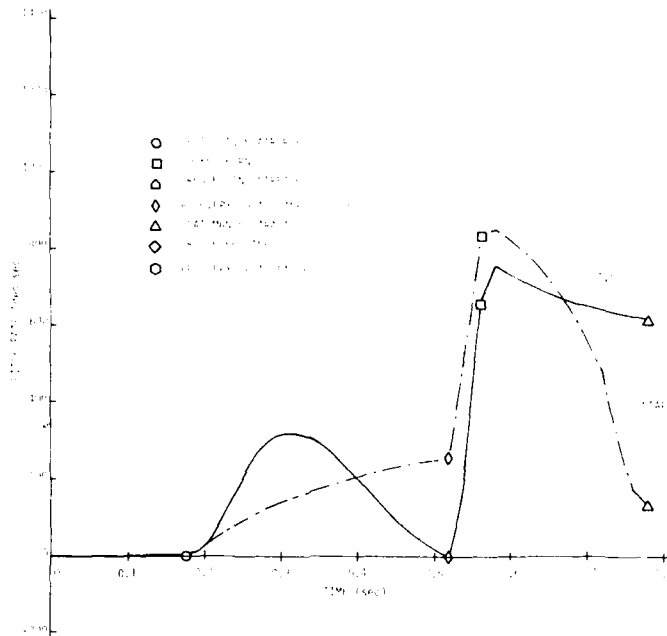
The TVC system demonstrates advantages over STAPAC. Evidence of improved stability is shown in Figures 10 and 11. These figures show that the TVC system is much more effective at damping out seat pitch and yaw rates than STAPAC, especially at high speed. The pitch rate and yaw rate data in Table 2 supply further proof of this ability. Note that the rates for the TVC system at line stretch are typically only a fraction of those of STAPAC. Also note that the maximum rates are smaller with TVC.

There are two reasons why the TVC system is more stable than STAPAC. First, STAPAC only controls seat pitching motion; it does not produce any control in the yaw axis. This explains why TVC is more stable in yaw. Second, TVC has more than twice the control authority of STAPAC because it uses the sustainer rocket to produce control moments instead of a vernier rocket.

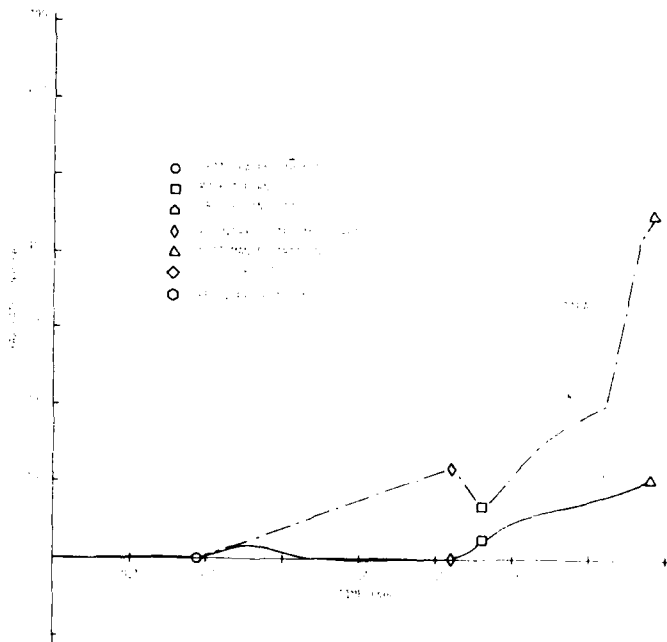
The g summaries in Table 2 demonstrate the lower g loads of TVC. In all but a few cases the TVC system has a smaller maximum radical and unsafe radical than STAPAC. The biggest difference between the two systems and also the highest g load occurs at 240 knots in Mode I. At this speed STAPAC exceeds the g specification by an average of about 24 percent while TVC only exceeds it by 13 percent.

Table 6. Aeromedical Summary--600 knots, 95th Percentile Pilot

Time (sec)	G <sub>x</sub>		G <sub>y</sub>		G <sub>z</sub>		DRI		Radical	
	No	TVC	No	TVC	No	TVC	No	TVC	No	TVC
	TVC		TVC		TVC		TVC		TVC	
0.0	0.00	0.00	0.00	0.00	0.00	0.00	0.00	0.00	0.00	0.00
0.1	-.55	-.55	-.00	-.00	10.24	10.24	8.79	8.79	.75	.75
0.2	-2.54	-1.31	-.02	-.02	3.84	2.12	7.80	7.60	.49	.48
0.3	-11.17	-5.15	-.60	-.51	4.32	9.89	8.59	14.63	.65	.93
0.4	-23.03	-27.07	-1.79	-.83	-17.16	13.30	-8.98	7.34	1.63	1.16
0.5	-27.90	-29.39	-14.93	.35	-6.93	19.86	-13.31	12.26	1.82	1.69
0.6	-12.46	-21.63	-6.13	-.73	20.08	15.79	28.09	14.98	1.85	1.18
0.7	-23.54	-21.62	-3.10	-.40	-.25	5.12	4.76	5.11	1.22	.79
0.8	-14.37	-17.70	-1.53	-.29	-11.06	3.35	-12.46	2.34	1.04	.65
0.9	-15.18	-12.76	-1.09	-.19	-1.02	6.35	-3.39	5.61	.68	.57
1.0	-6.58	-10.89	.27	.06	5.67	5.65	9.47	5.09	.63	.48
1.1	-9.65	-11.14	.26	-.04	4.53	3.24	5.53	2.32	.47	.40
1.2	-4.22	-3.18	-.03	-.04	-1.80	.34	-4.52	1.93	.31	.16
1.3	-3.08	-3.36	.02	-.13	-2.12	-.00	-2.59	-.36	.20	.16
1.4	-2.07	-4.45	.03	-.42	-2.05	-1.55	-1.88	-2.43	.18	.22
1.5	-2.25	-4.03	.07	-.73	-2.05	-1.90	-1.87	-2.75	.19	.23
1.6	-3.03	-2.84	.01	-1.06	-1.85	-2.11	-1.56	-2.76	.18	.21

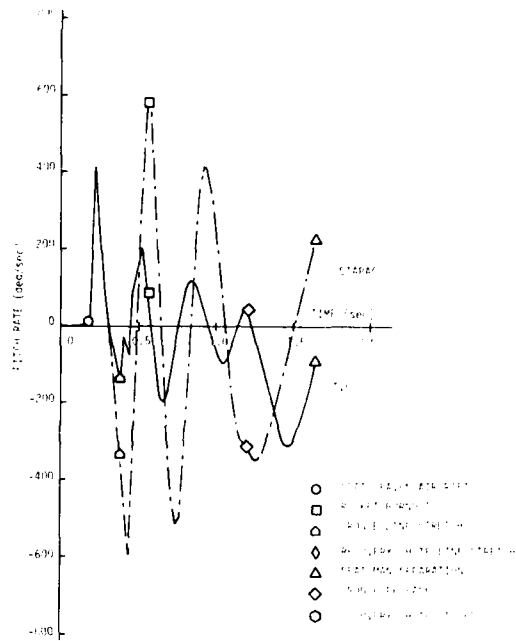


a) Pitch Rate History

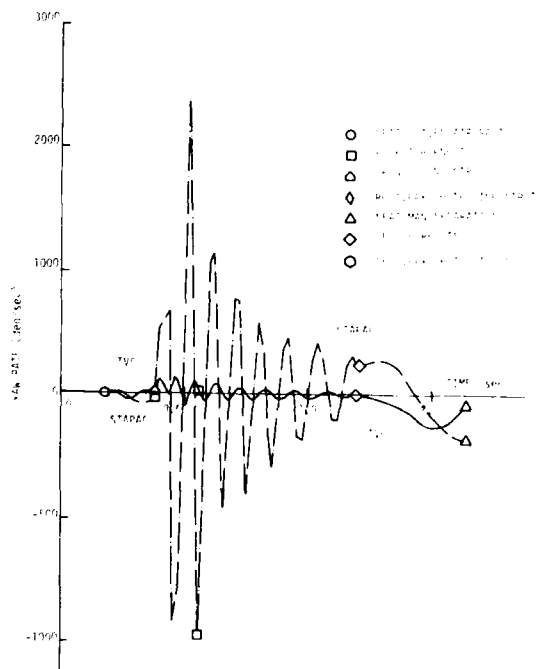


b) Yaw Rate History

Figure 10. TVC and STAPAC Performance at Zero Knots



a) Pitch Rate History



b) Yaw Rate History

Figure 11. TVC and STAPAC Comparison at High Speed

The TVC system has lower g radicals than STAPAC because it is more stable. The data in Table 7 show how this works. This table lists the maximum and minimum g loads experienced in a Mode I ejection at 240 knots. Note the differences between the two control systems, especially the differences in the  $g_y$  components. STAPAC's  $g_y$  components are much bigger than those of TVC because STAPAC is less stable in yaw. These differences in  $g_y$  are the primary reason why STAPAC has a larger unsafe radical than TVC at this speed. STAPAC allows the seat to yaw more than TVC, thereby shifting more of the total g load from the x axis to the y axis. This produces a larger radical because the  $g_y$  components are weighted more heavily than the  $g_x$  components in the calculation of the radical.

The third advantage of the TVC system over STAPAC is that it has more recovery height. The results presented in Table 2 show that the TVC system gets more height than STAPAC in all cases except for the ones in which the initial roll angle is 180 deg and the two cases which have an initial sink rate. The biggest difference occurs in Mode II ejections where the TVC system gets as much as 80 ft more height than STAPAC.

The TVC system typically gets more height than STAPAC because it tips the seat back more during rocket burn. This places the rocket nozzle in a position which directs more thrust toward the ground producing more height, unless of course the seat happens to be upside down initially. The pitch responses shown in Figure 12 demonstrate this behavior in a level attitude ejection at 240 knots. With these initial conditions, the rocket nozzle is pointed directly at the earth when the pitch angle is 47 deg.

#### COMPONENT DESIGN REQUIREMENTS

The static and dynamic performance requirements for the TVC system were derived from the trajectory analysis. Requirements for the TVC system hardware are shown in Table 8 and Figure 13. These requirements are based on 6 DOF simulation results and a stability analysis of the pitch axis control system.

Table 8 lists the limiting values for most of the control system design parameters. The nozzle deflection limits should be as large as possible. We need at least  $\pm 20$  deg pitch deflection and  $\pm 10$  deg yaw deflection. The deflection rates should also be as large as possible, at least 700 deg/sec are needed.

Table 7. Maximum g Loads--240 knots, Mode I, 5th Percentile Pilot

	TVC	STAPAC
$g_{x \max}$	24.91	28.53
$g_{x \min}$	-30.24	-21.88
$g_{y \max}$	9.85	13.09
$g_{y \min}$	-2.98	-29.85
$g_{z \max}$	24.79	24.86
$g_{z \min}$	0	-0.15
$\text{DRI}_{\max}$	25.03	30.49
$\text{RAD}_{\max}$	1.80	2.41

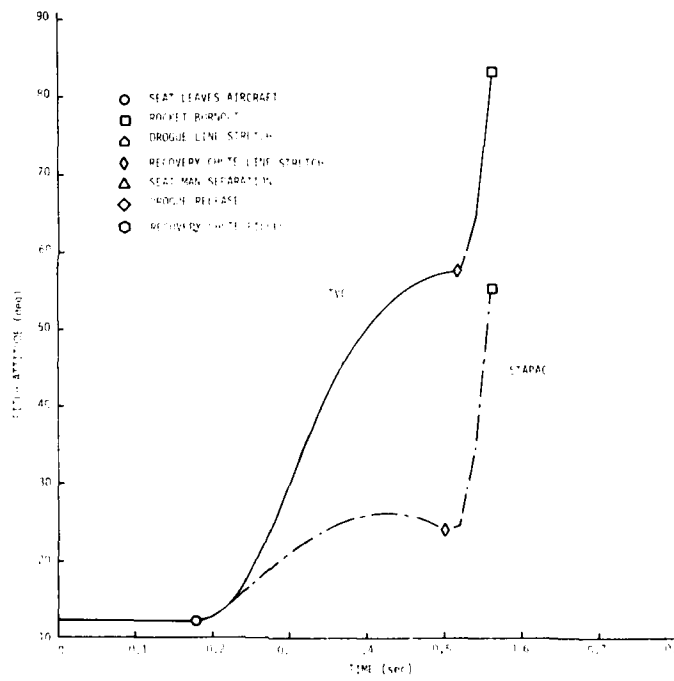


Figure 12. TVC and STAPAC Pitch Attitude History at 240 Knots, Mode I

Table 8. Control System Requirements

	Preferred	Minimum	Maximum
Pitch Deflection	± 20 deg	± 20 deg	_____
Yaw Deflection	± 10 deg	± 10 deg	_____
Deflection Rate	700 deg/sec	700 deg/sec	_____
Nozzle Jitter	_____	_____	± 2 deg RMS
Pitch Attitude Bias	60 deg	50 deg	70 deg
Controller Threshold	_____	_____	10 deg/sec
Frequency Range	_____	0.1 Hz	10 Hz
DC Gain	1.25 deg/deg/sec	1.0 deg/deg/sec	1.25 deg/deg/sec
Integrator Time Constant	2.5 sec	2.5 sec	3.13 sec
Lead Time Constant	0.1 sec	0.1 sec	0.2 sec
Actuator Time Constant	0.0135 sec	_____	0.0135 sec
Rate Sensor Time Delay	0.010 sec	_____	0.010 sec

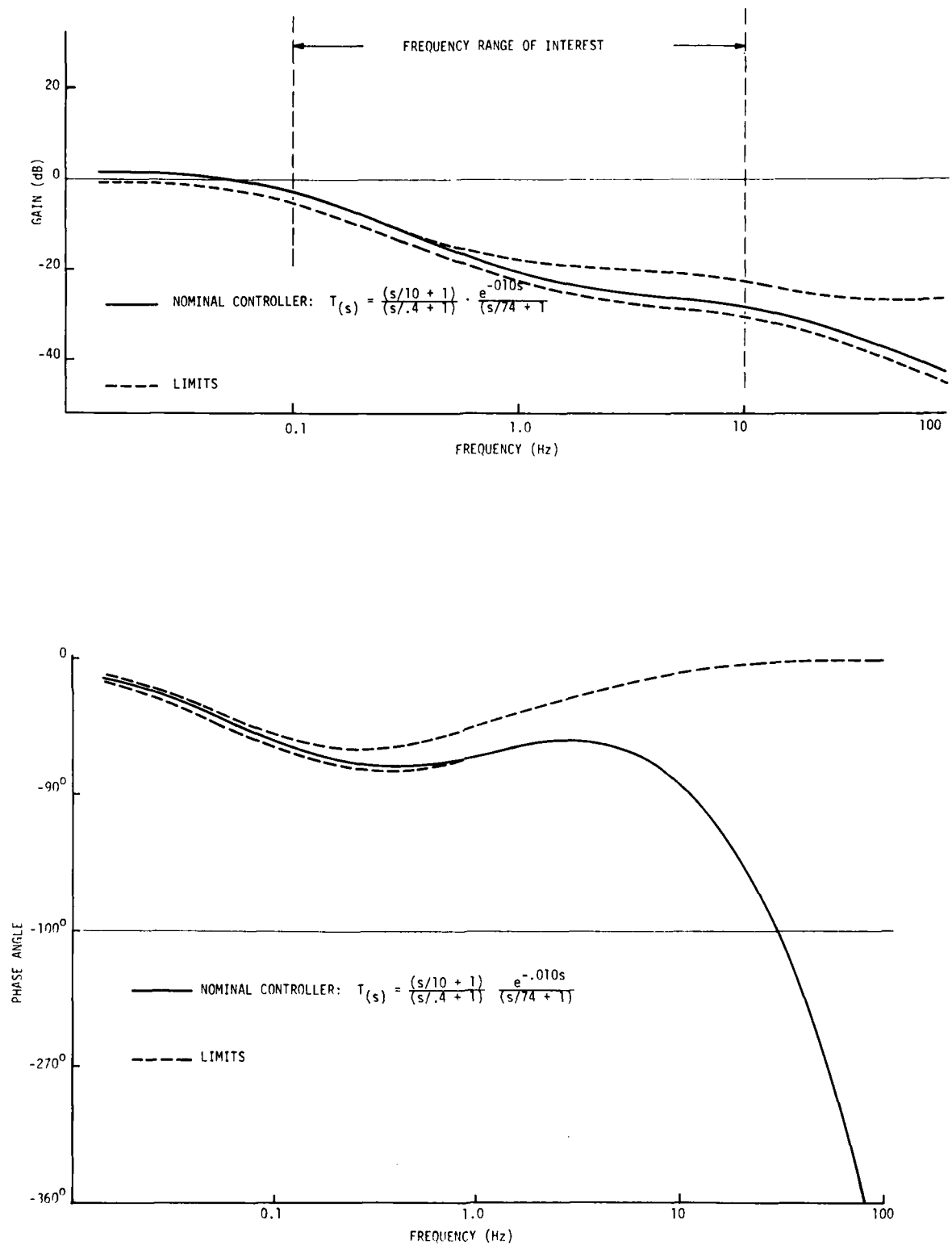


Figure 13. Control System Frequency Response Requirement

Nozzle jitter should be less than  $\pm 2$  deg RMS to maintain sufficient control authority. Two degrees of jitter reduces the effective control moment by about 10 percent.

The pitch attitude bias should be set as close to 60 deg as possible since this angle gave the best performance in the 6 DOF simulation. Variations of up to  $\pm 10$  deg are acceptable.

The controller threshold should be held to a minimum with a maximum value of 10 deg/sec. Controller threshold is defined as the smallest rate input which can be detected by the control system and results in a measurable nozzle response. This parameter should be small to limit attitude drift in the control system.

The controller DC gain should be in the 1.00 to 1.25 deg range of nozzle deflection per deg/sec of rate input. A value close to 1.25 deg/deg/sec is preferred since this will give the most control authority. The DC gain should not be larger than 1.25 deg/deg/sec because it might cause the TVC system to become unstable in ejections at high speed. This can be seen in the seat open-loop frequency response shown in Figure 14. Note that with a DC gain of 1.25 deg/deg/sec the phase margin is only about 30 deg at this speed. Increasing the DC gain further would reduce the phase margin even more.

The integrator time constant should be between 2.5 and 3.13 sec to preserve the accuracy of the seat attitude reference. The preferred value is 2.5 sec. This parameter should not be smaller than 2.5 sec because it can also cause the seat to become unstable in ejection at high speed. Figure 14 shows that lowering the time constant has the same effect as increasing the DC gain on pitch stability at 600 knots. It raises the gain response so that the gain crossover frequency is lowered and the phase margin is reduced.

The lead time constant should be about 0.1 sec. It can be somewhat larger but should not be decreased because reducing it introduces a stability problem in low speed ejections. This parameter determines the ratio between the control system attitude gain and the rate gain. Increasing the time constant increases the rate gain and improves system stability. Decreasing it has the opposite effect as the frequency response in Figure 15 shows.

The actuator time constant should not be larger than 0.0135 sec to maintain sufficient phase margin in low speed ejections (Figure 15). The rate sensor time delay should not be longer than 0.010 sec for the same reason.

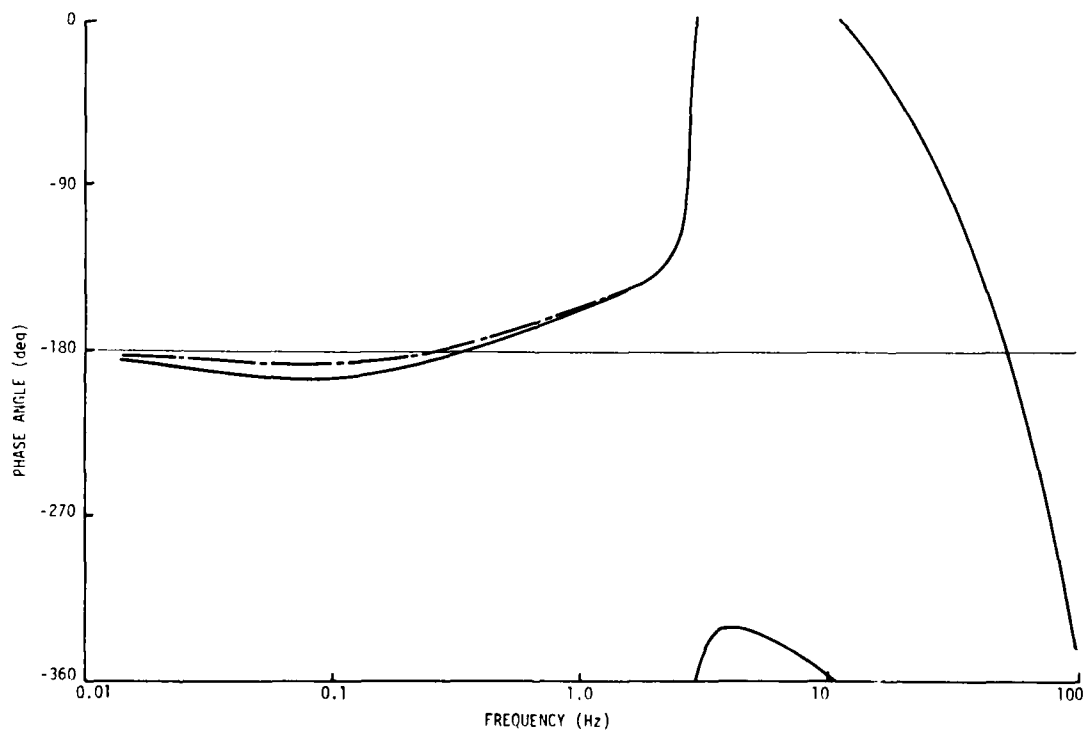
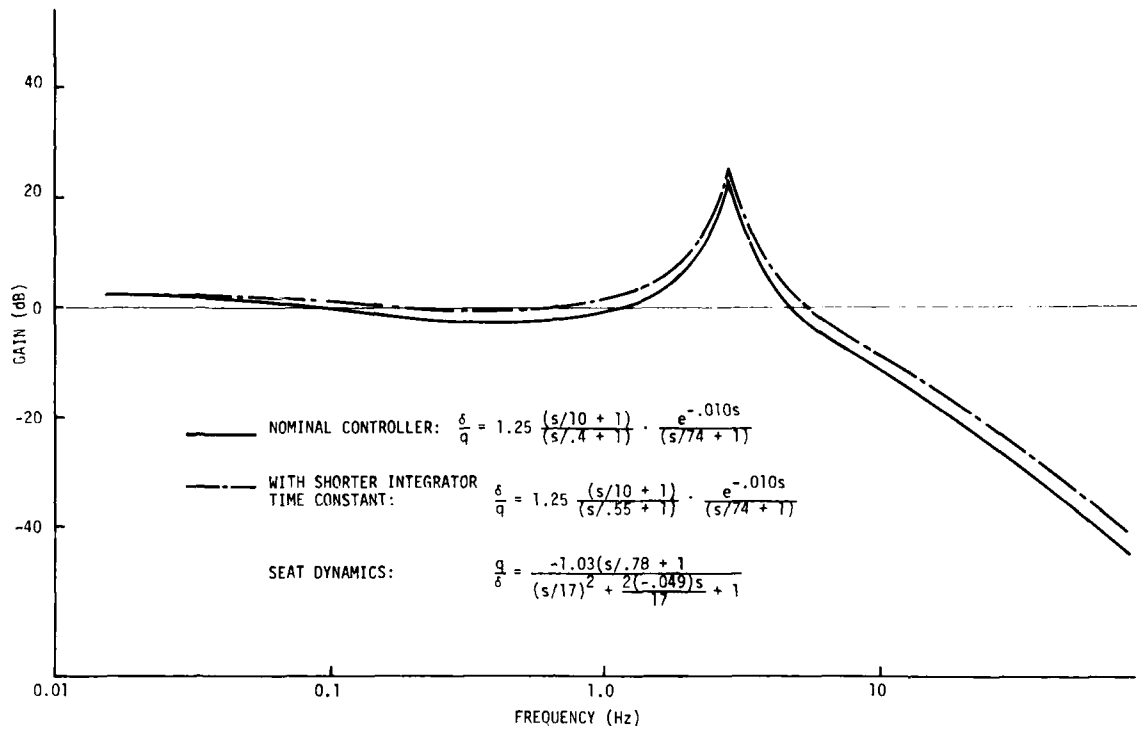


Figure 14. Ejection Seat Linearized Pitch Axis Frequency Response at 600 Knots

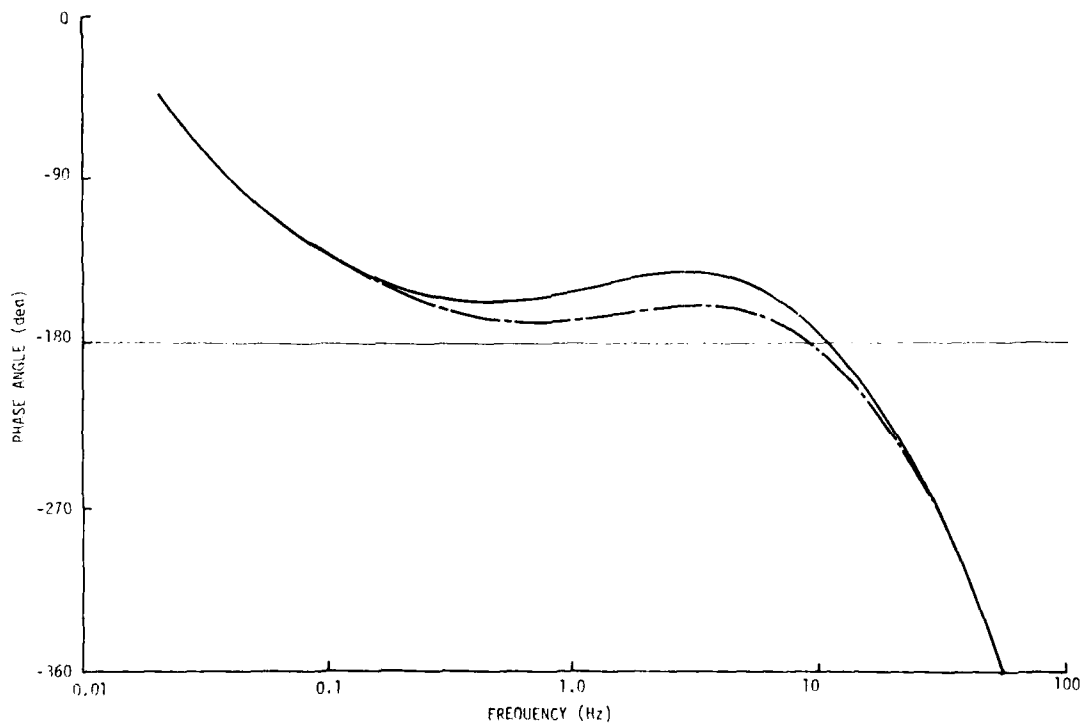
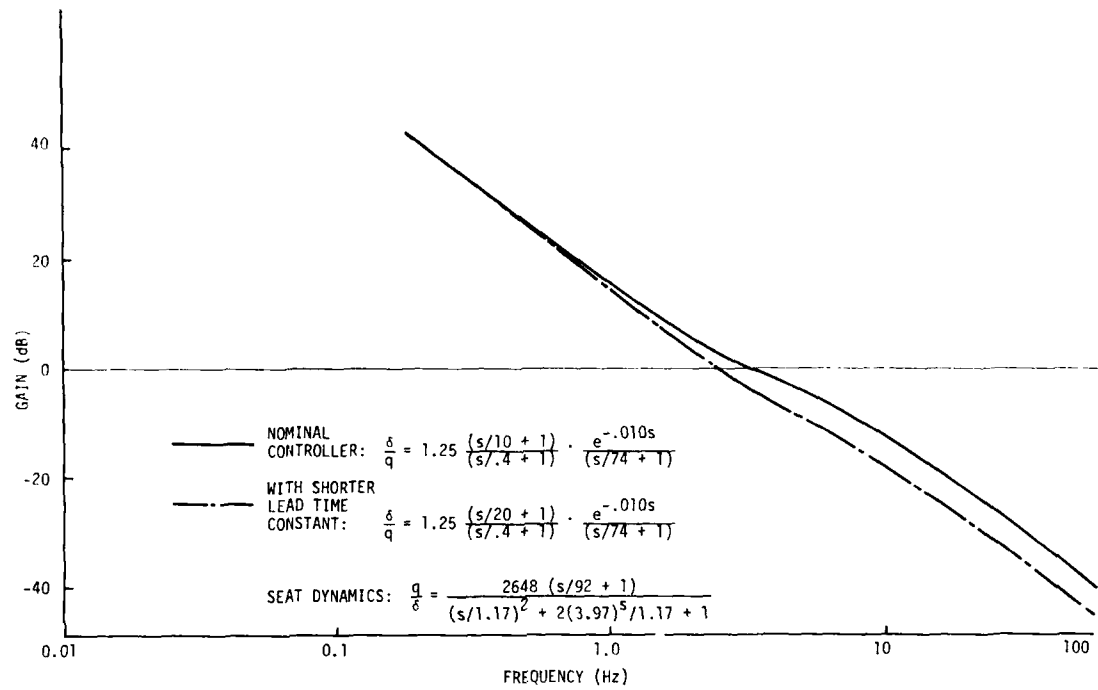


Figure 15. Linearized Pitch Axis Frequency Response at Zero Knots

Frequency response requirements for the controller are shown in Figure 13. The solid curves in this figure show the frequency response of the nominal controller. The dashed lines define the envelope of acceptable variations. These limits were chosen to maintain adequate control authority and gain and phase margins under all flight conditions.

The lower limit on the gain response is 2 dB below the gain response of the nominal controller throughout the entire frequency range. The upper limit coincides with the gain of the nominal controller below about 4 Hz and varies from 0 to 6 dB higher than the gain of the nominal controller in the frequency range 4 to 20 Hz. Above 20 Hz, the upper limit is constant at -26 dB.

The lower limit on the phase response is about 5 deg below the response of the nominal controller below 4 Hz and coincides with the response of the nominal controller above 4 Hz. The difference between the upper limit and the phase response of the nominal controller increases with frequency from about 3 deg at 0.02 Hz to over 360 deg at 100 Hz.

#### DESIGN ANALYSIS

This section discusses the effects of pitch control attitude bias, rocket thrust, and drogue attach point on system performance. Trajectory results are presented comparing bias angles ranging from 0 to 150 deg, rocket thrusts of 3500 and 5000 lb, and two different drogue options. Time/thrust curves for the two rockets are shown in Figure 16. The two drogue options consist of a "nominal" version and a "high drogue" version. In the nominal version the drogue is fastened to the seat almost directly behind the seat's/man's cg. The attach point is six inches higher in the high drogue version. These two options are illustrated in Figure 17.

#### Summary of Design Analysis

The results presented in this section show that the escape system performs best overall with a bias angle of 60 deg, 3500 lb rocket, and high drogue option. This configuration is a compromise between the configuration which works best in Mode I ejections and the one which works best in Mode II ejections.

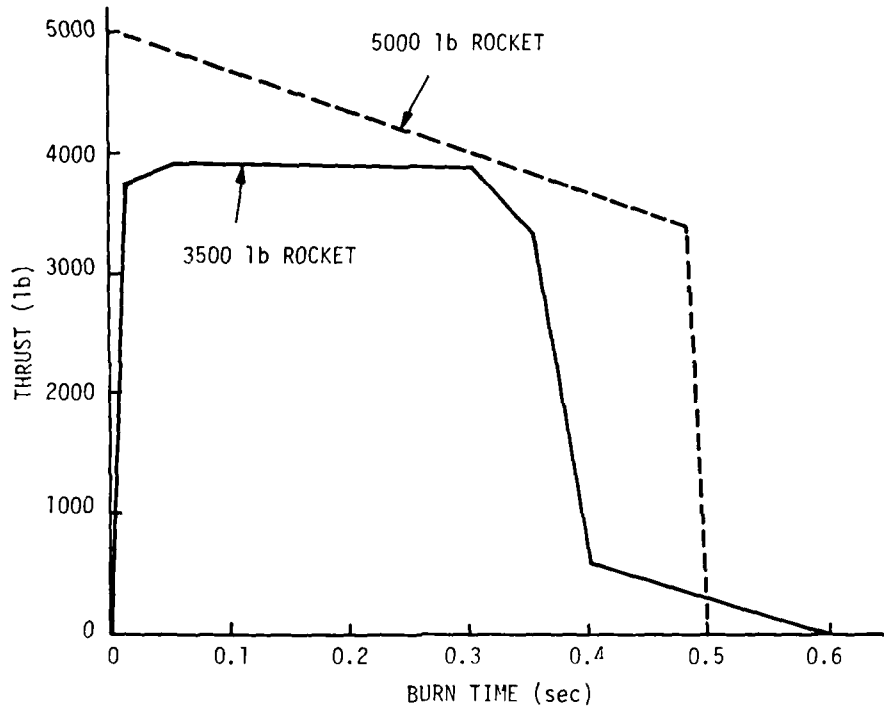


Figure 16. Rocket Thrust Time Responses

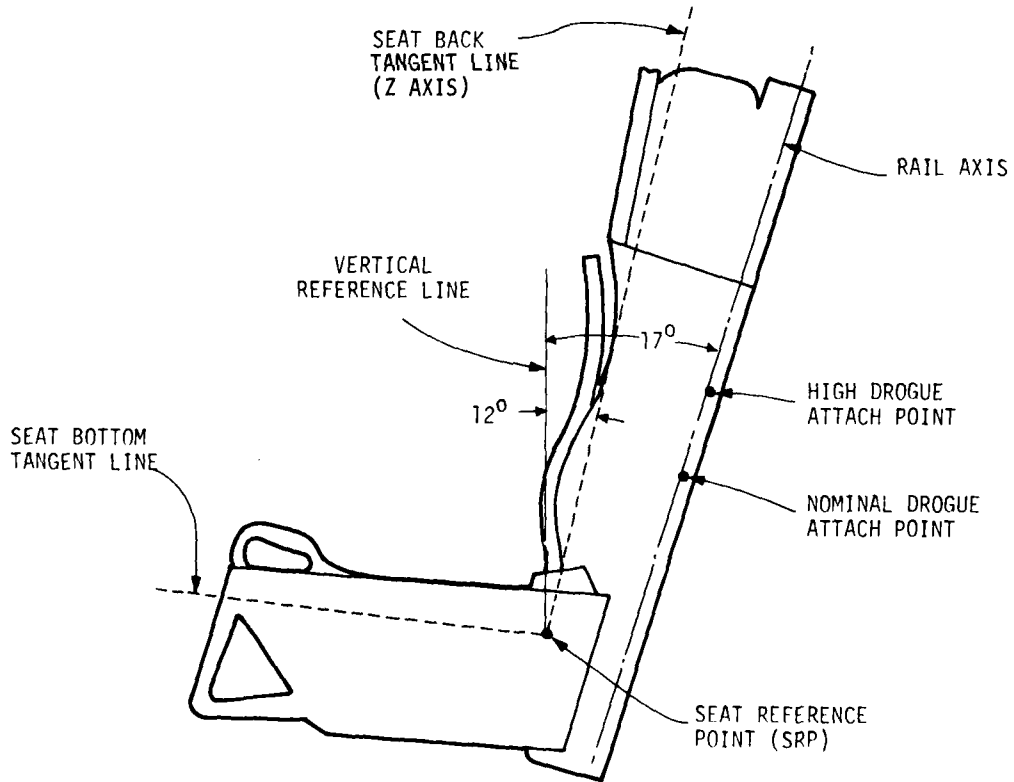


Figure 17. Seat Geometry

In Mode I the best results are obtained with a large bias angle (90 to 120 deg) and the 3500 lb rocket. This combination gives better pitch damping and lower g's than any other configuration tested. A smaller bias angle in combination with the 3500 lb rocket also works well in Mode I; however, the pitch damping and g loads are not as good as with a larger bias angle. The 5000 lb rocket is not a good choice in Mode I. It produces too many g's.

The combination of 60 deg bias, 5000 lb rocket, and nominal drogue performs best in Mode II ejection. The same bias angle together with the 3500 lb rocket and the high drogue is a close second. The only significant difference between the two is that the latter produces higher g forces. Both configurations give plenty of recovery height and do a good job of stabilizing the seat.

It should also be noted that combinations using the 3500 lb rocket and the nominal drogue do not work very well in Mode II regardless of the choice of bias angle. These combinations cannot produce enough recovery height at 600 knots for a safe ejection.

Selected results showing how the system works in level attitude ejections are presented in Table 9 and are discussed in the following paragraphs. These results are for a 5th percentile pilot. They were all obtained using the Air Force's 6 DOF simulation and the simplified representation of the TVC control law given below.

The data presented in Table 10 show that the simplified model is a very good approximation of the complete model.

COMPLETE

$$T(s) = 1.25 \frac{(s/10. + 1)}{(s/0.4 + 1)} \cdot \frac{e^{-0.01 s}}{(s/100 + 1)}$$

SIMPLIFIED

$$T(s) = 0.5 \frac{(s/10. + 1)}{s(s/100. + 1)}$$

Table 9. Mode I Simulation Results, 5<sup>th</sup> Percentile Pilot

Speed (knots)	$\theta$ Bias	Thrust	Pitch Rate			Yaw Rate			RBO Roll Attitude	Full Chute Position			g Radical		
			Max	Ln. Str.	RBO	Max	Ln. Str.	RBO		x	y	z	Max	Ave	Unsafe
0	60	3500	988.	-4.	913.	98.	0.	74.	8.	-11.	5.	74.	.88	.567	0
	90	3500	873.	6.	873.	127.	-3.	127.	2.	-42.	1.	153.	.88	.558	0
	150	3500	740.	46.	46.	32.	-8.	-8.	5.	-53.	-2.	-2.	.88	.622	0
	60	3500	988.	-4.	913.	98.	0.	74.	8.	-11.	5.	74.	.88	.567	0
	60	5000	1018.	5.	16.	98.	0.	-38.	0.	-46.	1.	77.	1.01	.749	0
	240 (I)	60	3500	1527.	1.	1527.	131.	0.	109.	2.	332.	0.	73.	1.72	.959
	90	3500	875.	104.	875.	123.	-18.	123.	3.	338.	0.	65.	1.42	.898	.086
	120	3500	545.	118.	133.	51.	-9.	51.	11.	350.	1.	51.	1.38	.892	.056
	60	3500	1527.	1.	1527.	131.	0.	109.	2.	332.	0.	73.	1.72	.959	.159
	60	5000	1692.	2.	-1332.	366.	0.	366.	60.	321.	-2.	72.	2.45	1.180	.327

Note: Ln. Str.--Line Stretch  
RBO--Rocket burnout

Table 9. Mode I Simulation Results, 5<sup>th</sup> Percentile Pilot (concluded)

Speed (knots)	θ Bias	Drogue Attach Point	Thrust	Pitch Rate			Yaw Rate			REO Roll Attitude	Full Chute Position			g Radical		
				Max	Ln. Str.	RBO	Max	Ln. Str.	RBO		x	y	z	Max	Ave	Unsafe
240 (II)	0	Nom	3500	267.	-2.	142.	99.	3.	-63.	0.	851.	-3.	33.	1.04	.346	0
	30	Nom	3500	128.	-26.	60.	46.	3.	-30.	-4.	768.	8.	97.	.97	.323	0
	60	Nom	3500	299.	1.	-30.	81.	2.	-64.	-14.	698.	4.	138.	.91	.390	0
	60	Nom	3500	299.	1.	-30.	81.	2.	-64.	-14.	698.	4.	138.	.91	.390	0
	60	Up 6"	3500	300.	2.	110.	66.	2.	-56.	-15.	782.	29.	131.	1.00	.407	0
	60	Nom	3500	299.	1.	-30.	81.	2.	-64.	-14.	698.	4.	138.	.91	.390	0
	60	Nom	5000	333.	13.	-49.	40.	2.	7.	-9.	681.	5.	207.	.97	.438	0
	600	0	Nom	3500	543.	-222.	-97.	235.	41.	149.	59.	1208.	-12.	25.	2.76	.614
30		Nom	3500	536.	-449.	16.	1325.	-62.	-808.	50.	1252.	-53.	-16.	2.31	.635	.061
60		Nom	3500	401.	-95.	60.	269.	-2.	86.	10.	1236.	-4.	-44.	1.64	.617	.024
60		Nom	3500	401.	-95.	60.	269.	-2.	86.	10.	1236.	-4.	-44.	1.64	.617	.024
60		Up 6"	3500	401.	-93.	-35.	288.	-2.	19.	12.	1237.	1.	23.	2.23	.777	.107
60		Nom	3500	401.	-95.	60.	269.	-2.	86.	10.	1236.	-4.	-44.	1.64	.617	.024
60		Nom	5000	401.	-20.	233.	139.	3.	-18.	9.	1247.	3.	20.	1.74	.655	.030

Note: Ln.Str.-- Line Stretch  
RBO--Rocket burnout

Table 10. Comparison of Simplified and Complete Control Law Models

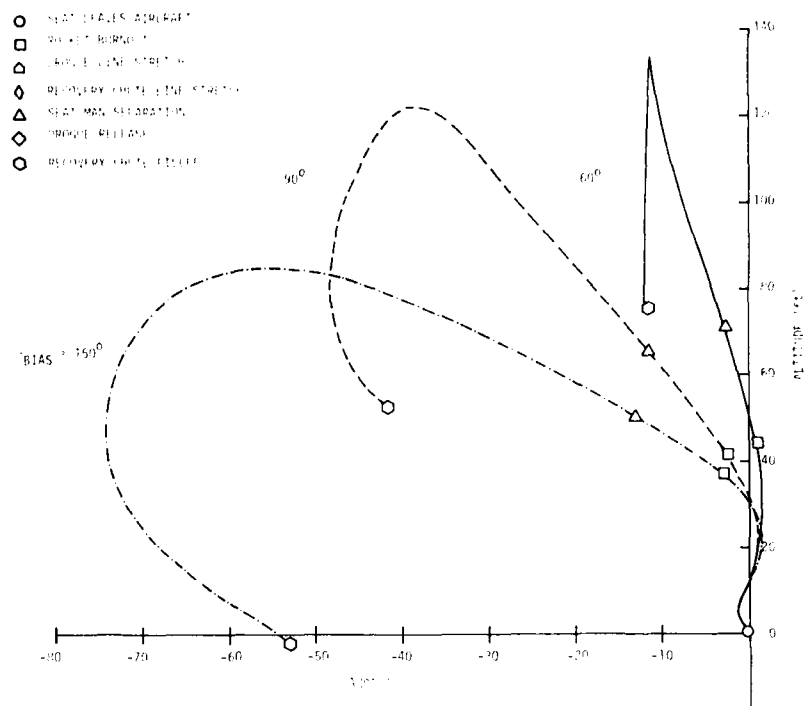
Velocity	Recovery Height		Average g Radical		Unsafe g Radical		RBO Pitch Rate		RBO Yaw Rate	
	Simplified	Complete	Simplified	Complete	Simplified	Complete	Simplified	Complete	Simplified	Complete
0	74.	75.	.567	.557	0	0	913.	973.	74.	107.
240(I)	73.	73.	.959	.961	.159	.164	1527.	1584.	109.	141.
240(II)	131.	141.	.407	.415	0	0	110.	128.	56.	100.
600	24.	17.	.777	.697	.107	.108	35.	24.	19.	-98.

Note: RBO--Rocket burnout

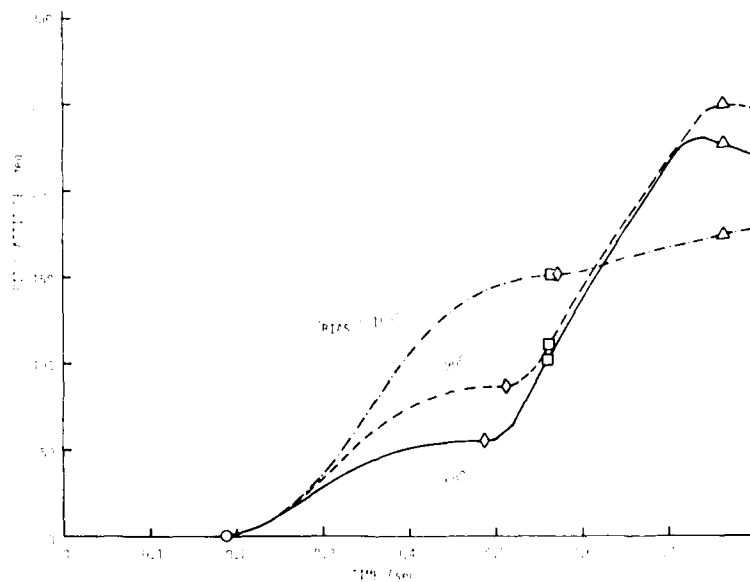
Low Speed System Design

This section describes the effects of control attitude bias and rocket thrust level on low speed trajectories. The low speed, or Mode I, requirements are very different from those for high speed because no drogue chute is used and the aerodynamic forces are much lower. The lower air speed causes a large angle of attack which increases the trim angle of the recovery chute. This large rotation of the seat creates a conflict between trajectory height and g loads on the pilot. We selected the attitude bias and thrust level to optimize that tradeoff.

Attitude Bias Selection--The effect of attitude bias on Mode I trajectories is shown in Figures 18 and 19. Figure 18a shows the 0 knot altitude trajectories. With a bias angle of 60 deg, the response is nearly vertical and full chute is obtained at 74 ft. Increasing the bias results in less recovery height and a bending of the trajectory toward the earth. The 60 deg bias case gives the most height because it directs more rocket impulse toward the earth than the other two cases. This can be seen in the pitch responses shown in Figure 18b. Note that at a pitch angle of about 45 deg the rocket thrusts directly toward the earth since the rocket nozzle is mounted to the seat back at an angle of about 45 deg. Thus the 60 deg bias case clearly produces more vertical thrust than the other two cases.

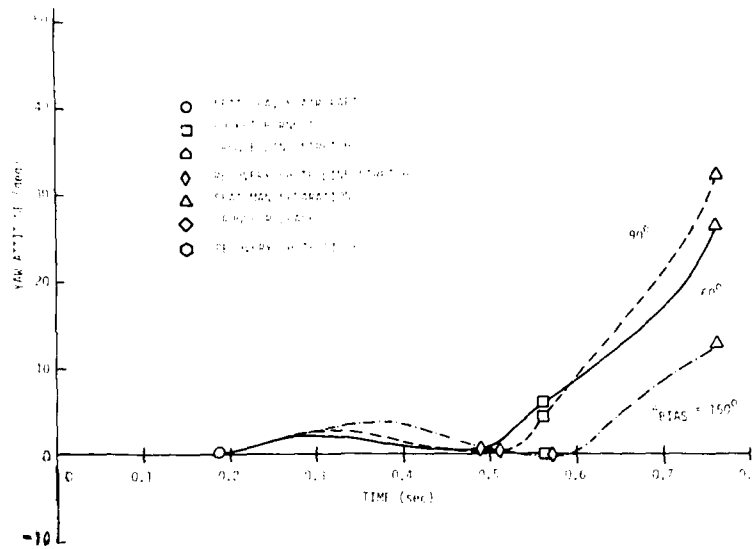


a) Altitude Trajectory



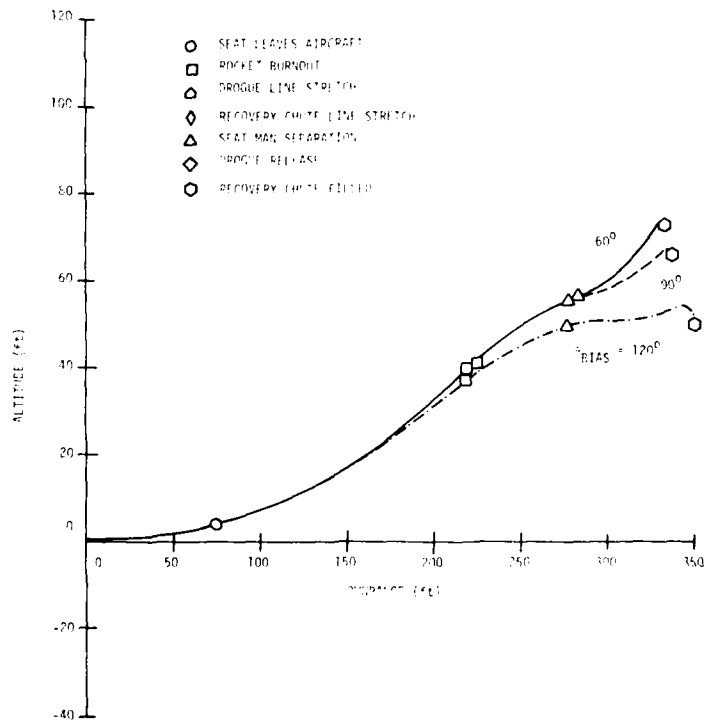
b) Pitch Attitude History

Figure 18. Effect of Pitch Attitude Bias at Zero Knots



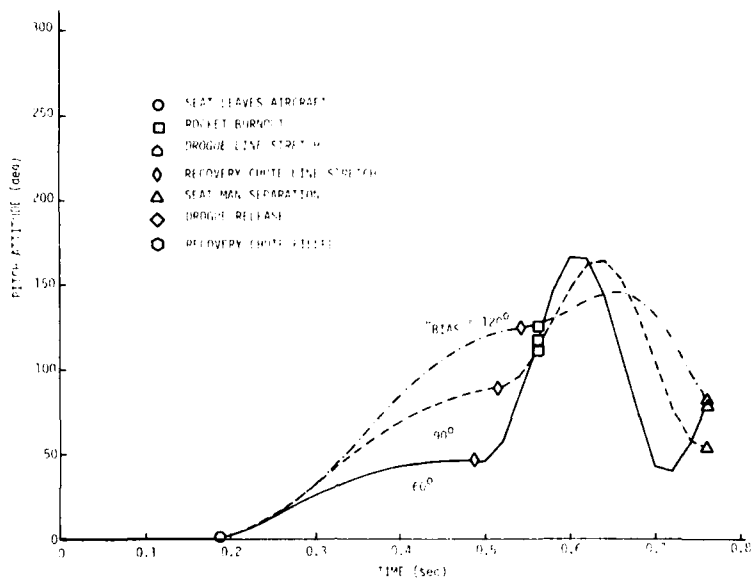
c) Yaw Attitude History

Figure 18. Effect of Pitch Attitude Bias at Zero Knots (concluded)

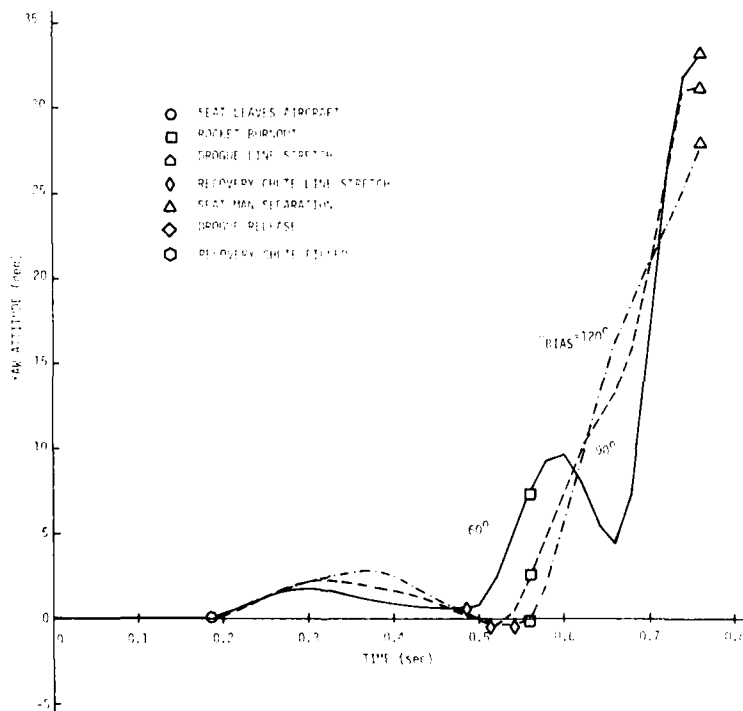


a) Altitude Trajectory

Figure 19. Effect of Pitch Attitude Bias at 240 Knots, Mode I



b) Pitch Attitude History



c) Yaw Attitude History

Figure 19. Effect of Pitch Attitude Bias at 240 Knots, Mode I (concluded)

Figure 18b also shows that the bias angle affects the pitch stability of the seat. The transition to recovery chute is much smoother in the 150 deg bias case than in the other two cases. This is because the recovery chute trim angle is very close to 150 deg.

Control bias does not have much effect on yaw stability. The yaw responses of all three cases are about the same.

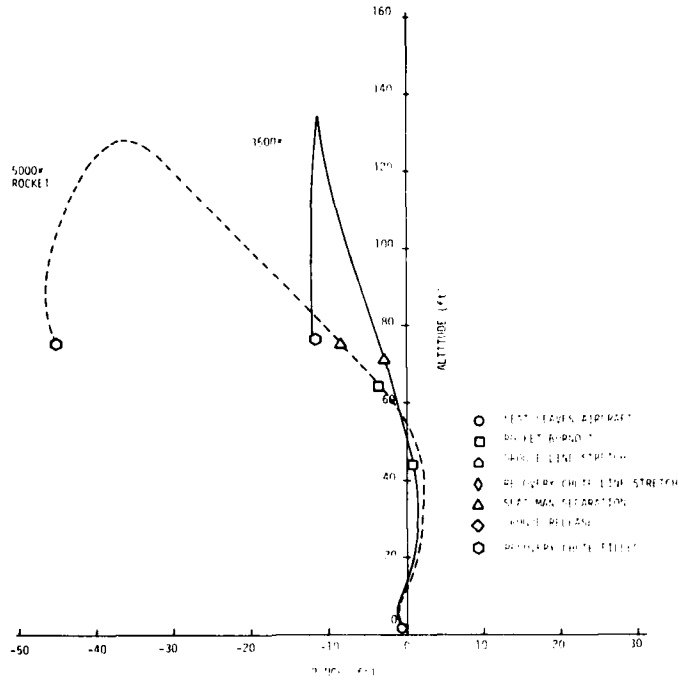
Table 9 shows that the bias angle does not have much effect on g loads either although the average value of the radical is a little larger for 150 deg of bias. This is because the g force at recovery chute line stretch is applied mainly in the spinal direction whereas in the other cases most of the g's are absorbed in the x axis.

With the exception of g loads, the effects of control bias on seat performance are pretty much the same at 240 knots. In Figure 19, increasing the bias reduces the recovery height and improves pitch damping as at 0 knots. However, instead of increasing the g load, increasing the bias decreases the g load at this speed. This difference is due to the difference in aerodynamic forces between the two speeds. At 240 knots the aerodynamic forces are much larger than at 0 knots. Because the aerodynamic forces work to destabilize the system, the seat oscillates much more in pitch at 240 knots (compare Figures 19b and 18b). These oscillations excite the DRI model in the simulation leading to high values for the g radical. The amplitude of the oscillations determines the size of the DRI component of the g radical. Since the oscillations are better damped with larger values of bias angle, the g forces decrease as the bias angle is increased.

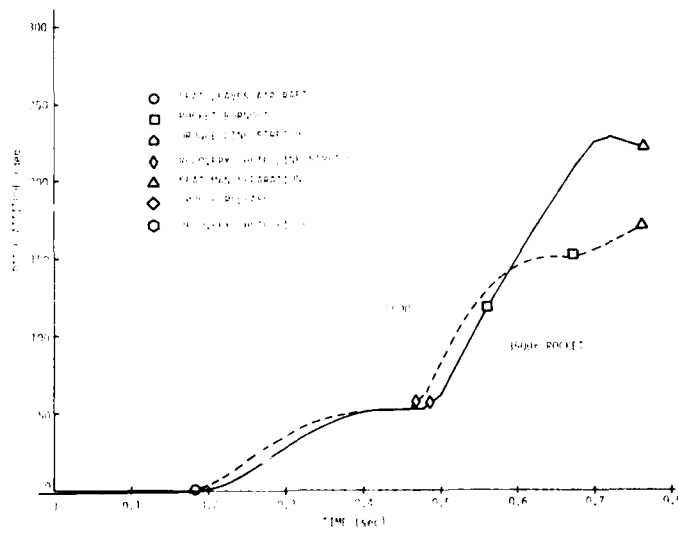
Thrust Level--The 3500 lb thrust level is sufficient for all the performance requirements at low speed. Additional thrust produces some improvement in yaw damping at the expense of increasing g loads. The altitude trajectories of the two thrust levels, shown in Figure 20, are similar.

Pitch responses for the two cases are also very similar. The 5000 lb rocket smooths out the transition to recovery chute.

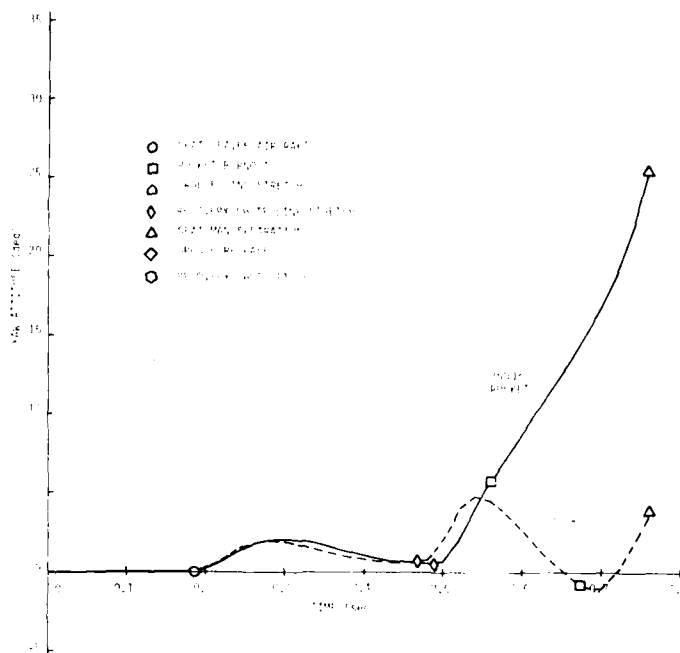
The improvement in yaw damping seen in Figure 20c is due to the longer burn time and larger control force of the 5000 lb rocket. Note that with the larger rocket the TVC system is able to zero out the yaw offset caused by recovery chute line stretch, whereas with the 3500 lb rocket it cannot.



a) Altitude Trajectory



b) Pitch Attitude History  
 Figure 20. Effect of Thrust Level at Zero Knots



c) Yaw Attitude History  
 Figure 20. Effect of Thrust Level at Zero Knots (concluded)

Resultant g forces for the two cases are compared in Table 11. The extra g's which the larger rocket produces come from two sources. First the extra thrust increases the g load by the following amount:

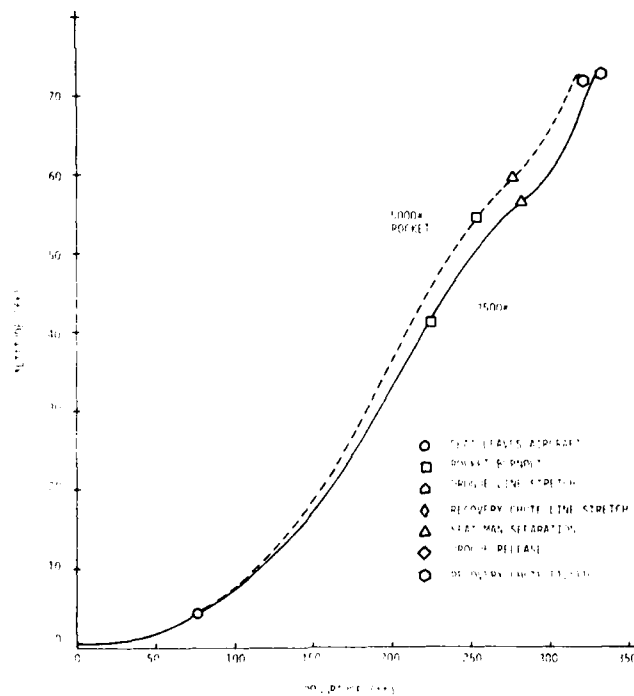
$$\Delta g_{\text{rocket}} = \frac{\Delta F}{W}$$

where  $\Delta F$  is the difference between the thrust of the 5000 lb rocket and that of the 3500 lb rocket (see Figure 16) and  $W$  is the weight of the seat/man system. This contribution is given in the last column of Table 11. The remaining extra g's come from increases in the aerodynamic and parachute forces. The 5000 lb rocket produces more acceleration which causes the seat to fly faster. Since the aerodynamic and parachute forces are functions of dynamic pressure, they are also increased.

The effect of increasing the rocket thrust at 240 knots is the same as at 0 knots. In Figure 21 there is almost no change in recovery height or pitch damping. Yaw control is improved by the extra thrust but only at the expense of increased g load. The unsafe g factor is more than twice as big with the 5000 lb rocket as with the 3500 lb rocket.

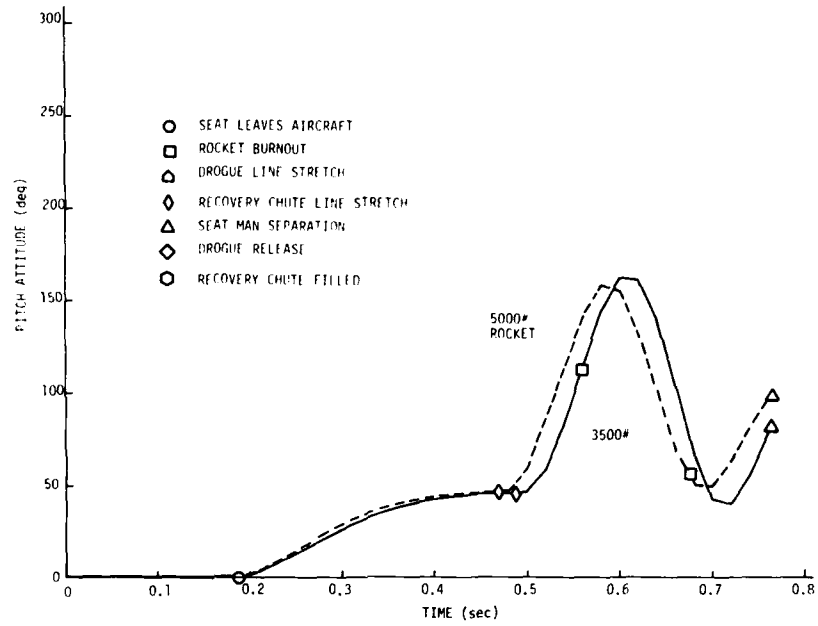
Table 11. Thrust Effect on Acceleration Force  
(0 Knots, 5th Percentile Pilot)

Time (sec.)	Resultant g's		$\Delta g$	$\Delta g_{\text{Rocket}}$
	3500	5000		
0	0	0	0	0
0.1	11.76	11.76	0	0
0.2	12.29	15.85	3.56	3.43
0.3	13.18	15.55	2.37	2.17
0.4	12.29	14.18	1.89	1.18
0.5	4.07	10.72	6.65	1.18
0.6	1.99	12.60	10.61	9.51
0.7	2.67	10.44	7.77	-0.60

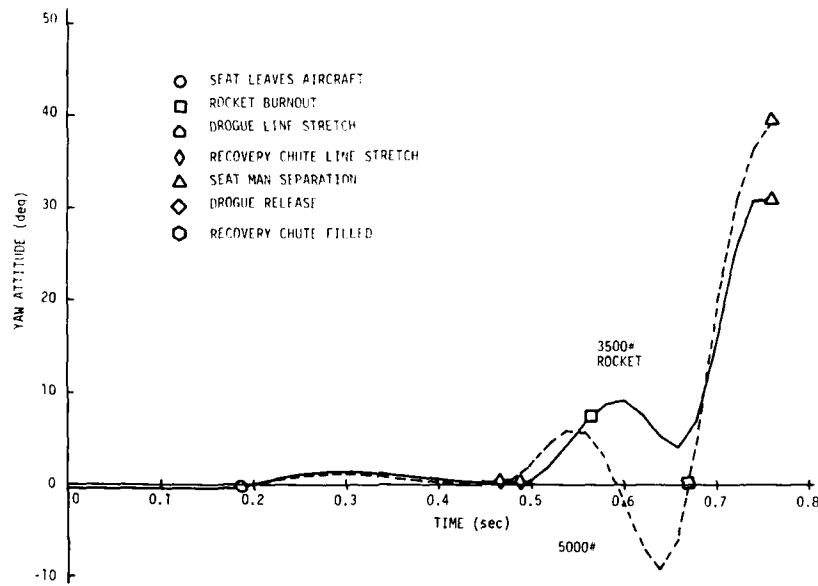


a) Altitude Trajectory

Figure 21. Effect of Thrust Level at 240 Knots, Mode I



b) Pitch Attitude History



c) Yaw Attitude History

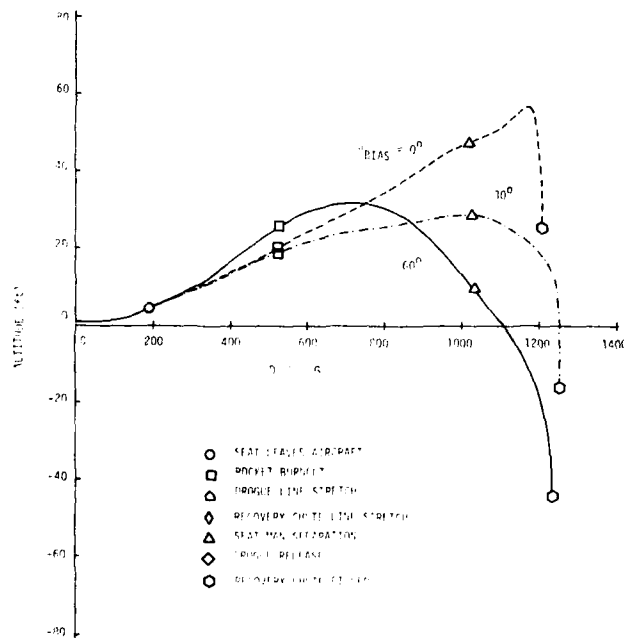
Figure 21. Effect of Thrust Level at 240 Knots, Mode I (concluded)

## High Speed System Design

This section describes the effects of pitch attitude bias, thrust level, and drogue attach point on Mode II trajectories. In summary, a combination of 60 deg bias, 3500 lb thrust, and 6 in higher drogue attach point was chosen.

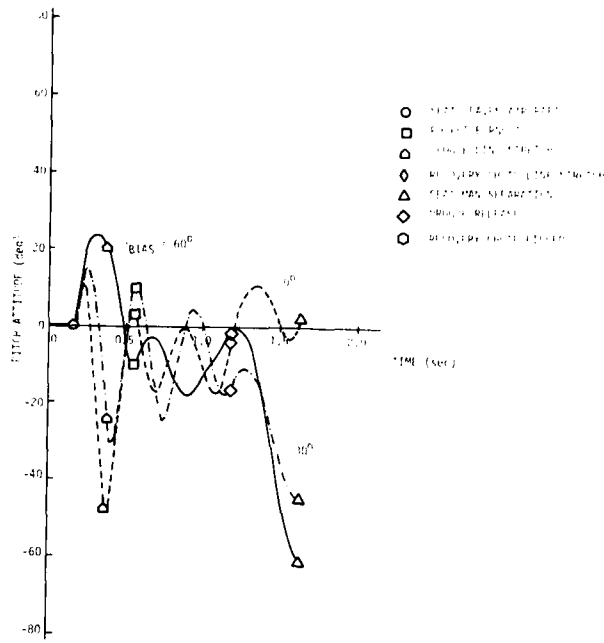
A minimum g load is the design goal. But we must compromise between steady loads and those caused by instability. Unfortunately, the optimal load direction is the least stable altitude for flight. When the drogue tries to hold the g vector along the x axis, the seat yaws. When we pitch the seat back, the seat is stable but the z axis loading increases the load radical. All three design parameters, bias, thrust and attach point, affect this optimization.

Pitch Attitude Bias--The effect of attitude bias is shown in Figures 22 and 23. Attitude bias affects stability and g loads due to changes in aerodynamic forces, drogue trim point, and g vector direction. The seat alone is very unstable at 0 deg angle of attack. If the drogue tries to hold it there, it oscillates in both pitch and yaw. The TVC system is able to stabilize the yaw axis best with a pitch bias of 60 deg. The unsafe g loads in

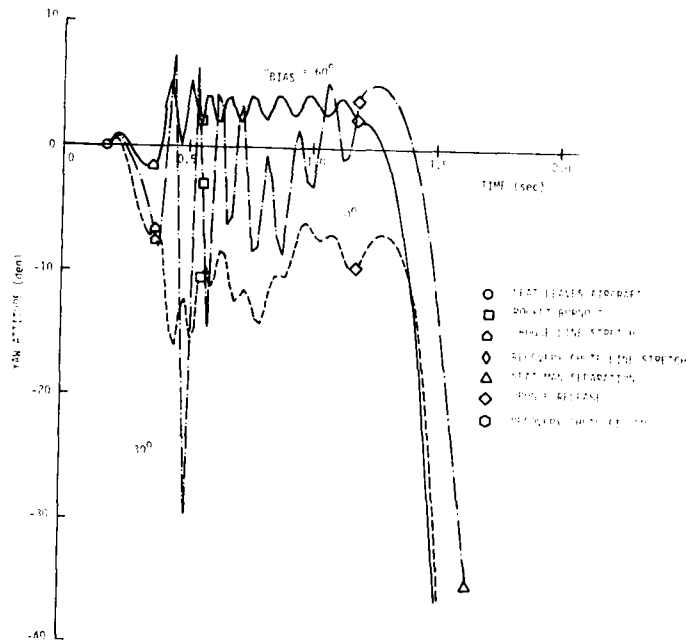


a) Altitude Trajectory

Figure 22. Effect of Pitch Attitude Bias at 600 Knots

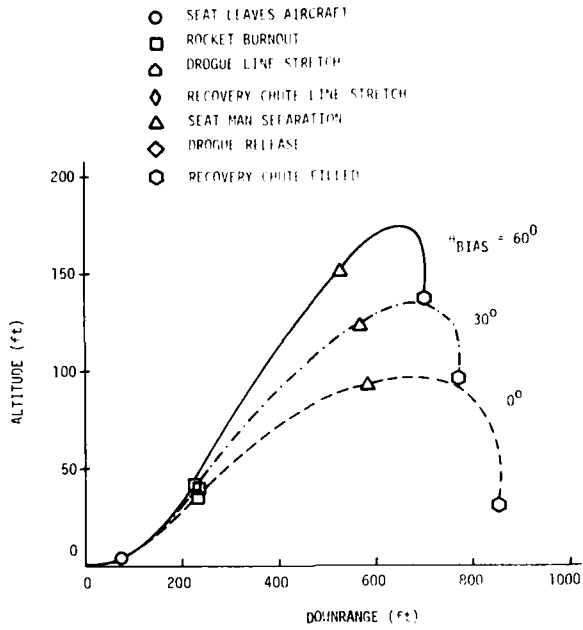


b) Pitch Attitude History

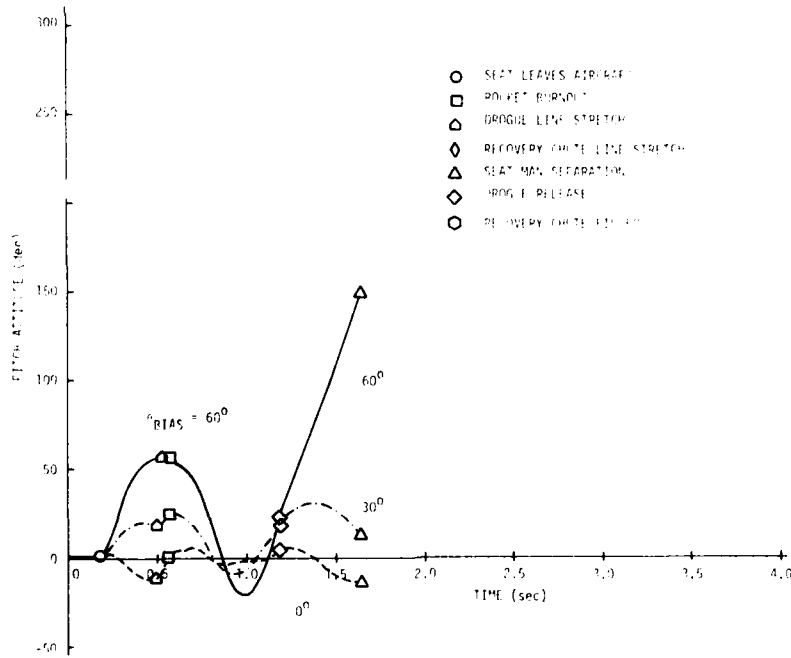


c) Yaw Attitude History

Figure 22. Effect of Pitch Attitude Bias at 600 Knots (concluded)

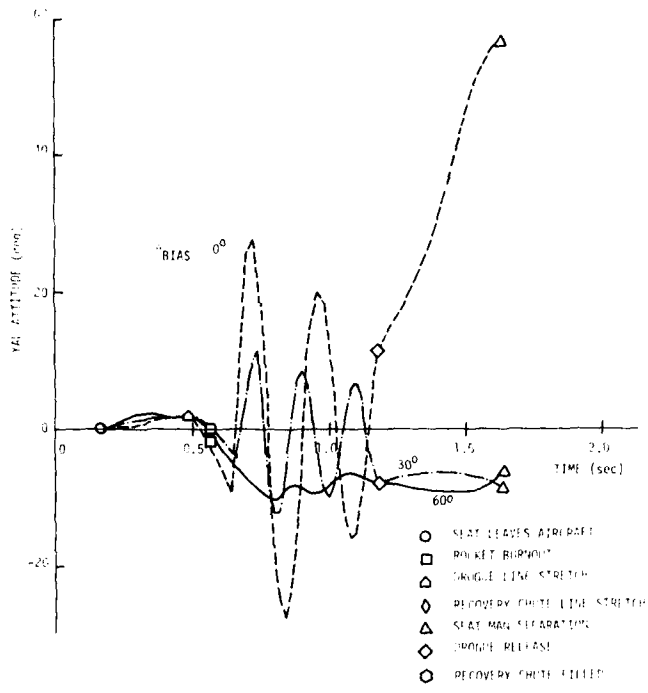


a) Altitude Trajectory



b) Pitch Attitude History

Figure 23. Effect of Pitch Attitude Bias at 240 Knots, Mode II



c) Yaw Attitude History

Figure 23. Effect of Pitch Attitude Bias at 240 Knots, Mode II (concluded)

the y axis are reduced with some increase in the z axis to obtain a net reduction in the g radical. Figure 22a shows that decreasing the bias does not reduce recovery height as expected but increases it instead. The smaller bias angles give more height because the seat rolls upside down in these two cases. This reverses the direction of the aerodynamics lift force acting on the seat from down to up producing more height. The data in Table 12 show this effect more clearly. Note that as the seat rolls through 90 deg in the 0 deg bias case, the aerodynamic force component changes sign.

Table 12 also shows another reason why the case with 0 deg bias gets more height. At drogue line stretch (0.4 sec), the aerodynamic force component in the 0 deg bias case produces positive lift, whereas in the 60 deg bias case it acts in the opposite direction. The reason for this difference is that the seat is pitched forward much more in the 0 deg bias case (Figure 22b).

The effect of control bias on pitch response is shown in Figure 22b. The results show that a large bias is needed to keep the seat from pitching forward during the early part of the trajectory. It is important to limit the forward pitching motion to minimize the

Table 12. Effect of Attitude Bias on Roll Attitude and Acceleration Forces  
(600 Knots, 5th Percentile Pilot)

Time (sec)	F <sub>Z</sub> * Aero (lb)		F <sub>Z</sub> * Drogue (lb)		Roll Angle (deg)	
	$\theta_{\text{Bias}} = 60$	$\theta_{\text{Bias}} = 0$	$\theta_{\text{Bias}} = 60$	$\theta_{\text{Bias}} = 0$	$\theta_{\text{Bias}} = 60$	$\theta_{\text{Bias}} = 0$
.4 (Line Stretch)	-1976	+1188	-1735	-1123	4.	26.
.6	-1661	-689	-342	-266	10.	70.
.8	-803	+379	-59	-122	10.	123.
1.0	-580	+501	+49	-125	8.	170.
1.2 (Drogue Release)	-306	+284	0	0	4.	212.

\* Negative F<sub>Z</sub> points toward the earth.

effect of drogue line stretch on the pilot. The pilot cannot withstand the shock of line stretch very well at negative pitch angles since he cannot tolerate more than 12 g's in the negative z direction. The g load summaries in Table 13 demonstrate this fact. Note that at line stretch, roughly 0.4 sec, the 0 deg bias case has more g's in the negative z direction than the other two cases and also has the largest radical.

Figure 22b also shows that increasing the bias improves the pitch stability of the seat. Pitch stability is improved because the aerodynamic pitching moment acting on the seat gets smaller as the pitch angle increases.

The only significant effect of control bias on yaw response (Figure 22c) is that, with 30 deg of bias, the system is much less stable than with either a larger or smaller bias. This results in much higher g loads in the y axis during the drogue phase of the flight (Table 13).

The effect of  $\theta_{\text{bias}}$  on the pilot g load is summarized in Table 9. Note that increasing the bias from 0 to 30 deg produces an increase in the unsafe radical, whereas further increasing the bias to 60 deg produces a decrease. The reason is the larger yaw angle discussed above. The 60 deg case has the lowest radical because increasing the bias improves the ability of the pilot to withstand the shock of drogue line stretch.

Table 13. Effect of Attitude Biases on Acceleration Forces (600 Knots, 5th Percentile Pilot)

Time (sec)	$\theta_{\text{Bias}} = 0^\circ$			$g_x$			$g_y$			$g_z$			DRI			Radical			
	0°	30°	60°	0°	30°	60°	0°	30°	60°	0°	30°	60°	0°	30°	60°	0°	30°	60°	
	0.0	0.00	0.00	0.00	0.00	0.00	0.00	0.00	0.00	0.00	0.00	0.00	0.00	0.00	0.00	0.00	0.00	0.00	0.00
0.1	-.96	-.96	-.96	-.00	-.00	-.00	11.67	11.67	11.67	10.51	10.51	10.51	0.00	0.00	0.00	.80	.80	.80	.80
0.2	-16.94	-14.91	-13.20	.61	.71	.77	7.59	6.52	4.86	5.76	4.97	4.53	-2.47	-2.47	-2.47	.75	.82	.85	.85
0.3	-12.18	-10.32	-5.18	-1.87	-1.89	-.74	-2.49	2.32	11.76	-2.47	5.87	14.80	-8.49	-8.49	-8.49	.71	.55	.94	.94
0.4	-34.25	-40.07	-35.66	2.40	-.88	-.96	-30.14	-19.15	17.42	-30.14	-19.15	17.42	9.33	9.33	9.33	2.76	2.08	1.48	1.48
0.5	-37.68	-33.81	-42.28	1.09	-23.20	-.02	9.20	4.13	.72	9.20	4.13	.72	-1.31	-1.31	-1.31	1.41	2.17	1.45	1.45
0.6	-30.84	-24.16	-32.36	-1.80	-3.39	.40	-.63	4.34	-2.98	-.63	4.34	-2.98	-4.47	-4.47	-4.47	1.08	.91	1.13	1.13
0.7	-23.80	-19.35	-24.46	-.62	1.05	-.46	-4.89	-5.78	-.41	-4.89	-5.78	-.41	-1.56	-1.56	-1.56	.88	.96	.83	.83
0.8	-18.86	-19.35	-19.73	-.65	.25	-.27	-2.10	-4.23	-2.90	-2.10	-4.23	-2.90	1.50	1.50	1.50	.65	.74	.72	.72
0.9	-14.94	-14.69	-15.79	-.37	-.65	-.08	.16	1.22	-3.15	.16	1.22	-3.15	-2.06	-2.06	-2.06	.51	.52	.59	.59
1.0	-13.08	-12.32	-13.48	-.64	-.99	.08	-1.92	.79	-2.06	-1.92	.79	-2.06	-1.50	-1.50	-1.50	.46	.43	.48	.48
1.1	-11.10	-11.64	-11.57	.08	-.20	-.01	-2.37	-2.03	-.35	-2.37	-2.03	-.35	-1.50	-1.50	-1.50	.42	.42	.40	.40
1.2	-3.77	-3.95	-3.49	-.01	.03	-.10	-.99	-1.41	-.47	-.99	-1.41	-.47	.25	.25	.25	.15	.18	.18	.18
1.3	-2.91	-3.88	-3.47	-.18	.16	-.23	-.09	-1.38	-.61	-.09	-1.38	-.61	.57	.57	.57	.11	.17	.18	.18
1.4	-3.59	-3.46	-3.67	-1.09	.01	-.69	-.45	-1.26	-1.32	-.45	-1.26	-1.32	-.05	-.05	-.05	.15	.16	.22	.22
1.5	-2.87	-3.37	-2.99	-2.38	-.26	-2.06	-1.04	-1.49	-1.57	-1.04	-1.49	-1.57	-1.66	-1.66	-1.66	.21	.17	.23	.23
1.6	-1.84	-2.81	-2.01	-3.06	-.50	-2.11	-1.36	-1.57	-1.85	-1.36	-1.57	-1.85	-1.85	-1.85	-1.85	.25	.16	.22	.22

Control bias affects performance in a more predictable way at 240 knots. There is no rolling at this speed so that increasing the bias increases trajectory height similar to the results obtained in Mode I.

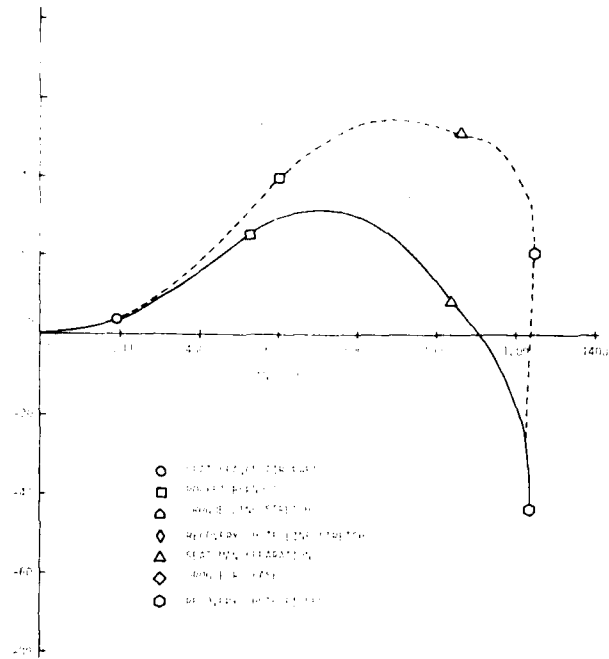
The effect on pitch stability is shown in Figure 23b. The response is less stable with a large bias angle because the bias angle is different from the trim angle. The TVC system wants to hold the seat at the bias angle, whereas the drogue wants to turn the seat to the drogue trim angle (about -10 deg). The TVC system wins during rocket burn because the control forces are larger than the aerodynamic and drogue forces at this speed. However, at rocket burnout the response is destabilized as the seat heads for the drogue trim angle.

Table 9 shows the effect on g load. Increasing the bias from 0 to 30 deg lowers the g radical because of the improvement in yaw stability (Figure 23c). Raising it further to 60 deg has the opposite effect because this change shifts a significant portion of the total g's during rocket burn from the x axis to the z axis.

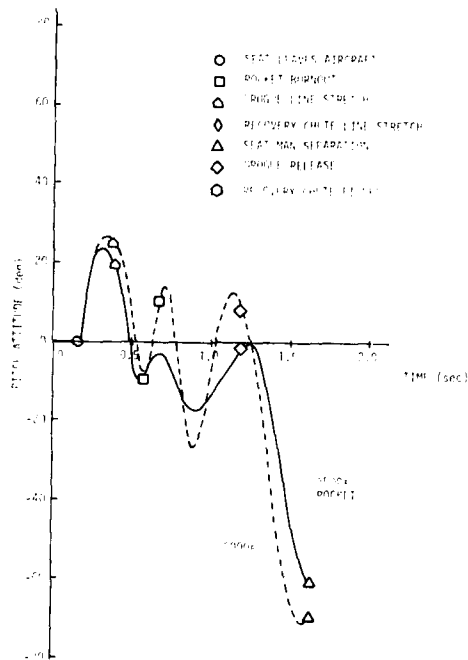
Thrust Level--The major advantages of the 5000 lb rocket over the 3500 lb rocket are that it has increased trajectory height and better yaw damping. Figure 24a shows that the extra thrust increases recovery height by over 60 ft. The improvement in yaw damping is shown in Figure 24c. Since the yaw damping of the 3500 lb rocket is already pretty good, the improvement does not affect the y component of the g forces.

The disadvantages of extra thrust are poorer pitch stability and higher g's. Figure 24b shows the change in pitch damping. Since the 5000 lb rocket has more control authority and a longer burn time than the smaller rocket, it does not settle in on the drogue trim angle nearly as well. However, if the drogue trim angle and bias angle were compatible, the 5000 lb rocket would be more stable than the 3500 lb rocket.

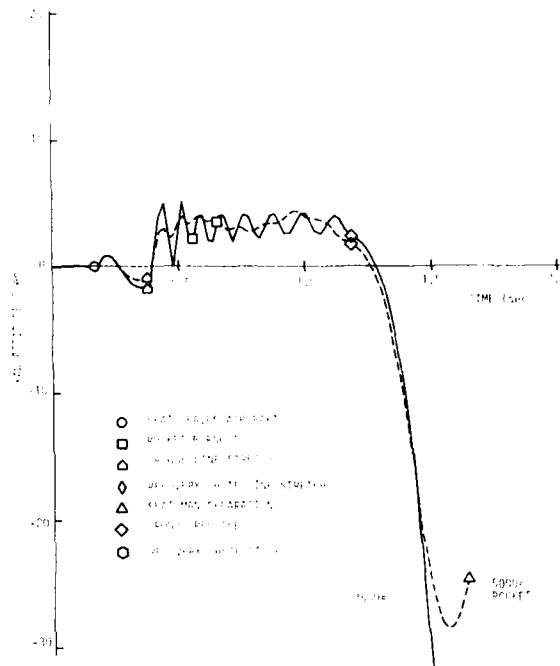
The 5000 lb rocket has a higher unsafe g radical for three reasons: 1) the extra thrust produces more acceleration, 2) the aerodynamic and parachute forces acting on the seat are bigger because the seat flies faster, and 3) more of the g load is applied in the z axis because pitch damping is not as good. The first two of these are also the reasons for higher g loads in low speed ejections.



a) Altitude Trajectory



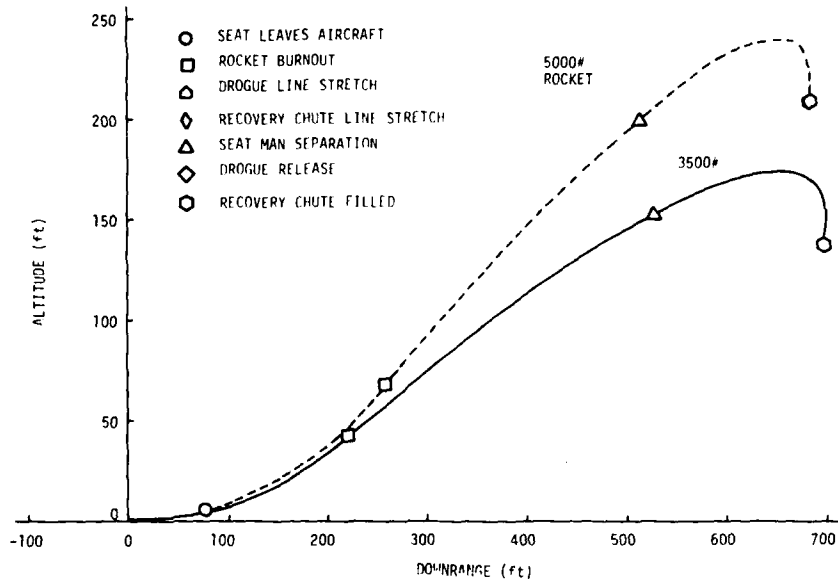
b) Pitch Attitude History  
 Figure 24. Effect of Thrust Level at 600 Knots



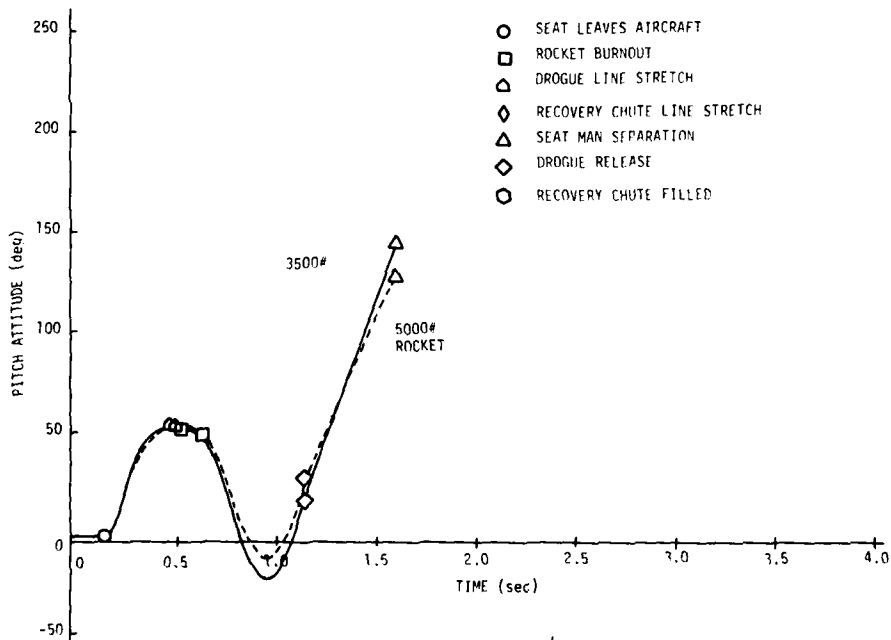
c) Yaw Attitude History  
 Figure 24. Effect of Thrust Level at 600 Knots (concluded)

Thrust affects trajectory height and g load in the same way at 240 knots. Increasing the thrust results in more recovery height and a larger g radical. However, the effects on pitch and yaw are different. Figure 25b shows that extra thrust has very little effect on pitch attitude at 240 knots, whereas at 600 knots it has a big effect (Figure 24b). Increasing the thrust at 600 knots destabilizes the pitch response because it aggravates the difference between the bias angle and the drogue trim angle. This does not happen at 240 knots because the drogue forces are much smaller during rocket burn. The forces are smaller because the dynamic pressure is lower and the drogue opens more slowly.

The difference in drogue forces also explains why extra thrust affects yaw stability differently at 240 knots. Increasing the thrust destabilizes yaw response. Figure 25c shows that extra thrust causes the seat to oscillate about the yaw axis. This oscillation results from yaw offset in the drogue trim angle. The TVC system wants to maintain zero yaw offset while the drogue wants to trim the seat at about -10 deg. Since drogue force is smaller than TVC force at 240 knots, the TVC system wins during rocket burn. The oscillation gets started as the seat heads for the drogue trim angle at rocket burnout.

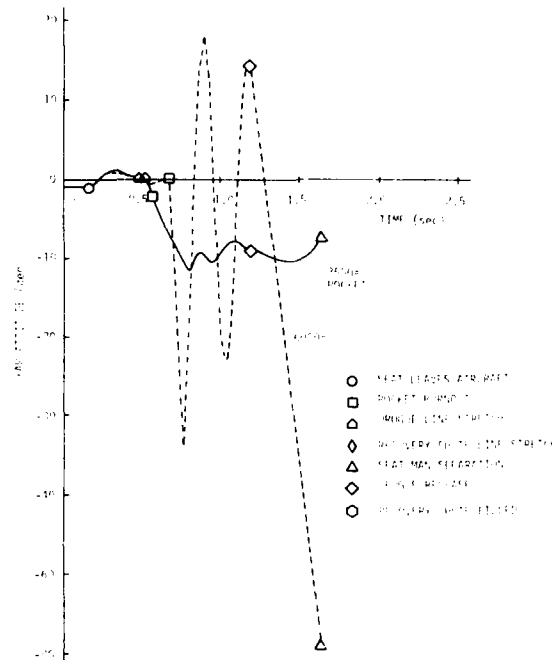


a) Altitude Trajectory



b) Pitch Attitude History

Figure 25. Effect of Thrust Level at 240 Knots, Mode II



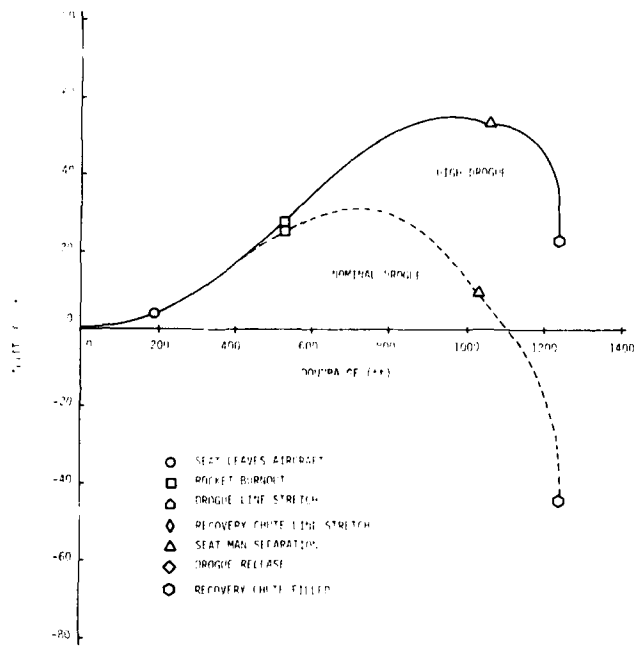
c) Yaw Attitude History  
 Figure 25. Effect of Thrust Level at 240 Knots, Mode II  
 (concluded)

Note that the oscillation does not occur with the 3500 lb rocket because rocket burnout occurs sooner. This effect does not show up at 600 knots because the drogue has more authority than the TVC system at high speeds.

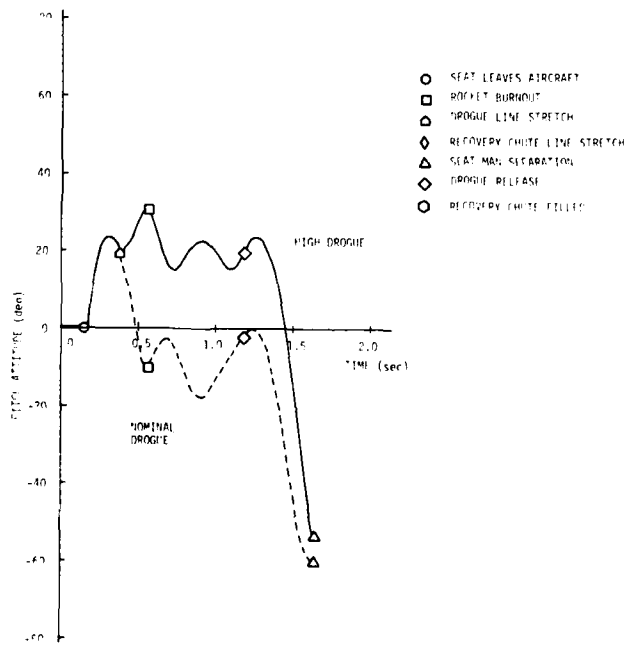
Drogue Attach Point--Raising the drogue attachment points on the seat is an effective means of increasing recovery height at high speed. It also improves pitch stability somewhat. However, spinal g loads are increased.

Recovery height is increased because the drogue holds the seat in a pitch-up position throughout rocket burn (Figure 26b). This increases the height by directing more thrust toward the earth in the same manner as increasing  $\theta_{bias}$  increases recovery height at lower speeds.

Pitch stability is improved because the drogue trim angle is closer to the bias trim angle. Figure 26b shows that, with the drogue moved up, the seat is already at the drogue trim angle at line stretch. With the drogue in the nominal position, the seat must pitch forward about 30 deg to trim out.

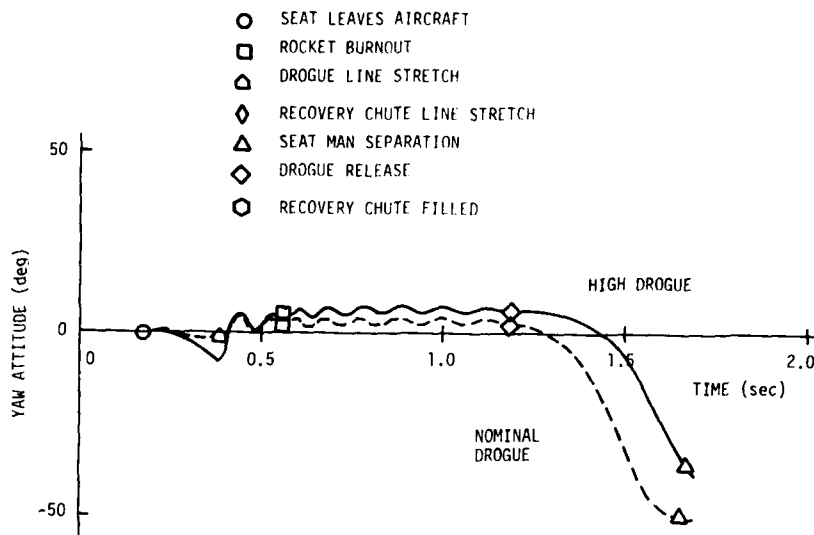


a) Altitude Trajectory



b) Pitch Attitude History

Figure 26. Effect of Drogue Attach Point at 600 Knots

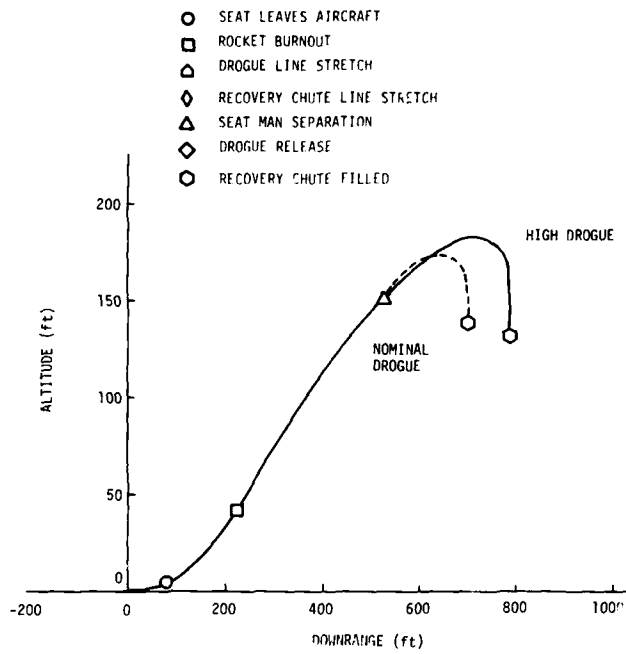


c) Yaw Attitude History  
 Figure 26. Effect of Drogue Attach Point at 600 Knots  
 (concluded)

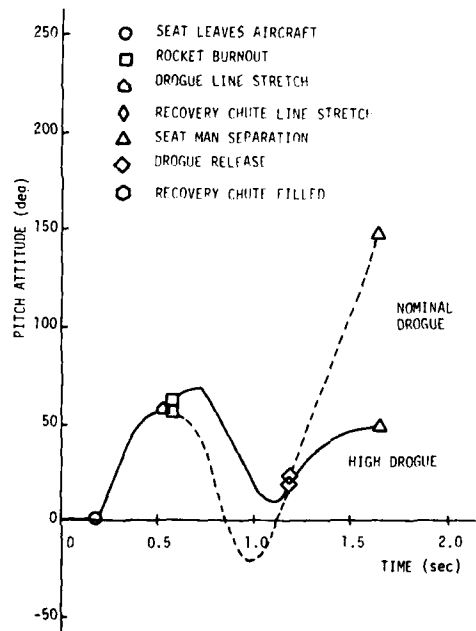
The difference in drogue trim angles also affects the g load. Moving the drogue up increases the g radical since it increases the z component of the g vector and decreases the x component.

Changing the drogue attach points has very little effect on the yaw response (Figure 26c).

Drogue position has the same effect on pitch attitude and g load at 240 knots; however, the effect on recovery height is quite different. Figure 27a shows that raising the drogue does not change the trajectory very much. The reason for this difference is that drogue chute line stretch occurs much later at 240 knots than at 600 knots (compare Figure 27b with Figure 26b). Trajectory height is not affected at 240 knots because rocket burn is almost over before line stretch occurs. Drogue position also affects yaw damping differently at 240 knots. Figure 27c shows that raising the drogue excites a yaw oscillation.

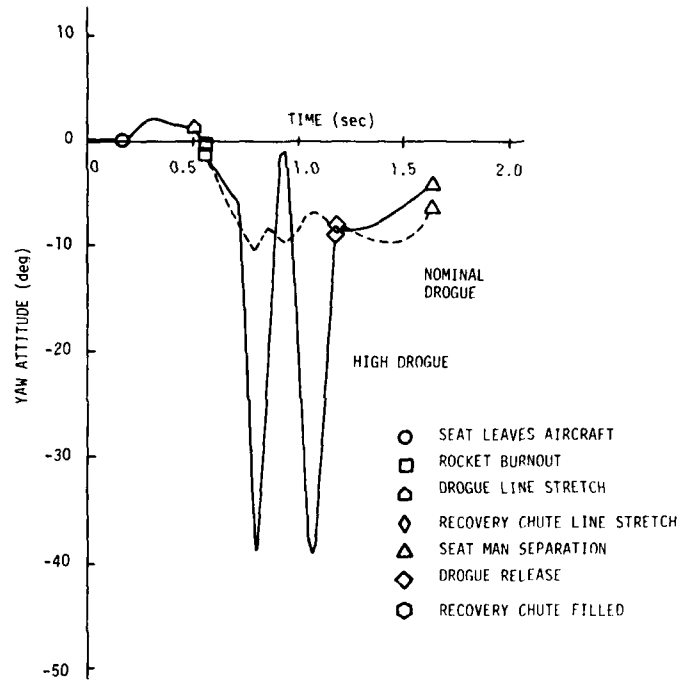


a) Altitude Trajectory



b) Pitch Attitude History

Figure 27. Effect of Drogue Attach Point at 240 Knots, Mode II



c) Yaw Attitude History  
 Figure 27. Effect of Drogue Attach Point at 240 Knots, Mode II (concluded)

## SECTION 3

### FTVC SYSTEM DESIGN AND TEST RESULTS

Two stages of hardware mechanization were built and tested. We fabricated a breadboard fluidic system with interchangeable components. We then fabricated an integrated fluidic circuit shown in Figure 28 from the design parameters obtained from the breadboard. The breadboard FTVC system shown in Figure 29, including the nozzle actuator, met all the performance requirements. The prototype system was fabricated using production electroforming techniques. The prototype system met all performance requirements except for null bias stability over the temperature range.

The null bias instability was caused by nozzle asymmetry in the fluid amplifier mold. Experience with one amplifier has shown that this asymmetry can be reduced with tighter tolerances in mold fabrication.

The breadboard system tests and prototype component tests demonstrated the feasibility of the all fluidic concept. The test results are described below.

#### SYSTEM DESCRIPTION

The fluidic TVC system consists of a vortex rate sensor, fluidic controller, servo-actuator and rocket nozzle assembly, and a hydraulic power source. The seat pitch axis and the seat yaw axis have independent controls. TVC is accomplished by vectoring a ball and socket type rocket nozzle in pitch and yaw.

A single axis block diagram is shown in Figure 30 with the dynamic transfer functions of each component. These transfer functions were defined in the simulation analysis of Section 2. Figure 31 shows the overall dynamic response required. Pitch and yaw axes have identical requirements.

Figure 32 shows the complete FTVC system circuit diagram. Figure 33 describes the component operating parameters necessary for impedance matching and meeting system performance specifications. Table 14 also defines these component operating parameters.

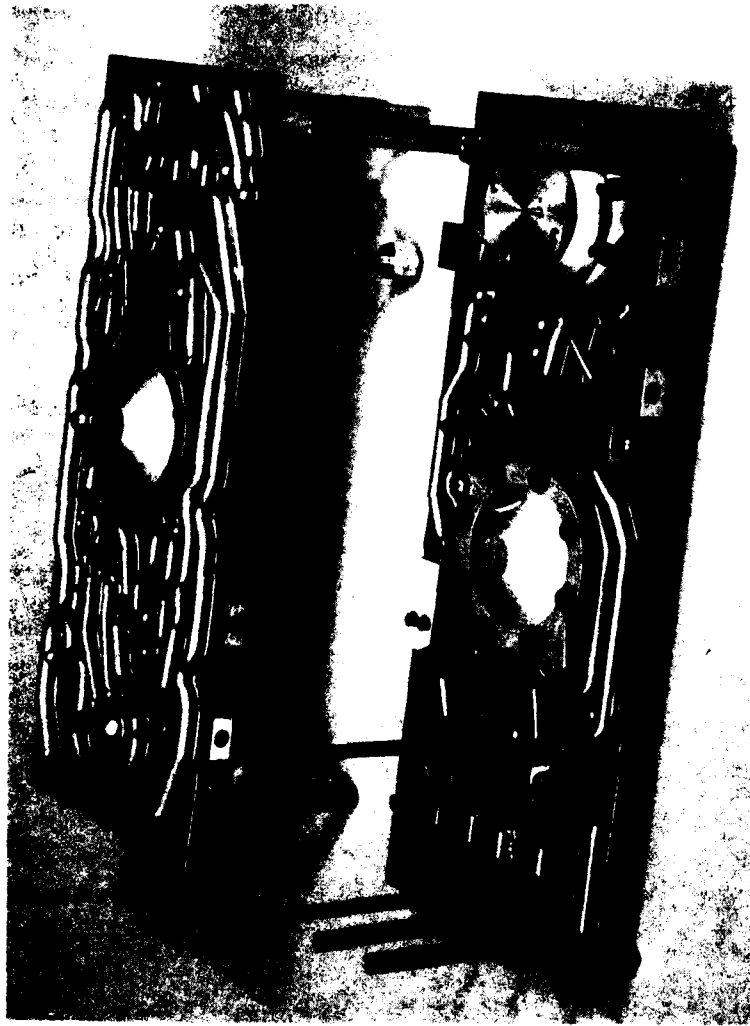
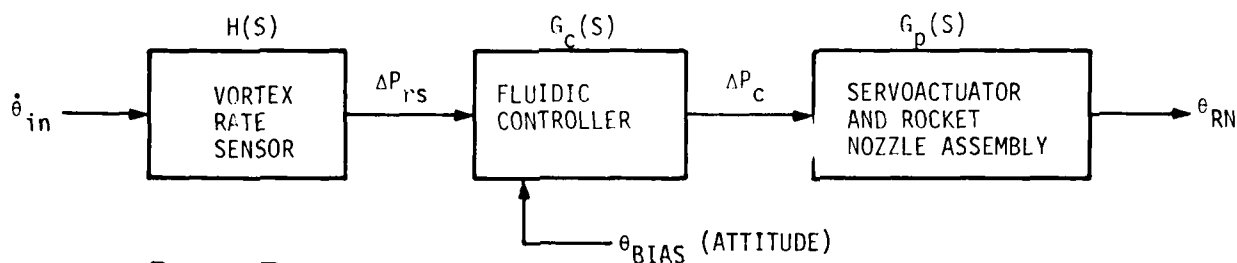


Figure 28. Assembled Attitude Controllers



Figure 29. Breadboard FTVC System



$$H(s) = -K_{RS} \left[ e^{-0.009s} \right] \quad (\text{RATE SENSOR DYNAMICS})$$

$$G_c(s) = -K_c \left[ \frac{0.10s+1}{2.5s+1} \right] \quad (\text{FLUIDIC CONTROLLER DYNAMICS})$$

$$G_p(s) = -K_p \left[ \frac{1}{0.011s+1} \right] \quad (\text{SERVO AND ROCKET NOZZLE DYNAMICS})$$

$$\frac{\theta_{RN}}{\dot{\theta}_{in}} = 0.50 \frac{\text{deg}_{RN}}{\text{deg/sec}_{rate}} \quad \text{AT } \omega = 1.0 \text{ rad/sec}$$

Figure 30. Single Axis FTVC Block Diagram

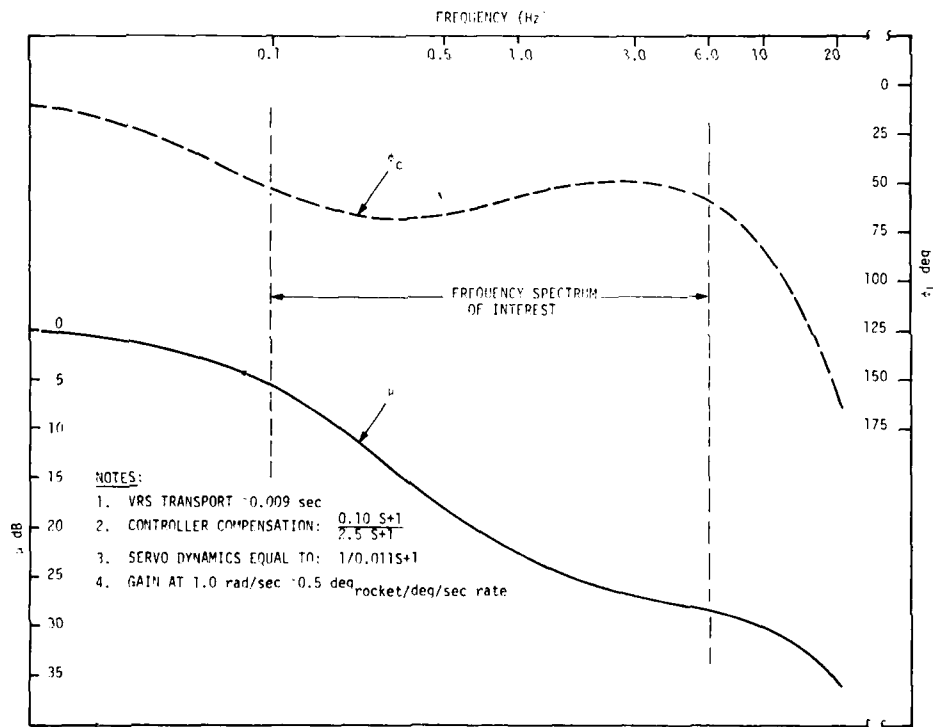


Figure 31. FTVC Design Goal Dynamic Response

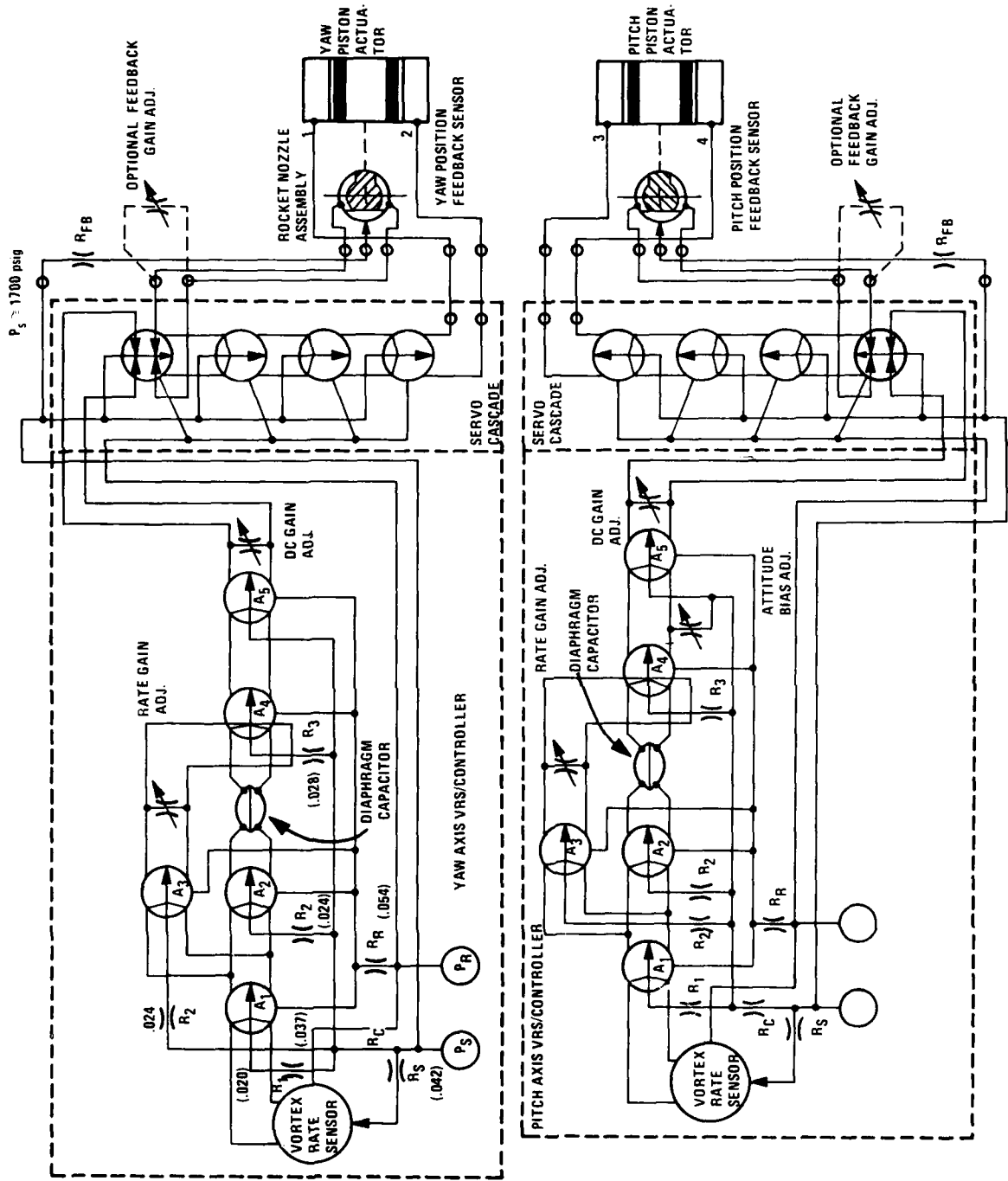


Figure 32. Fluidic Attitude Control System Schematic

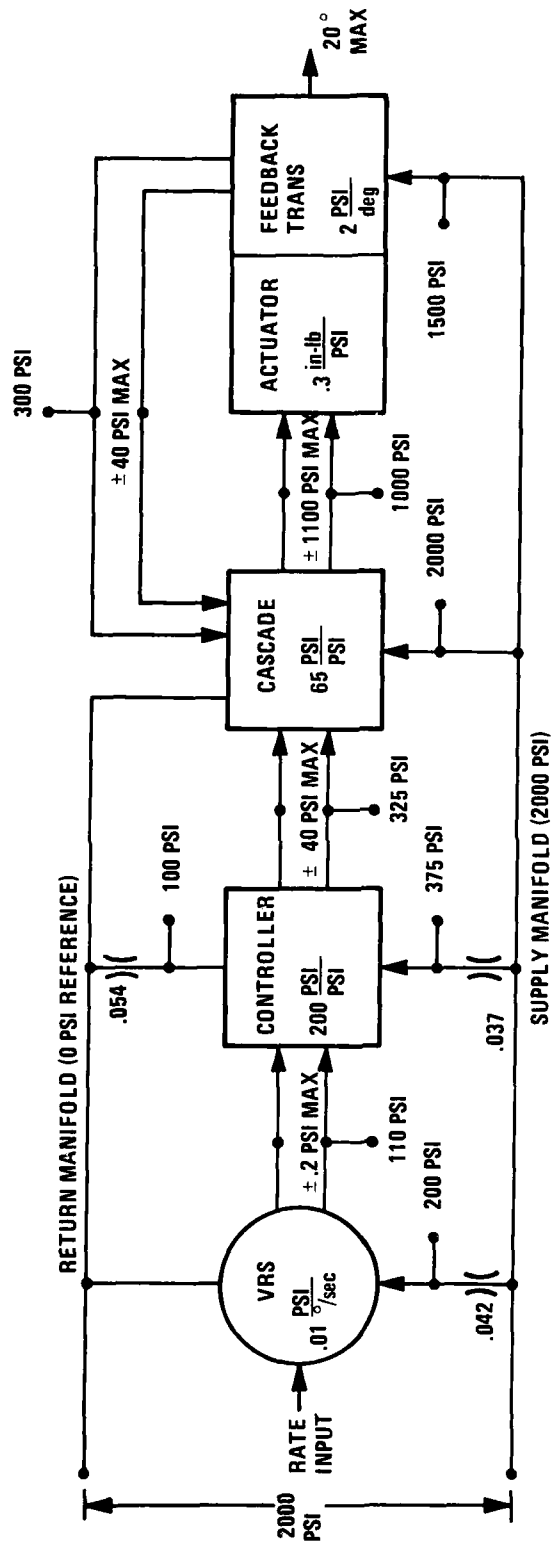


Figure 33. FTVC System Operating Schematic

Table 14. FTVC System Operating Parameters

Parameter	VRS	Controller	Cascade	Actuator	Feedback Transducer
Gain:					
Maximum Design operating point	$.01 \frac{\text{psi}}{\text{deg/sec}}$	600 psi/psi 200	65 psi/psi -	$.3 \frac{\text{in-lb}}{\text{psi}}$ -	20 psi/deg 2
Output signal:					
Maximum	Infinite	250 psi	1100 psi	330 in-lb	40 psi
Maximum nozzle angle	.2 psi	40 psi	-	150 in-lb	
Output static level	110 psi	325 psi	1000 psi	-	325 psi
Supply pressure	200 psi	375 psi	2000 psi	-	1500 psi
Return pressure	0	100 psi	0	-	325 psi

## FLUIDIC CONTROLLER

The fluidic controller includes the rate sensor, signal amplifiers, capacitor, gain adjustment, and bias adjustment. It senses seat rate and integrates the rate to obtain seat attitudes. It drives the servovalve with a signal containing the necessary proportions of rate and attitude to stabilize the seat.

The controller is shown in Figure 34. The components are described in Figures 35 and 36. It consists of an electroformed manifold and amplifier circuit. The rate sensor and capacitor diaphragm are mounted to this manifold. The supply and exhaust flow through this manifold. The yaw and pitch circuits are identical except for the orientation of the rate sensor.

### Description

The VRS/controller supply flow is obtained from a hydraulic power source. A line resistance is used to split the supply flow for VRS/controller and servoactuator as shown in Figure 33. Another resistor is used to split the VRS/controller supply

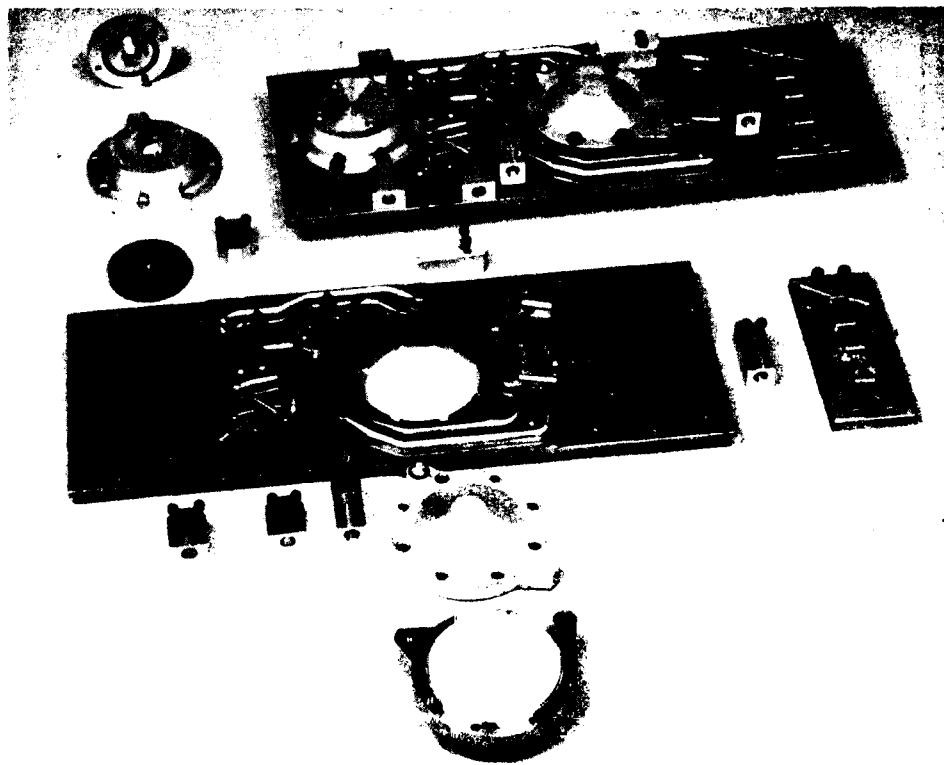


Figure 34. Fluidic Controller Disassembled

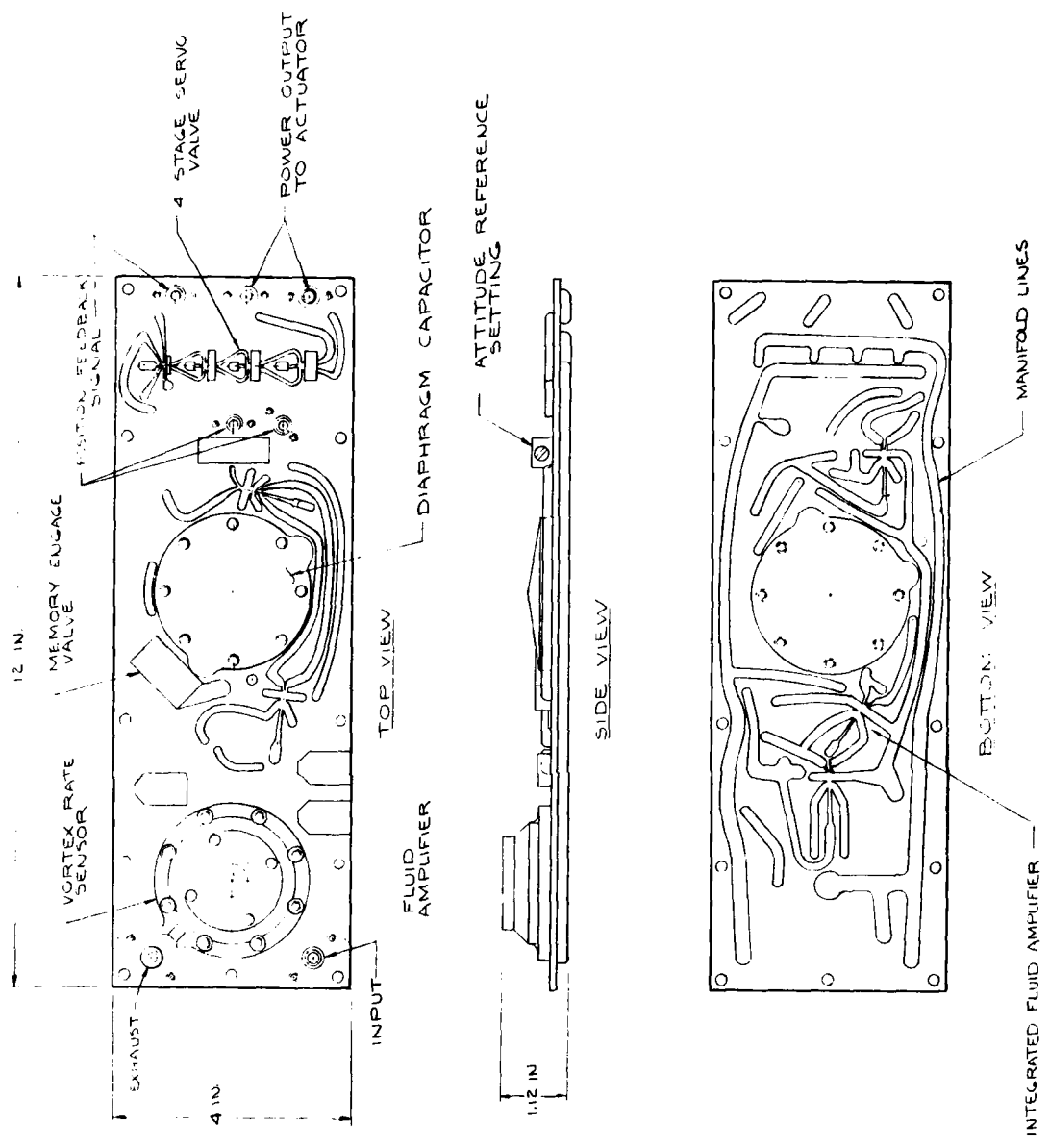


Figure 35. One-Axis Fluidic Rate Sensor and Amplifier

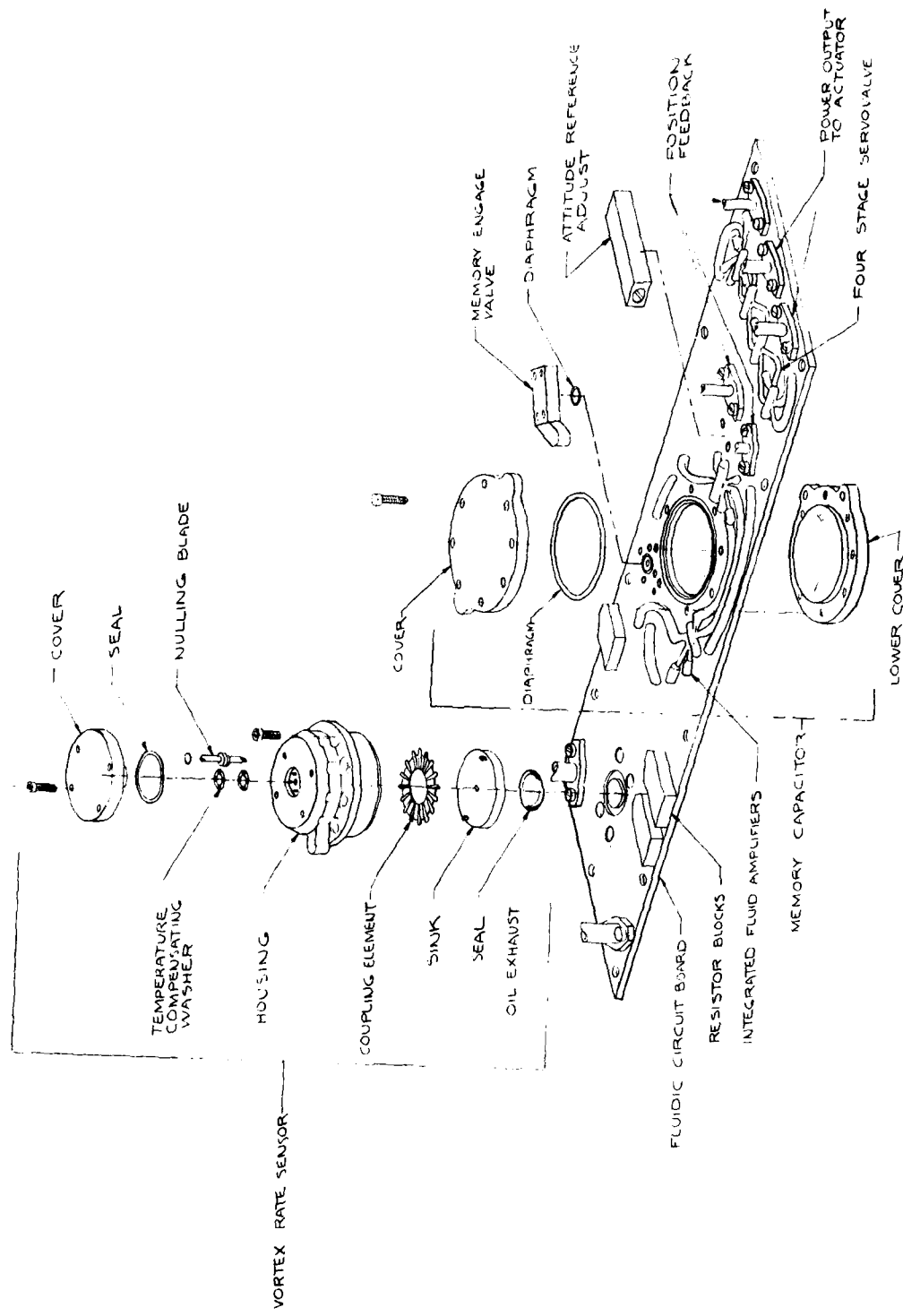


Figure 36. Detail of Fluidic Attitude Controller

flow between the VRS and the controller. In the controller section, fluid amplifier supply and return resistors are used to impedance match the amplifiers for the desired gain values. Amplifiers all have the same power nozzle size. These orifices also impedance match the VRS to the controller.

The controller dynamic requirement is expressed in the form of a lag-lead transfer function with the numerical value of:

$$C(S) = k_c \frac{0.10S+1}{2.5S+1}$$

The controller shaping is produced by combining a straight-through signal and a lagged signal in a jet summing amplifier ( $A_4$ ). The lag time constant is a short-term memory. It depends on the output port resistance of amplifier  $A_2$ , the input resistance of amplifier  $A_4$ , and the size of the capacitor across the output of amplifier  $A_3$ . The shunt resistor across the  $A_3$  output controls the straight-through signal gain.

The lag path corner frequency is set to provide the short-term memory time constant. The straight-through gain is set to provide the ratio of straight-through gain to lagged signal gain at frequencies beyond 5 Hz. The controller DC gain is provided by the summation of the lag path and straight-through path signals at the summing amplifier  $A_4$ . These signals vector  $A_4$  to provide the required steady state gain. As the input signal frequency increases, the lag path signal attenuates until the lag path signal is negligible, leaving only the straight-through path signal. The phase lag decreases and the gain attenuation ceases with the gain holding constant at the high frequency gain. The transfer function has the lag-lead specified for the controller. A major advantage of this active circuit over passive circuits is that the gain attenuation is avoided. High gain fluidic controllers with a minimum number of elements become practical.

### Test Results

Figure 37 shows the controller with valves in place of the orifices. Table 15 describes the procedure for setting these valves.

Null Bias--We applied 2000 psi supply pressure to the controller and measured several amplifier signals. For this test, there was zero rate input and blocked output. The signals could be nulled at any temperature by adjusting the supply pressure ratio between the VRS and the controller. However, the signals are sensitive to temperature.

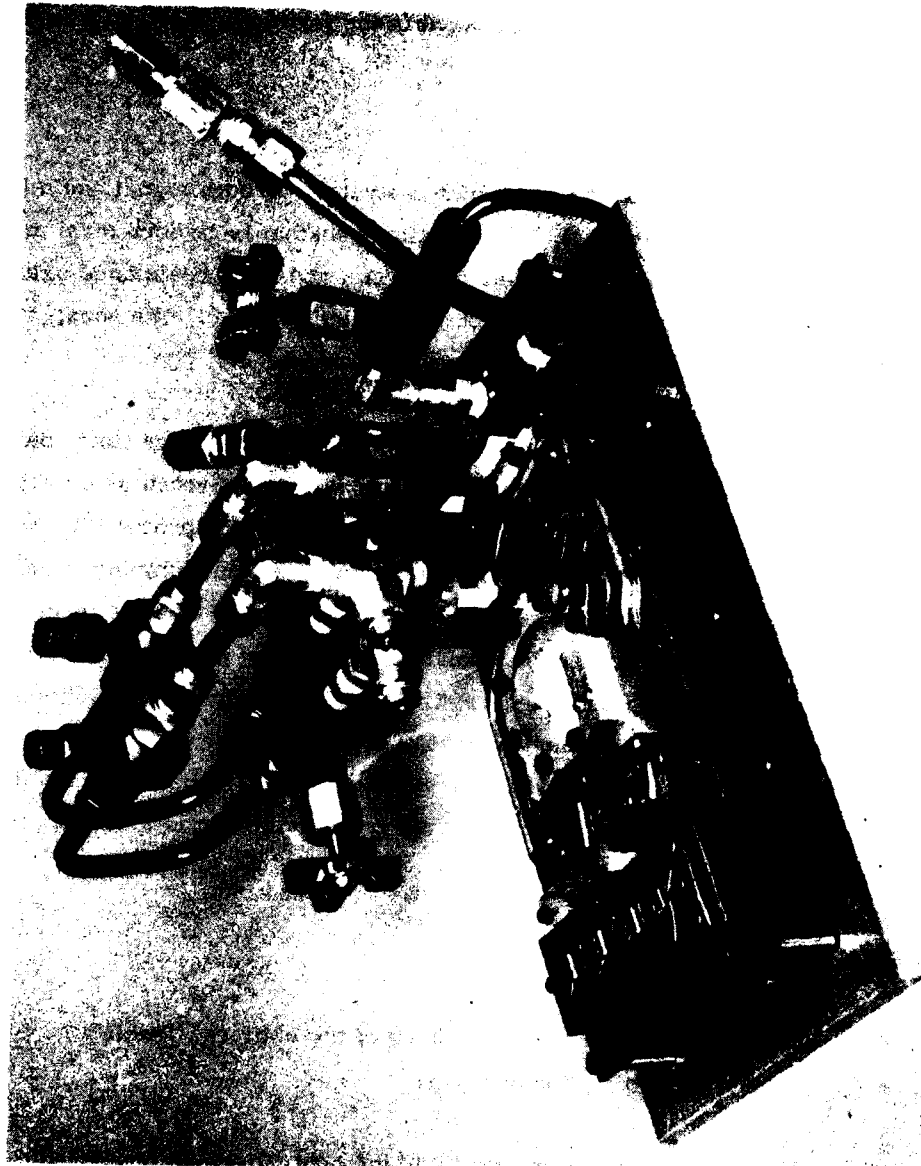


Figure 37. Controller Instrumented with Flow Meters and Valves for Impedance Matching

Table 15. Procedure for Selecting Controller Orifices

1. Select rate sensor supply orifices to obtain 1.1 gpm (4.24 cis) through the rate sensor.
2. Select the controller supply orifices to obtain an output static pressure equal to the cascade command port static pressure. This should be about 300 to 350 psi.
3. Select the controller return orifice to obtain a return pressure which is below the rate sensor output static pressure by 10 percent of the controller supply pressure. This should result in a  $\Delta P$  across the controller of about 250 psi and a flow rate through the controller of .85 gpm (3.27 cis).

The controller gain can be optimized by varying the return orifice and hence the ratio of VRS output static pressure to controller return pressure.

Figure 38 shows the pressure signals at three different amplifiers over a temperature range of 80 to 120°F with Mil 5606 oil. Mil 5606, at these temperatures, covers a viscosity range which can be obtained by modified Dow Corning # 510 silicone oil from -65°F to 160°F.

The attitude or lag amplifier output was very stable; it varied within  $\pm .01$  psi. This also indicates that the rate sensor preamp was also very stable. The rate amplifier stability is not within specifications since its output varied from  $-.5$  psi to  $+.9$  psi. This null bias is amplified two times at the output, producing approximately 40 psi of null shift.

The output null shift is 96 psi. This indicates that the summing amplifier or the output amplifier has additional null shift. This null shift can be reduced by improving the nozzle symmetry in the controller mold.

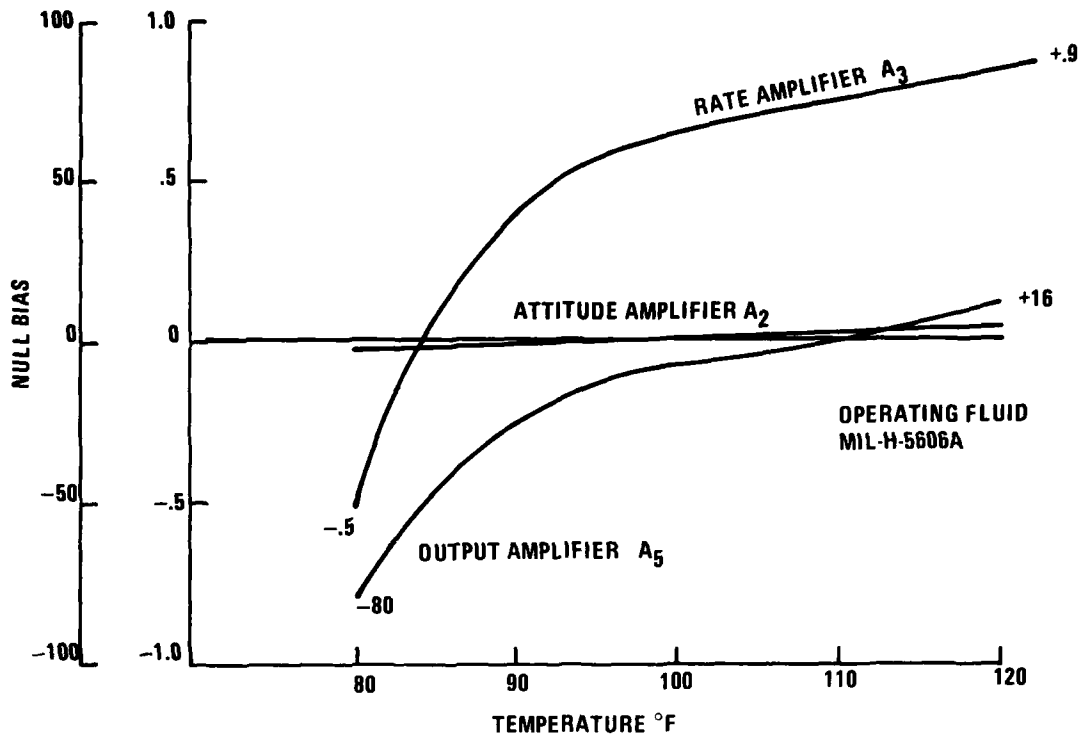


Figure 38. Controller Null Bias Stability

Gain and Frequency Response--A VRS/controller using the circuit shown on Figure 32 was tested. A production prototype design vortex rate sensor was used. This VRS is the same as that used in the Sikorsky UTTAS helicopter HYSAS and has been used successfully as a fluidic rate gyro on an experimental M60A1 battle tank gun/turret stabilization system.

The VRS used 1.10 gpm supply flow to meet the 0.009 sec transport time requirement. Figure 39 shows the gain factor test results. It was concluded that the prototype HYSAS rate sensor was satisfactory for the FTVC application.

The VRS/controller was also bench tested. The capacitor was mechanized with a rubber diaphragm. The capacitance is determined by the ratio of the effective area squared to the effective spring rate. Changing the diaphragm thickness allowed the capacitance to be varied. The hydrofluidic servos for this system have gain factors

NOTES:

1. SUPPLY FLOW ~1.1 gpm
2. FLUID: MIL-H-5606 AT 100°F
3. VRS PRESSURE DROP ~125 psi d
4. VRS LOAD WAS CONTROLLER INPUT AMPLIFIER
5. NOISE ~1 deg/sec (P-P)
6. THREE RESTRICTION WASHERS USED IN SECONDARY SINK
7. TRANSPORT TIME ~0.009 sec

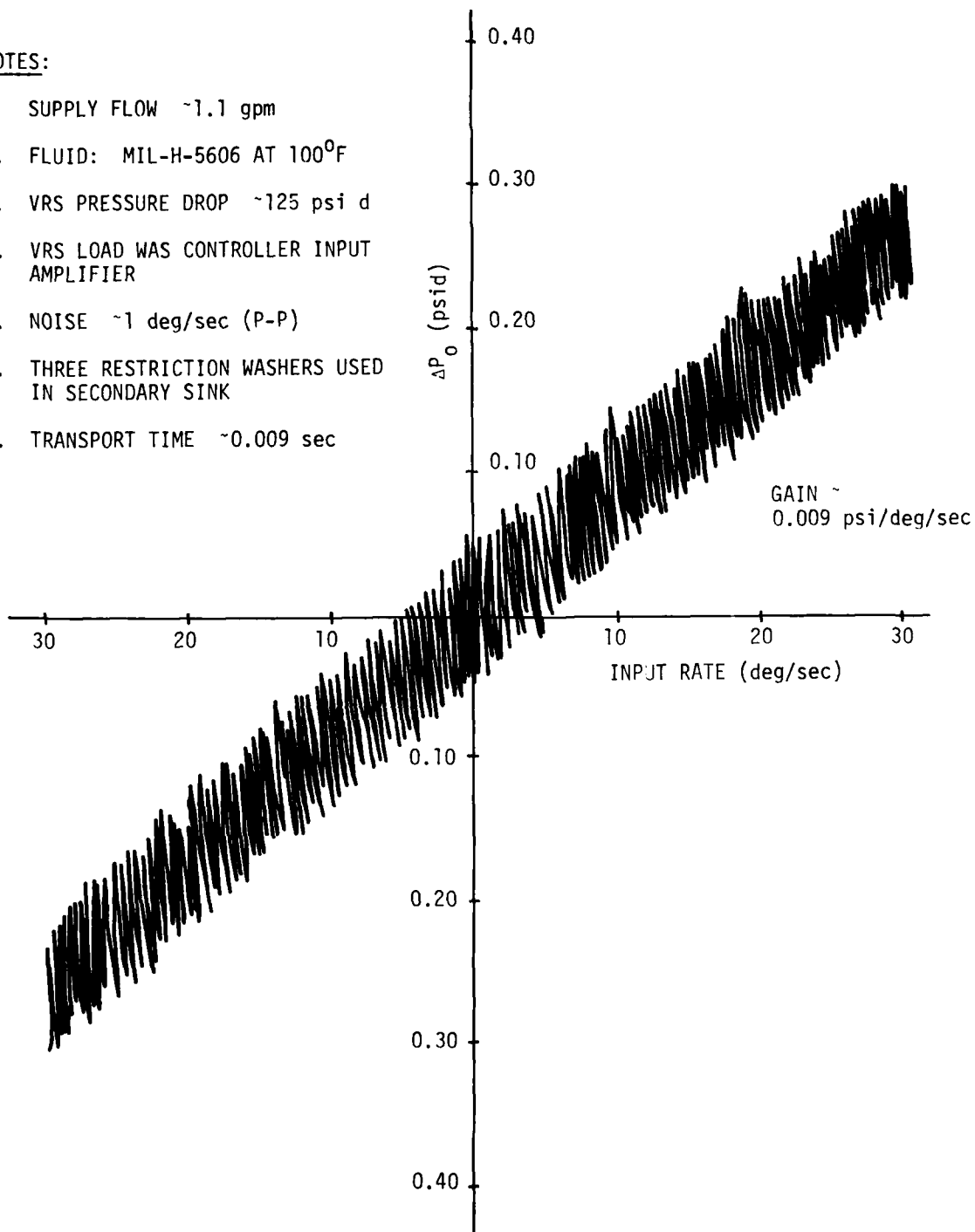


Figure 39. Vortex Rate Sensor Gain Factor (UTTAS Design)

of 0.30 to 0.50 deg/psid. The VRS/controller gain was computed from the FTVC requirements. The controller output was not loaded (no servo), so a loading factor was applied to obtain the VRS/controller gain on a dead-ended basis (pressure transducer load). VRS/controller gain must be variable between 2.0 and 6.0 psid/deg/sec to allow for variations in servo feedback gain.

Figure 40 shows the dynamic response results compared with the design requirement. The results show that the design goal response was met. It was observed that the capacitor had a threshold which allowed a straight-through rate signal in excess of that set by the straight-through signal path. This situation prevented matching exactly the apparent lead time constant. The VRS/controller gain was also greater than design value. This could have been reduced by the adjustable shunt resistor across the  $A_4$  amplifier output. The fluidic controller gain was calculated as 667 psi/psi. The controller circuit was satisfactory for FTVC application. Refinements to match design performance were not warranted at this time.

Transient Response--The breadboard VRS/controller transient response was measured. The  $\theta_{\text{bias}}$  (attitude) should be set at a value to cause the rocket motor to be driven to its null (mid-position) when the seat turned through the required angle. For example, if a 50 deg  $\theta_{\text{bias}}$  was required, the controller  $\theta_{\text{bias}}$  set would be adjusted so that the rocket motor would drive to its mid-position when the seat had turned through 50 deg.

A start-up transient test was made after setting the  $\theta_{\text{bias}}$  to -50 psid. The hydraulic pump was operating with the flow diverted to return by a solenoid valve. This kept the VRS/controller full of fluid. The solenoid valve was switched causing the flow to be fed to the VRS/controller. Ten feet of hydraulic lines were between the pump and the VRS/controller.

Figure 41 shows the transient start-up with no angular rate applied. It took 0.150 sec for the output to attain the -50 psid bias. The bias overshoot the -50 psid by about 10 psid and then decayed back to -50 psid. Start-up offsets ahead of the short-term memory are minimal. The bulk of the 0.150 sec time to attain set  $\theta_{\text{bias}}$  signal output was due to the line length between the hydraulic source and the controller. A close coupled source will be used in the future.

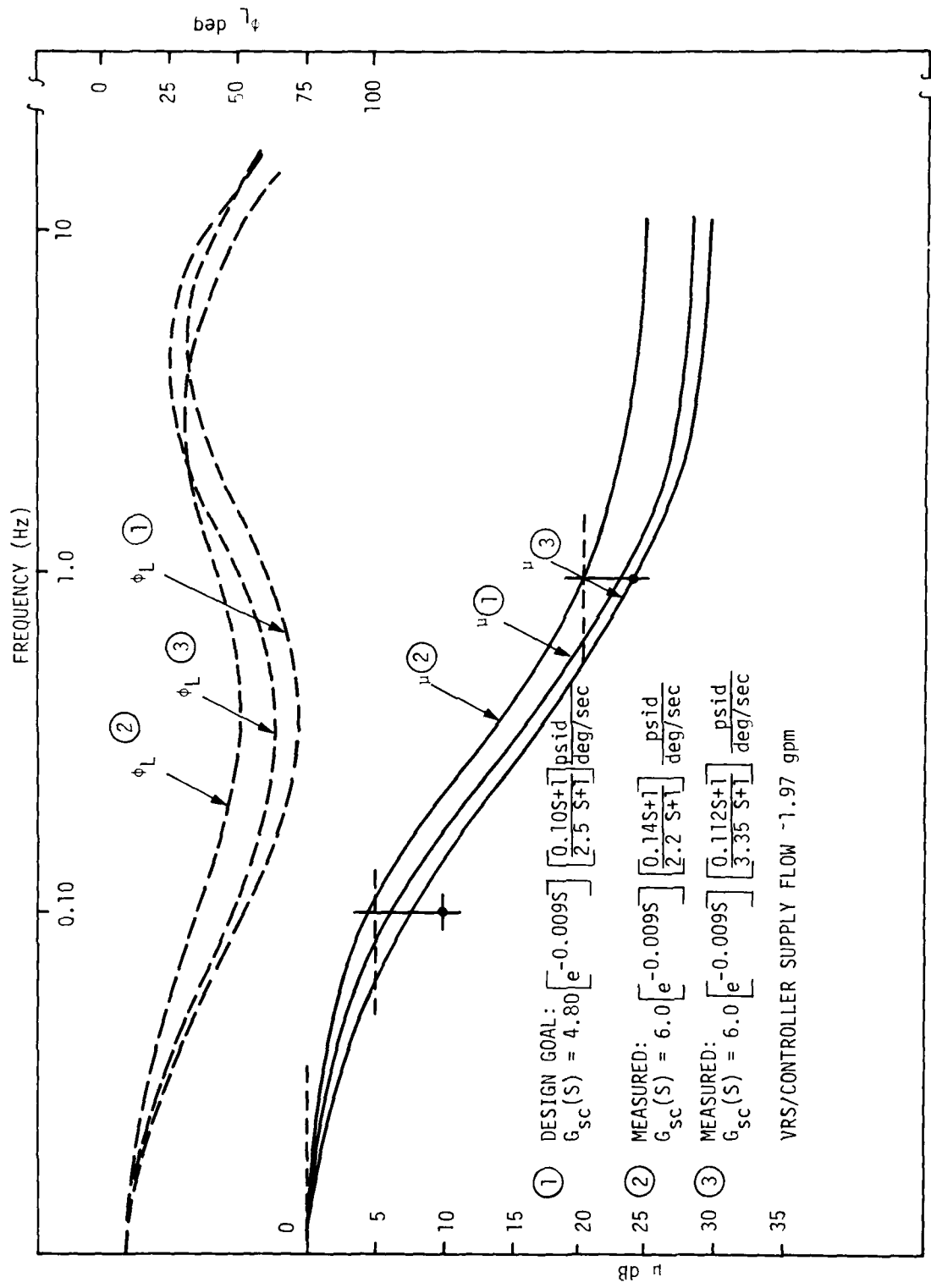


Figure 40. Dynamic Response--Breadboard VRS/Controller

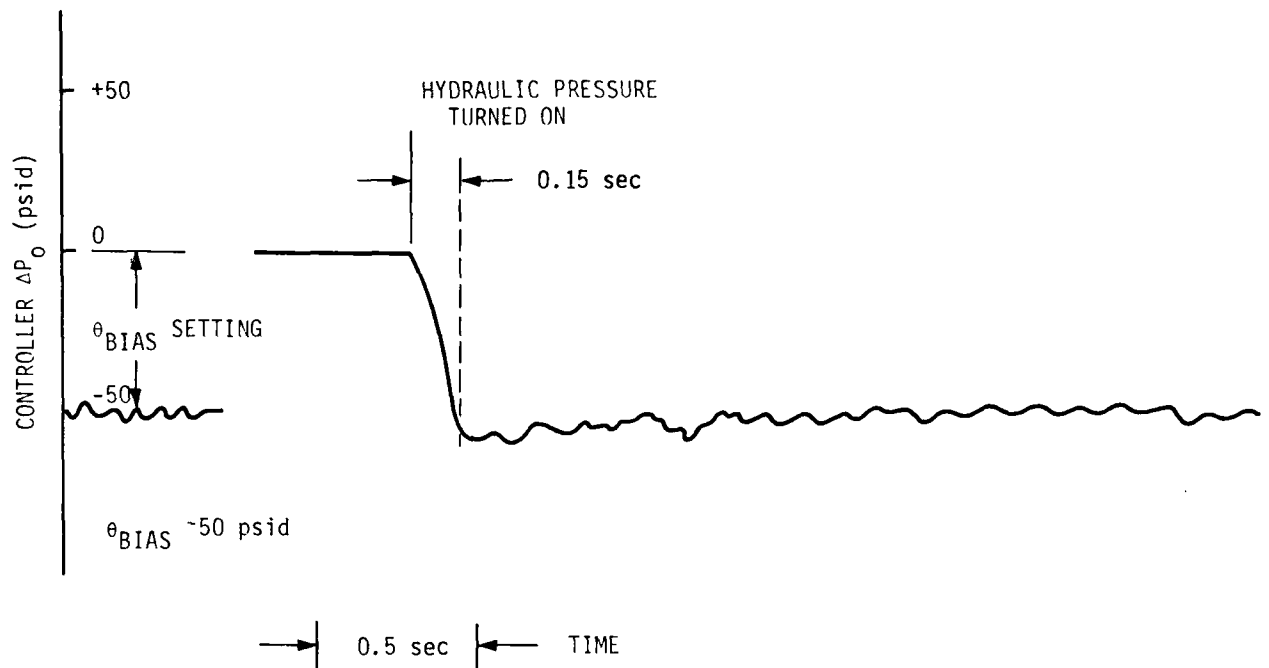


Figure 41. VRS/Controller Start-Up--Zero Rate Applied

A second transient test was made. The hydraulic pressure was turned on and a 100 deg/sec step input rate was applied by the rate table. The rate table was switched on at the time the  $\theta_{bias}$  output reached peak value. These results are shown in Figure 42. The same 0.150 sec signal buildup time was seen. At 0.56 sec after the rate was applied, the memory drove the controller output to null. The table had turned through a 56 deg angle at the time the controller output reached null. The rate input was left on for 0.50 sec and the table turned through 50 deg. The preset  $\theta_{bias}$  was equivalent to 50 deg. The -50 psid  $\theta_{bias}$  set was worth 56 deg. After crossing through null, 35 psid was worth 50 deg. This difference in integration is due to threshold effects in the capacitor.

A third transient test was made. The 100 deg/sec step input rate was applied before the pressure was turned on. These results are shown in Figure 43. Again, it took 0.150 sec for the controller output signal to reach peak value. The peak output of the controller was less than the steady state set  $\theta_{bias}$  output. The fluidics were working as soon as supply pressure was applied. The memory was supplying a rate integrating

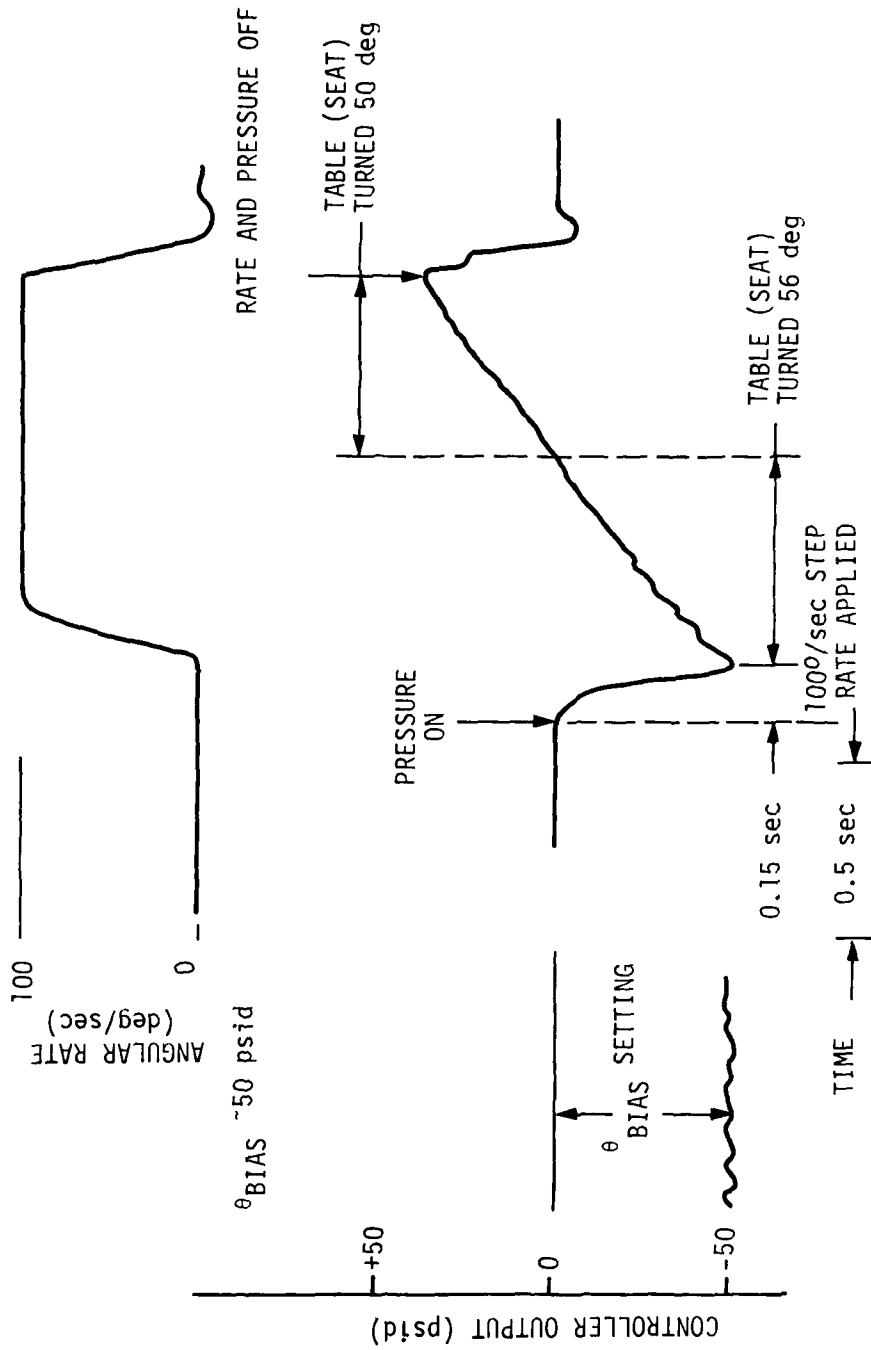


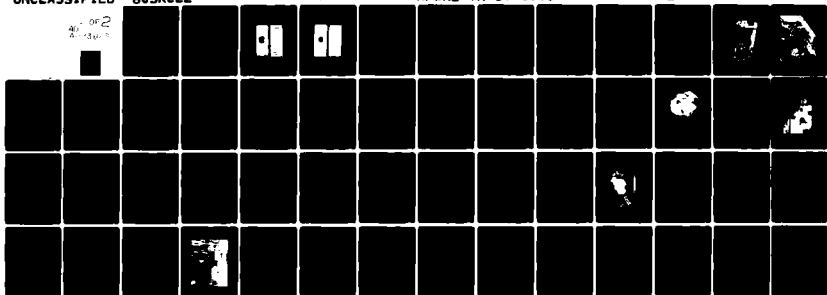
Figure 42. Start-Up Transient Test Controller Turned On Before Rate Input

AD-A093 888

HONEYWELL SYSTEMS AND RESEARCH CENTER MINNEAPOLIS MN F/G 1/3  
TWO-AXIS, FLUIDICALLY CONTROLLED THRUST VECTOR CONTROL SYSTEM F--ETC(U)  
JUL 80 R B BEALE, R V BURTON, N E MILLER F33615-76-C-3070  
80SRC22 AFWAL-TR-80-3080 NL

UNCLASSIFIED

OF 2  
2-84



END

DATE

FILMED

2-84

DTIC

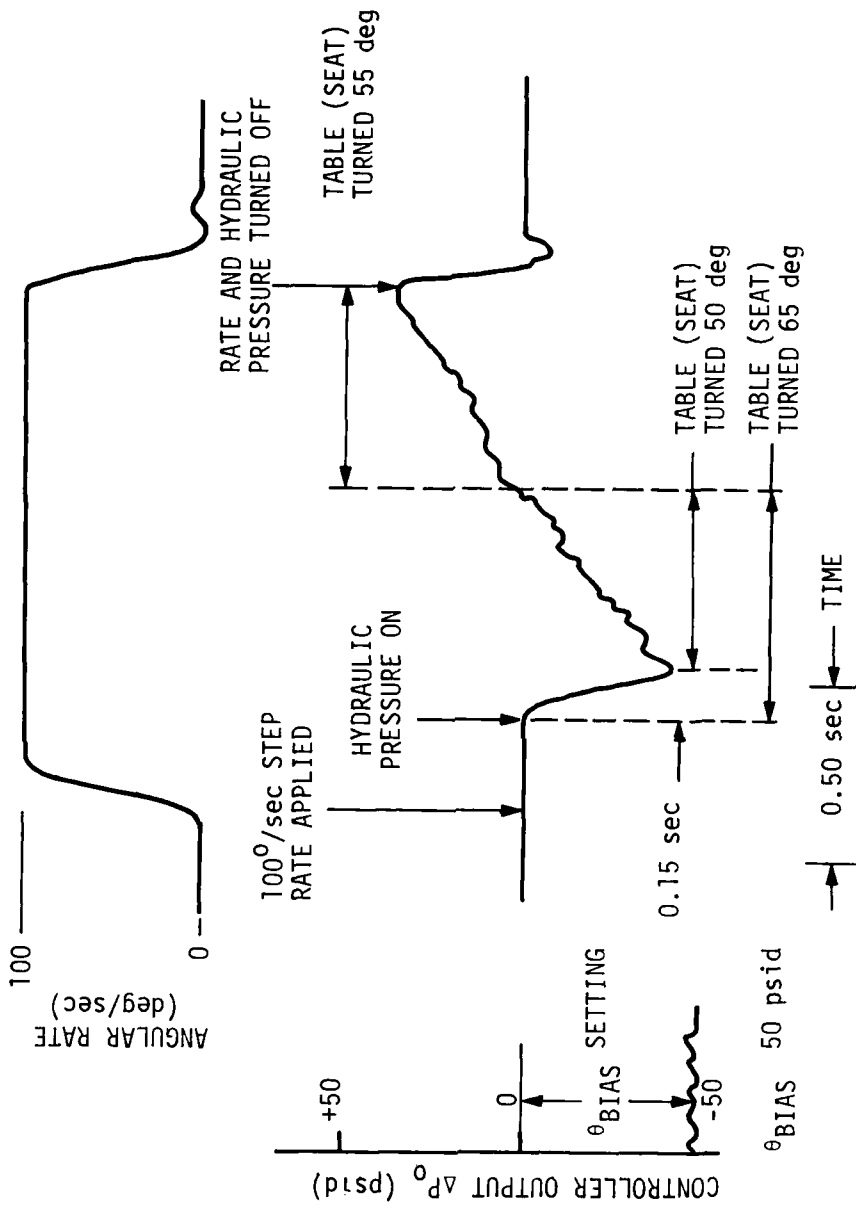


Figure 43. Start-Up Transient Test Controller Turned On After Rate Input

output as the VRS/controller supply was building up. The peak output pressure was -40 psid as compared to a -50 psid for steady state conditions. From the time of pressurization, the seat turned 65 deg before the controller output was driven to null. The controller output attained a 35 psid output after the seat turned an additional 55 deg. The  $\theta_{\text{bias}}$  set was worth 65 deg of seat travel instead of the intended 50 deg. The time to pressurize the VRS/controller is the integration error. The use of a close coupled power source will reduce pressurization time and improve the memory integrating accuracy.

Conclusions drawn from the breadboard tests are as follows:

- The selected VRS/controller mechanization meets the performance requirements for the FTVC application.
- $\theta_{\text{bias}}$  was demonstrated. In the future the  $\theta_{\text{bias}}$  setting will be based on the rocket nozzle position instead of fluidic controller output signal.
- The five amplifier configuration meets the DC gain requirement of the controller.
- Transient start-up does not appear to present problems. Test results were considered very satisfactory. VRS/controller tests with a close coupled hydraulic power source are necessary for measuring start-up time.

#### Fabrication

Figures 44 and 45 show the brass mold and wax form of the controller. The most critical process in fabrication of the controller is machining the mold. The symmetry of the amplifier nozzles with respect to the control ports and splitter are critical to amplifier null bias. Electroforming is a low-cost production process once the mold is perfected.

A steel base plate shown in Figures 44 and 45 is clamped between the upper and lower molds. The two sides are injected simultaneously with a conductive wax. Nickel is electroplated over the wax, and the wax is cleaned out.

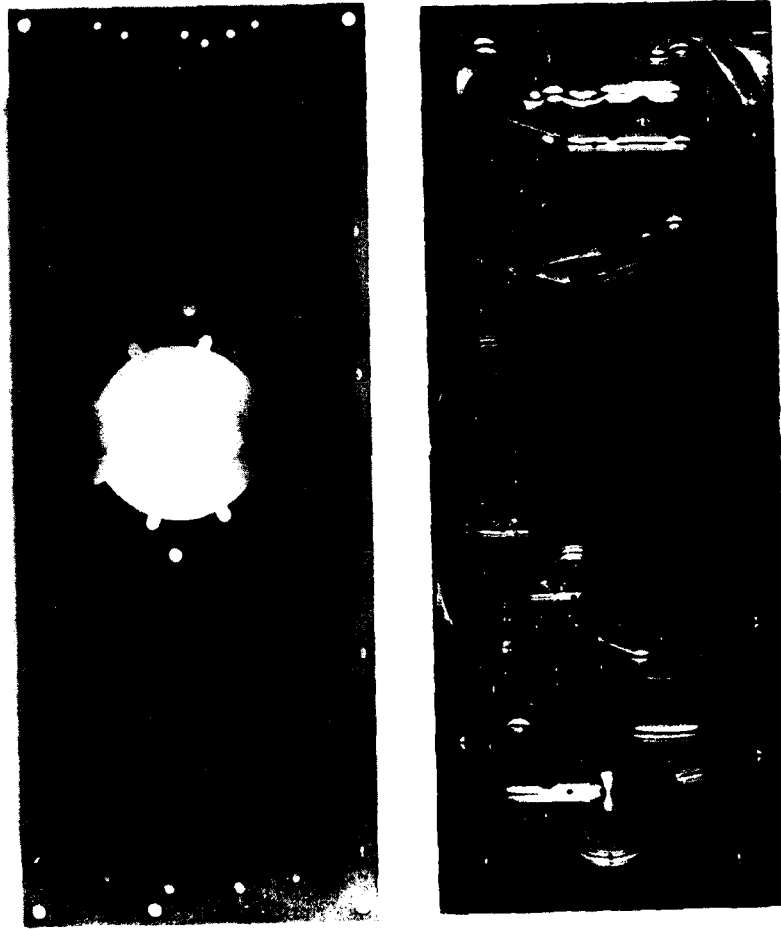


Figure 44. Mold and Wax Form of the Under Side of the Controller Circuit

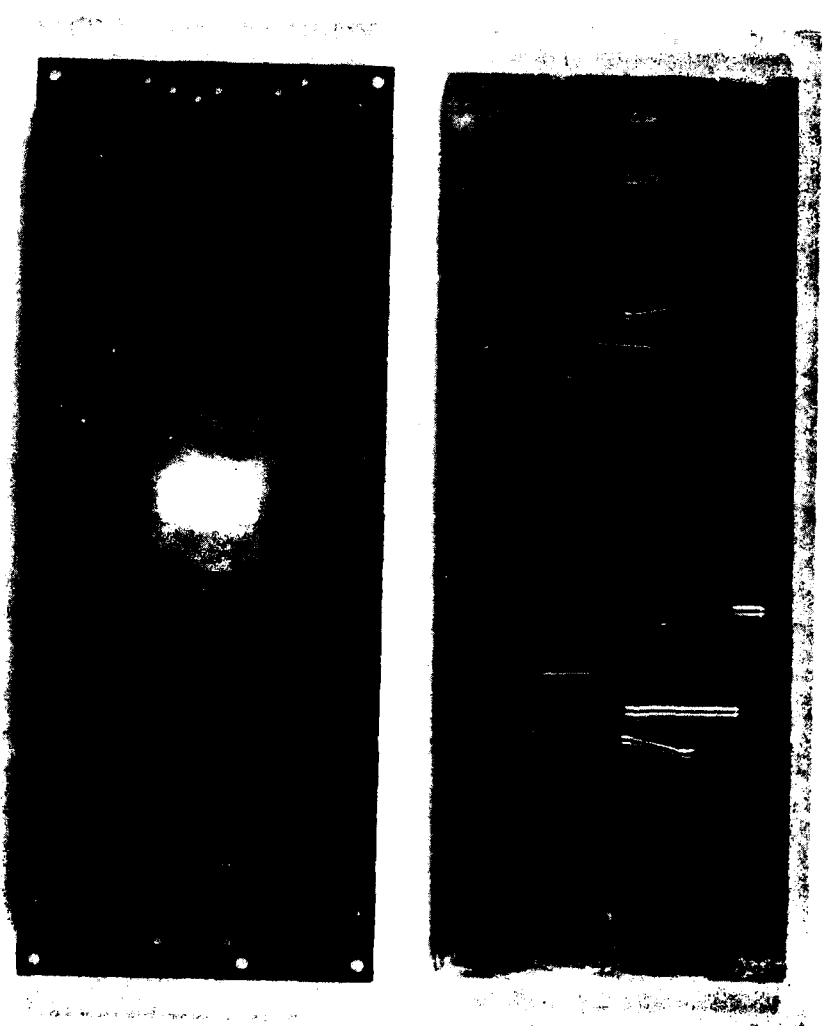


Figure 45. Mold and Wax Form of the Upper Side of the Controller Circuit

## NOZZLE SERVO SYSTEM

### Description

The hydrofluidic servovalve concept was selected for the nozzle positioning application<sup>6</sup> as a low-cost, highly reliable alternative to a mechanical servovalve.

Figure 46 shows a block diagram of the servo concept. The servo loop consists of a proportional amplifier, actuator, and position feedback transducer. The first stage of the amplifier sums the input and feedback signals by using stream deflection. All amplifiers are vented to the exhaust.

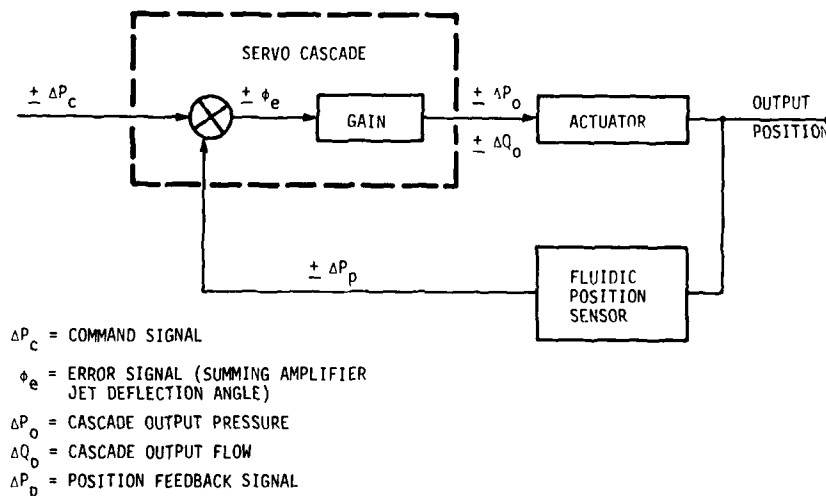


Figure 46. Block Diagram, Basic Hydrofluidic Servo

<sup>6</sup>R. V. Burton and R. B. Beale, "Development of a Hydrofluidic Vernier Rocket Control System for Ejection Seat Stabilization," NASC N00019-C-0374, Honeywell, Inc., Minneapolis, Minnesota, December 1976.

The key component of the servo loop is the servovalve. It provides signal amplification, actuator driving, and actuator position feedback. It has no moving parts. The servovalve performs the same functions as the servoamplifier and servovalve in a conventional electrohydraulic servoactuator.

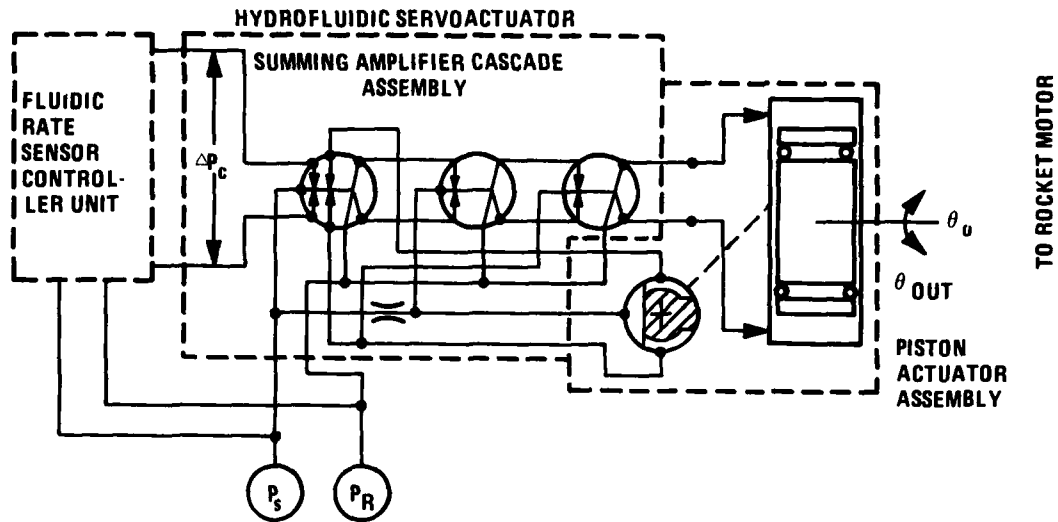
The input signal is a differential pressure supplied by a fluidic controller unit. The actuator position feedback signal is a differential pressure supplied by a flow divider type fluidic sensor. The sensor produces an output differential pressure proportional to the actuator position. The error signal which drives the actuator is the summing amplifier deflection angle. The deflection angle is produced by the summation of command signal and feedback signal thrust vectors acting on the amplifier power jet.

Figure 46 shows that this concept has eliminated the numerous moving parts common to conventional servos. It has replaced them with dynamic pressure functions. The actuator and position feedback sensor are the only moving parts in the servo loop.

Figure 47 shows a schematic of the servoactuator selected for the rocket nozzle. The servoactuator consists of the nozzle assembly with attached position feedback sensor and the servocascade. The actuator is a piston with a crank arm. The hydrofluidic servoactuator has a building block or "erector set" configuration. This demonstrates the versatility of the hydrofluidic servoactuator concept.

The operation of the servoactuator is described in Figure 47. When fluid is applied to the supply port (Ps), power and control jet flows are established in the servocascade. Power jet flow not used by the fluid amplifier receiver ports is vented to a common return line. Servo supply flow is the same for driving the actuator or holding actuator position. The hydrofluidic servo requires a continuous power flow for operation. The servo is inoperative when the power flow is cut off.

An input signal is supplied by the fluidic controller to the servocascade command ports. This signal produces an error signal in the form of power jet deflection angles. The power stage of the cascade delivers a flow rate to the actuator to produce an actuator velocity proportional to the error signal. Actuator motion causes the fluidic position sensor to produce a differential pressure signal. The feedback signal generates control thrust in the summing stage. This reduces the cascade power jet deflection angles to zero (null).



**NOTES:**

1.  $P_S = 2000$  psi
2.  $P_R =$  ATMOSPHERES
3.  $\theta_o$  IS PROPORTIONAL TO  $\Delta P_C$

**ROCKET NOZZLE ASSEMBLY IS THIOKOL, THIOVEC<sup>R</sup> DESIGN WITH HI FEEDBACK TRANSDUCER**

Figure 47. Schematic of Nozzle Hydrofluidic Servoactuator

The power stage output flow is reduced to zero, and equal static pressures are developed at the actuator input ports. The actuator assumes the position commanded by the input signal.

When the actuator is subjected to an external load, the actuator deflection causes the position sensor to generate an output signal. This signal causes the servocascade to generate an output differential pressure to resist the load change. The amount of actuator position change for a given load change is a function of the feedback loop gain. The resulting servo stiffness or torque gradient is a measure of servo positional accuracy.

**Test Results**

The hydrofluidic servoactuator concept has the performance potential for this application. One was bench tested at 2000 psi supply pressure. The servoactuator consists of a servocascade and an actuator assembly. The actuator in preliminary tests had

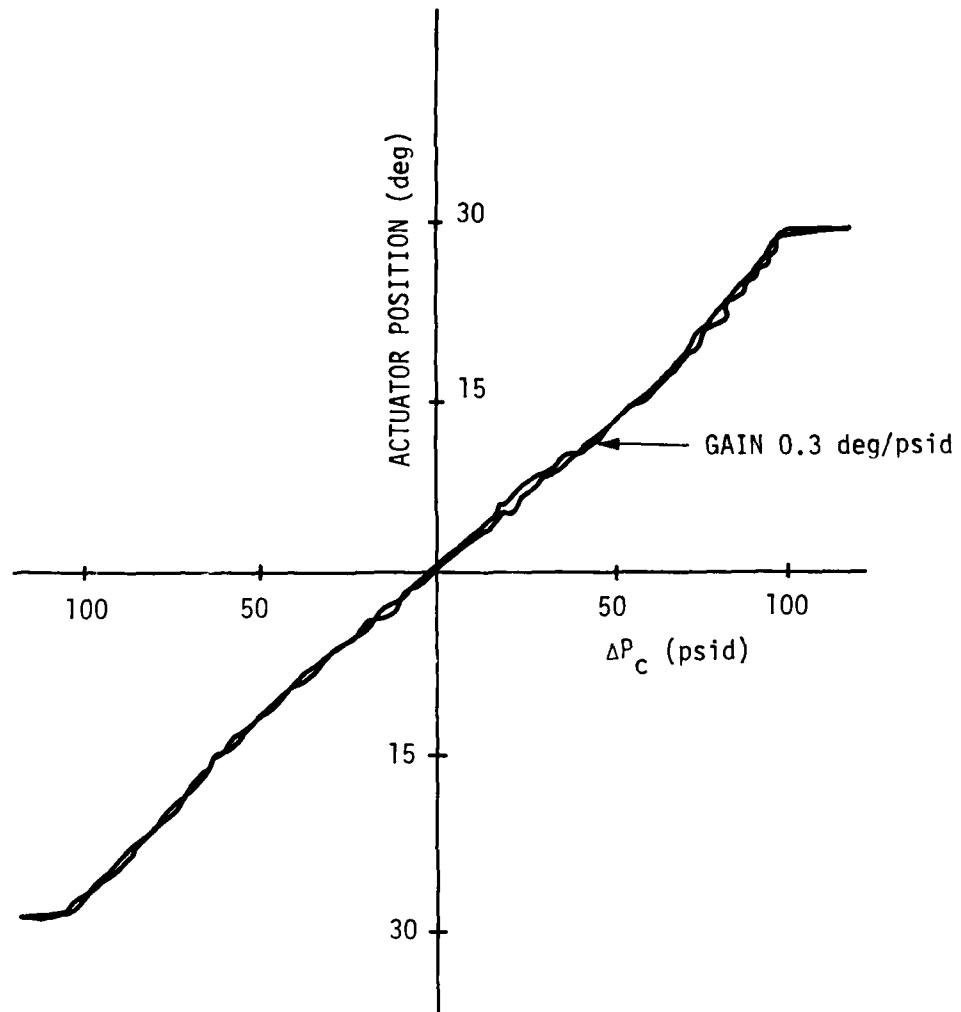
a balanced vane design and had the fluidic position feedback sensor built into the actuator output shaft. The actuator volumetric displacement was  $0.80 \text{ in}^3/\text{rad}$ .

Dynamic Response--The load in preliminary tests consisted of  $0.00684 \text{ in-lb sec}^2$  inertia and 17 in-lb of friction. Figure 48 shows the scale factor and Figure 49 shows the servoactuator dynamic response.

The test data show that the servoactuator operates well at a 2000 psi supply pressure and has sufficient performance for the rocket nozzle positioning application. To meet the  $700 \text{ deg/sec}$  slew rate, the actuator displacement was reduced to  $0.030 \text{ in}^3/\text{rad}$  in the final configuration. The stall torque was reduced from 640 to 302 in-lb. The actuator torque measured at the  $700 \text{ deg/sec}$  slew rate was initially 60 in-lb. Since the torque requirement is 80 in-lb, a fourth stage was added to the cascade which resulted in a torque capability of 240 in-lb at  $700 \text{ deg/sec}$  in the final configuration.

Scale Factor--The final configuration is shown in Figures 50 and 51. Table 16 describes impedance matching conditions of the servoactuator. The fluidic position feedback sensor gain is an important parameter in determining servo loop gain. A number of tests were conducted on the actuator where the servo supply pressure and ambient pressure levels at the command ports varied. The effect of command signal ambient pressure level on servo feedback gain, servo scale factor, and servo dynamic response was determined. The servo command pressure ambient level will be determined by the scaling of the controller output stage and the selected supply pressure. Servo scale factor increased as the command pressure ambient level was decreased. But the servo dynamic response was essentially unaffected. An increase in servo scale factor is due to a decrease in position feedback gain. Normally one would expect a decrease in servo dynamic response. But the jet deflection sensitivity of the jet summing stage increases. This effect provides an increase in forward loop gain which offsets the decrease in feedback gain.

Figure 52 shows a plot of position feedback sensor gain for various servo supply pressures and command port ambient pressure levels. This effect is more pronounced at the higher servo supply pressures (greater than 500 psi). These data will be extremely useful for scaling the hydrofluidic servoactuator loop when using the "building block" configuration shown in Figure 47.



NOTES:

1. MIL-H-5606 FLUID AT 100° TO 140°F
2.  $P_s = 2000$  psi
3.  $Q_s$  (SUPPLY FLOW RATE) ~3.96 gpm
4. SLEW RATE ~330 deg/sec
5. STALL TORQUE ~640 in-lb
6. INPUT SIGNAL SUPPLIED BY 24110029-006  
COMMAND VALVE ASSEMBLY

COMMAND SIGNAL AMBIENT PRESSURE 32%  $P_s$

Figure 48. Scale Factor--ACH104A1022 Hydrofluidic Servoactuator

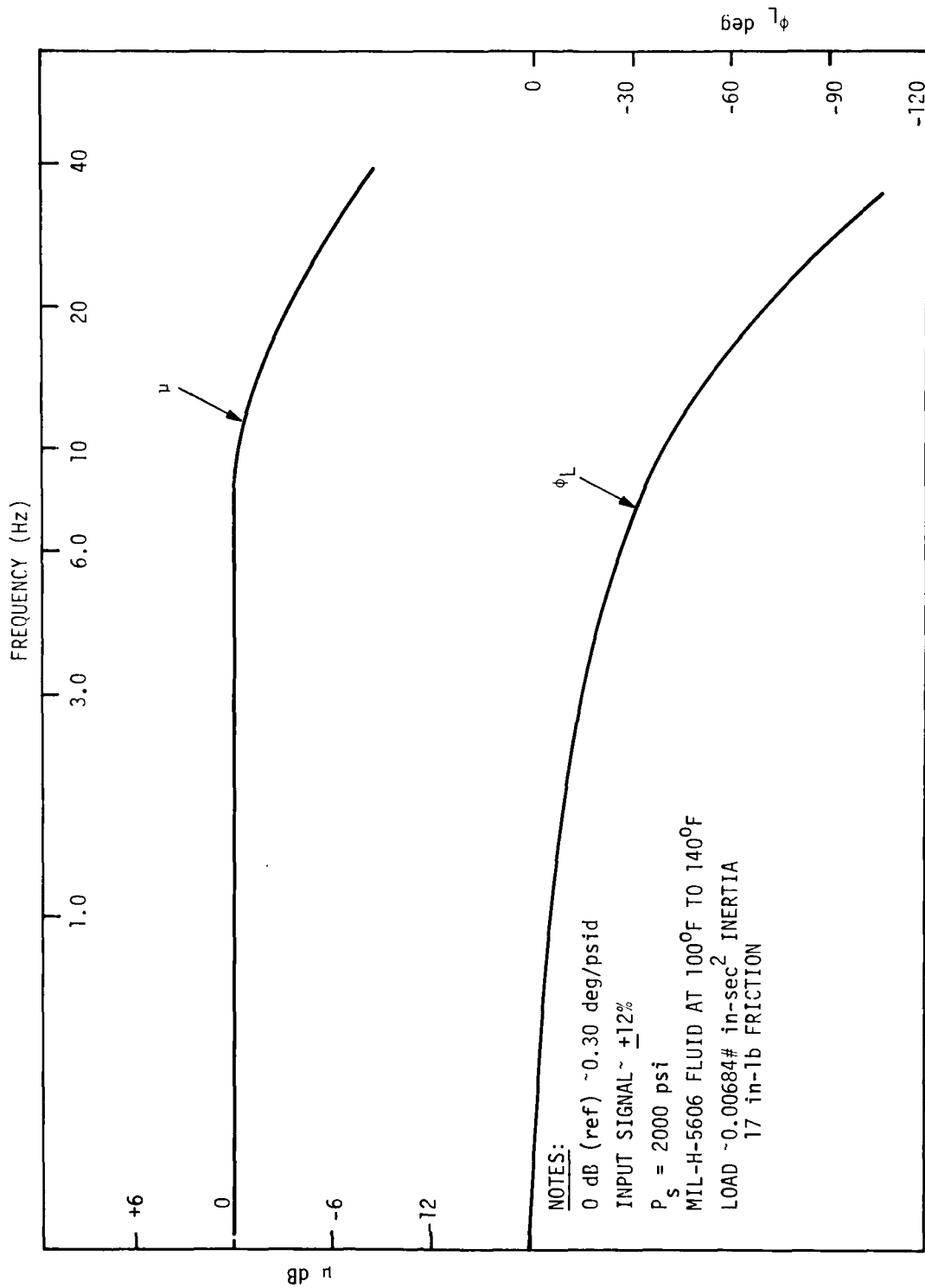


Figure 49. Dynamic Response--ACH104A Hydrofluidic Servoactuator

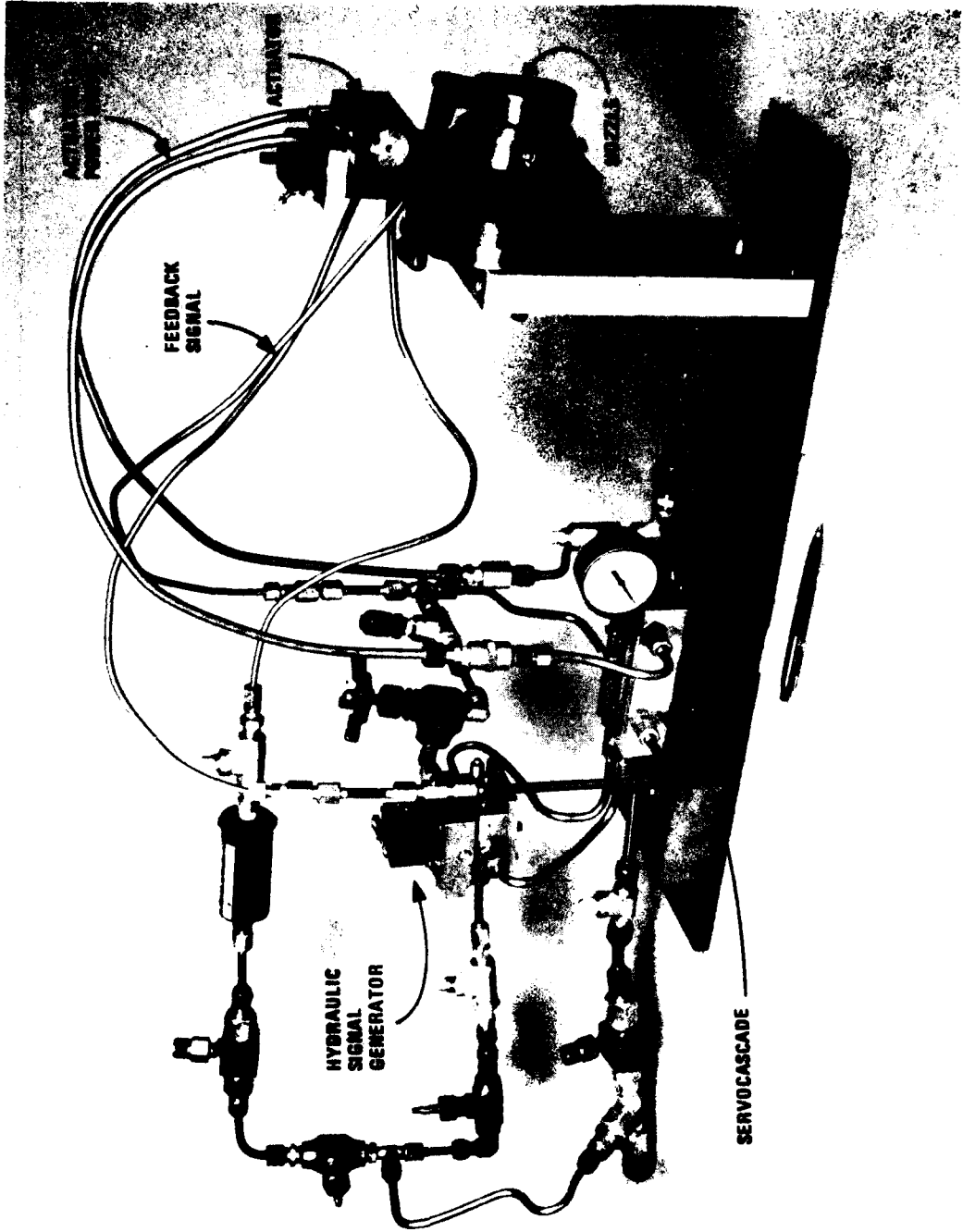


Figure 50. Nozzle Servo Test Apparatus

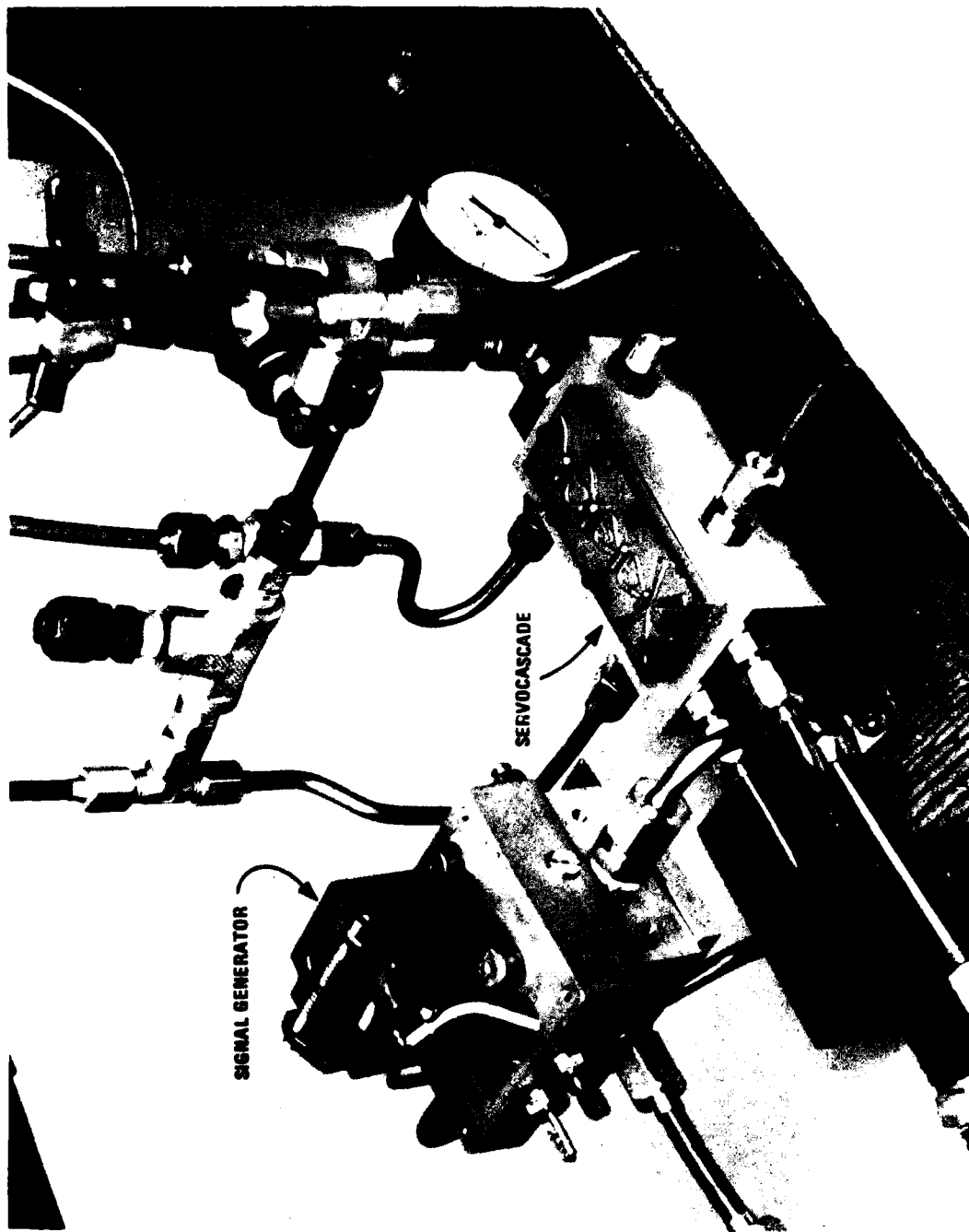


Figure 51. Servocascade Test Apparatus

Table 16. Nozzle Servo Adjustments

1. Set feedback transducer supply pressure to obtain a mass flow ratio of one or less at the cascade amplifier. This should correspond to a command port pressure level of 300-350 psi.
  - a. Mass ratio too high--No control, stiffness or sensitivity to command, very jittery
  - b. Mass ratio too low--High scale factor, very sensitive to command, little stiffness
2. Set feedback shunt to obtain transducer feedback gain of 126 psid/rad or loop scale factor of .5 deg/psid.

NOTE: Mass ratio--control flow rate/supply flow rate  
Scale factor--rocket nozzle deflection/input  $\Delta P$

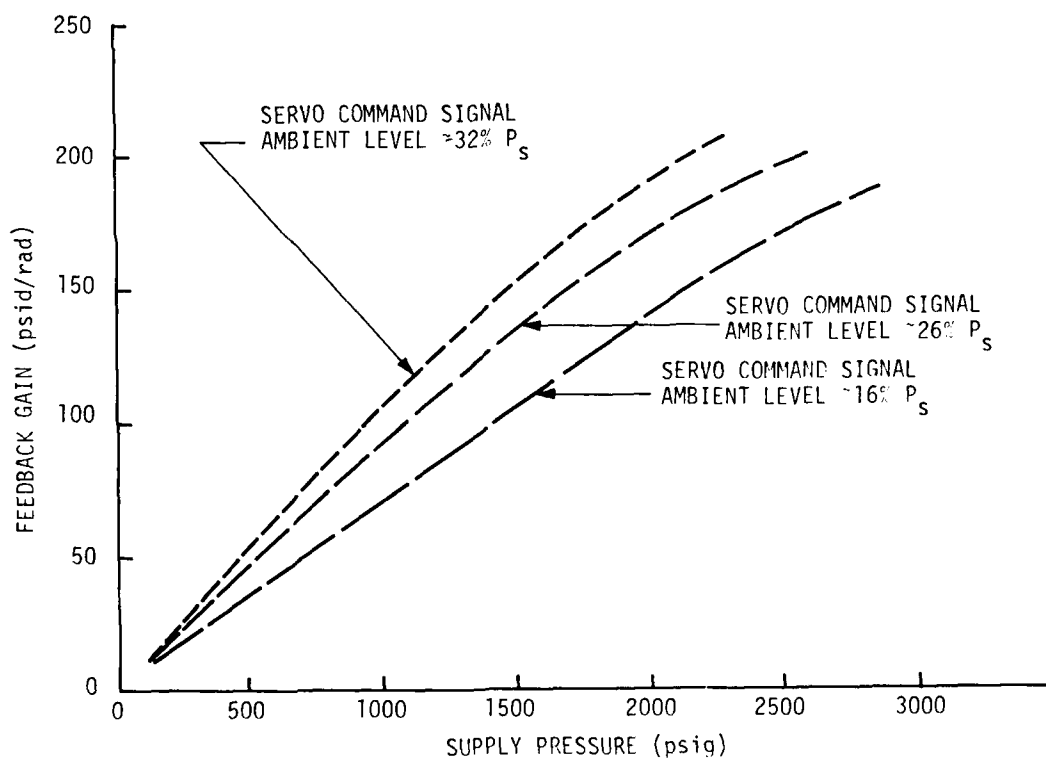


Figure 52. ACH 104 Servo Feedback Transducer Characteristic

Servo Valve Power--Cascade bench tests were conducted to provide information on P-Q envelope curves, pressure gain, and flow gain for 1000 to 2000 psi supply pressure. Figure 53 shows the typical P-Q envelope for the three-stage power amplifier.

Figure 54 shows the measured P-Q envelope for the servocascade at 1500 psi supply pressure. The measured curve fits the composite data curve shown in Figure 53. We can use the composite P-Q envelope curve to predict power stage fluid amplifier sizes for various operating design requirements.

Cascade pressure gain was measured at 1500 psi supply and is shown in Figure 55. Cascade flow gain was determined by calculation from the open-loop response, obtained from the Nickols Chart, using the closed-loop servo response shown in Figure 49. The pressure gain and flow gain data obtained from the breadboard tests were compared with prior data on high pressure cascades. Our techniques for predicting pressure and flow gains for high pressure servocascades of various sizes are valid for design purposes.

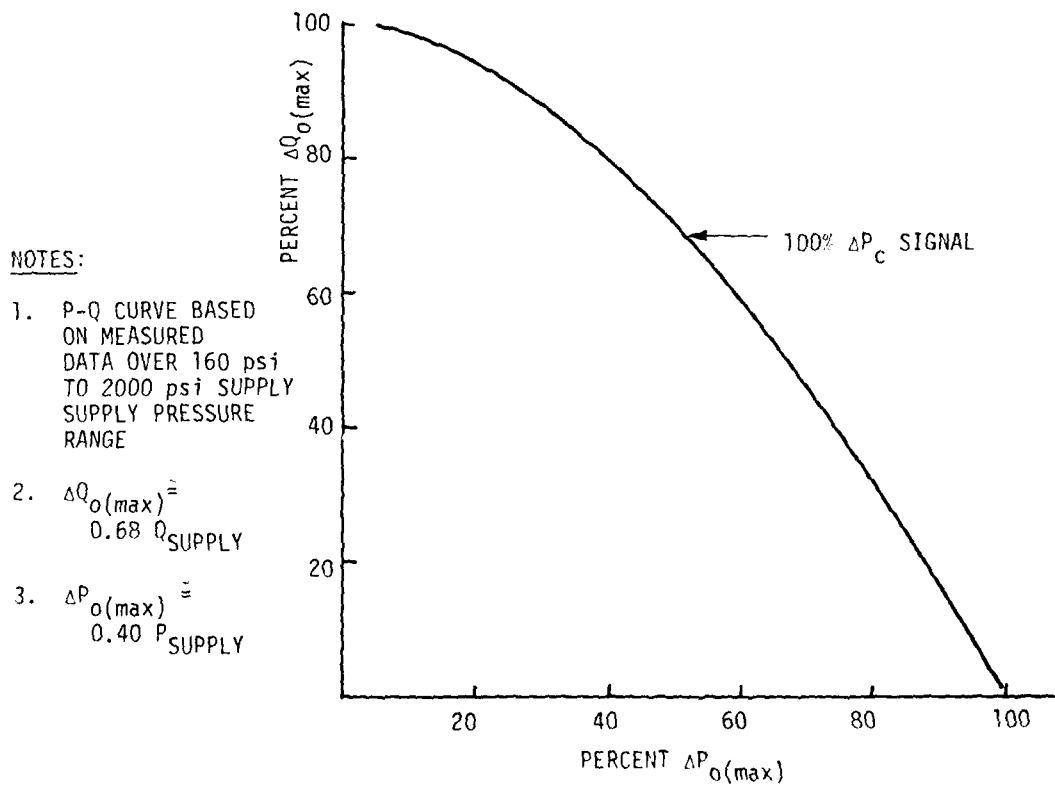


Figure 53. Typical P-Q Envelope for a Fluid Power Amplifier (High Pressure Data)

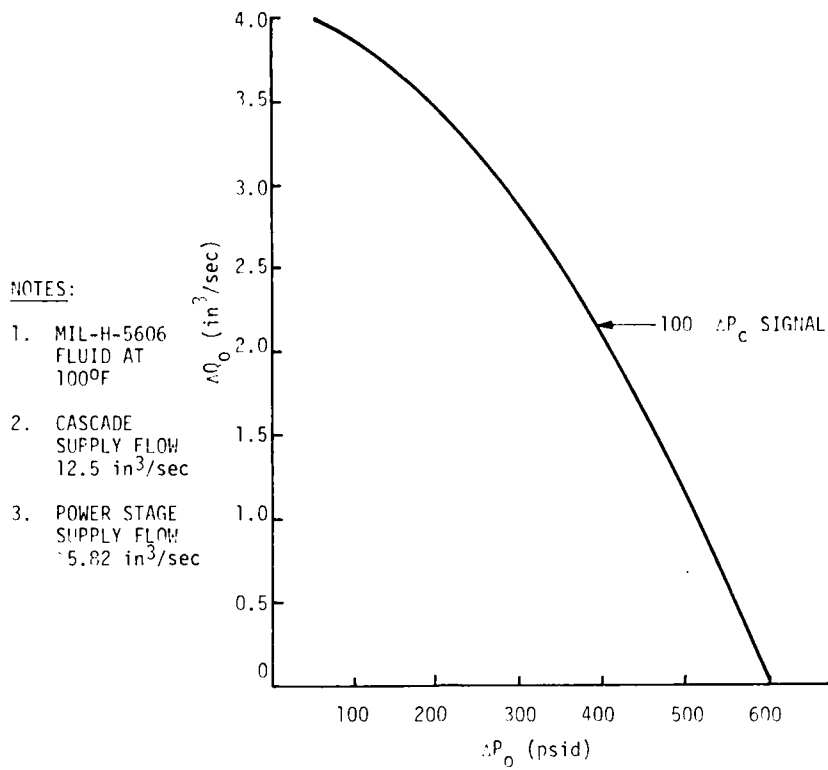


Figure 54. P-Q Envelope for 24110024-00 Three-Stage Servocascade at 1500 psi Supply Pressure

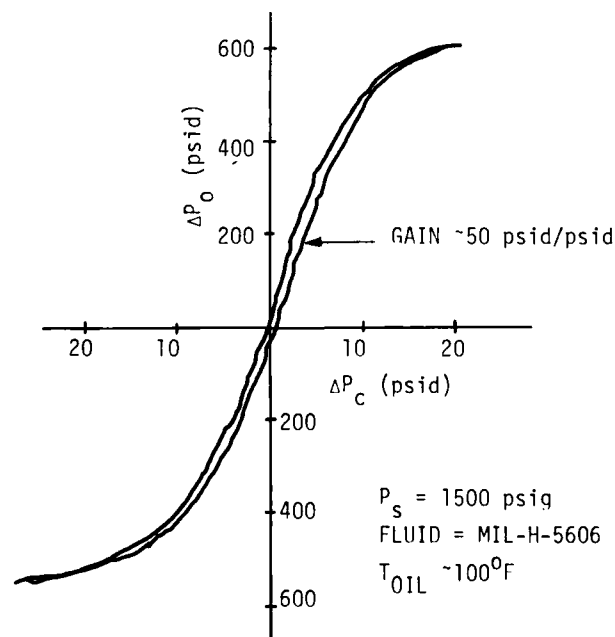


Figure 55. Blocked Actuator Port Pressure Gain--24110024-001 Servocascade

## Design Analysis

The servosystem is shown in Figure 47. The key element is a servocascade with sufficient output to drive the actuator load. The servocascade, actuator, and fluidic position feedback sensor also must be designed. The resulting servo loop characteristics must be adequate to meet the dynamic response requirements.

Servovalve Power--The servoactuator torque requirements are specified at 700 deg/sec slew rate. The servocascade must supply an output flow rate of 3.7 in<sup>3</sup>/sec at a differential pressure of 266 psid. The servocascade power amplifier stage is then based on this requirement. Using the power amplifier P-Q curve (Figure 53), the power amplifier size and output characteristics were predicted. The prediction is shown in Figure 56. A power amplifier design with a power nozzle width (Wp) of 0.042 in and an aspect ratio of 1.25 was fabricated. The details of the amplifier design are not shown.

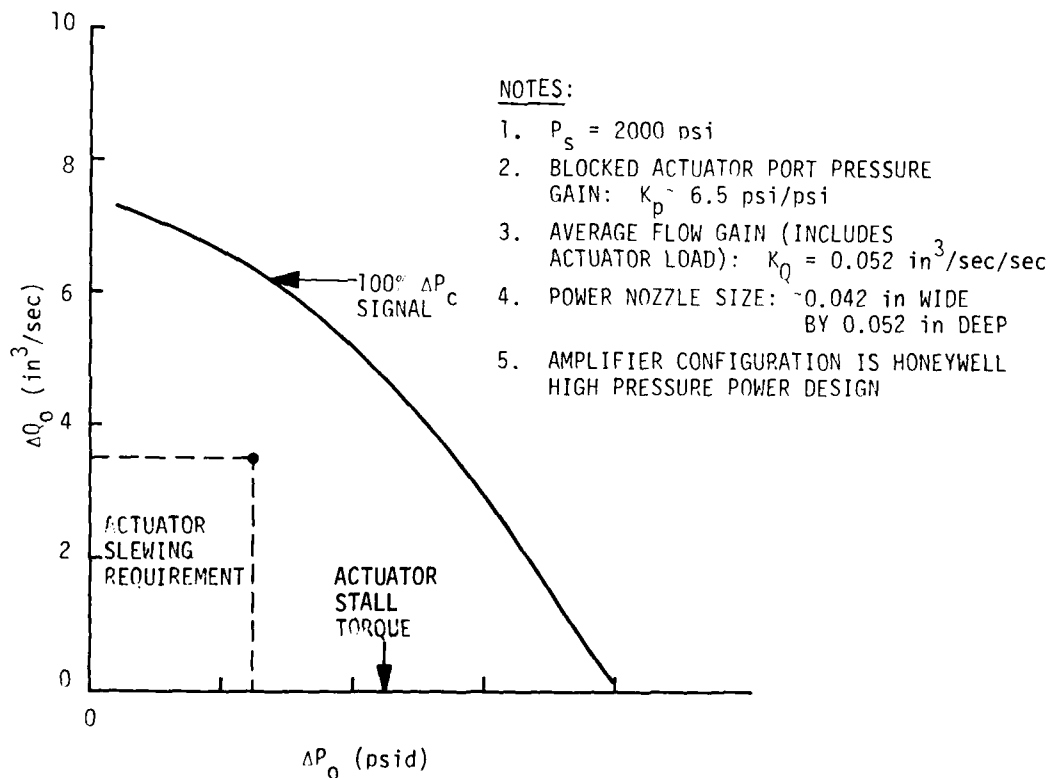


Figure 56. P-Q Envelope for Four-Stage Actuator Power Fluid Amplifier

Servo loop gain affects the servoactuator dynamic response. It is based on the actuator volumetric displacement and feedback gain. A servoactuator scale factor must be compatible with the inertial rate sensor/fluidic controller scale factor. A four-stage servocascade with the 0.042 in x 0.052 in power nozzle added is more than adequate. Pressure gain and flow gain estimates were generated for this design and are shown in Figures 57 and 58.

Servocascade supply flow requirements were calculated for the 2000 psi supply pressure and are as follows:

- First stage (summing amplifier)    ~ 2.36 in<sup>3</sup>/sec
- Second stage                                ~ 4.41
- Third stage                                    ~ 6.72
- Fourth stage (actuator driver)    ~  $\frac{10.74}{24.23}$  in<sup>3</sup>/sec

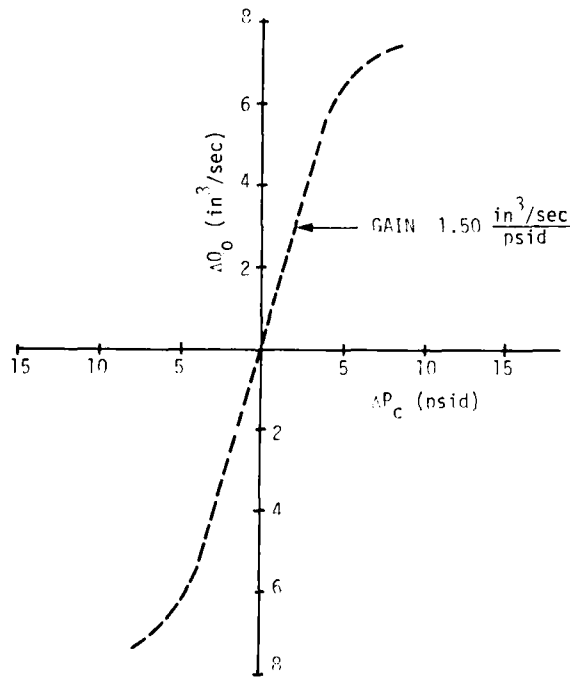


Figure 57. No-Load Flow Gain, Four-Stage Servocascade at 2000 psi Supply Pressure

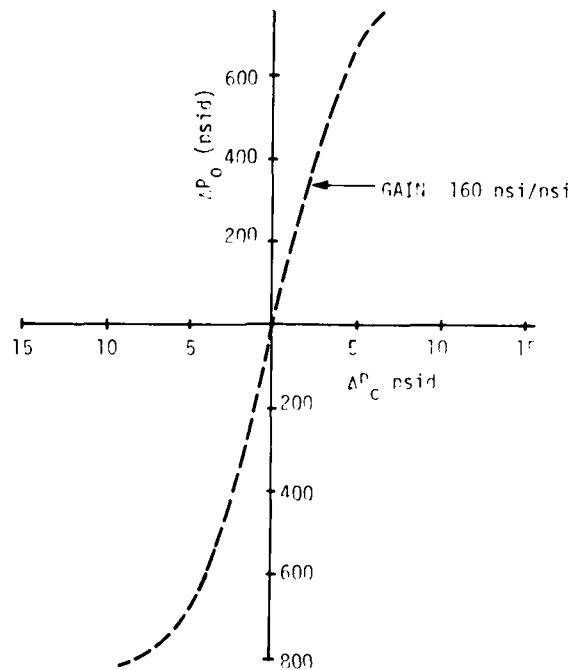


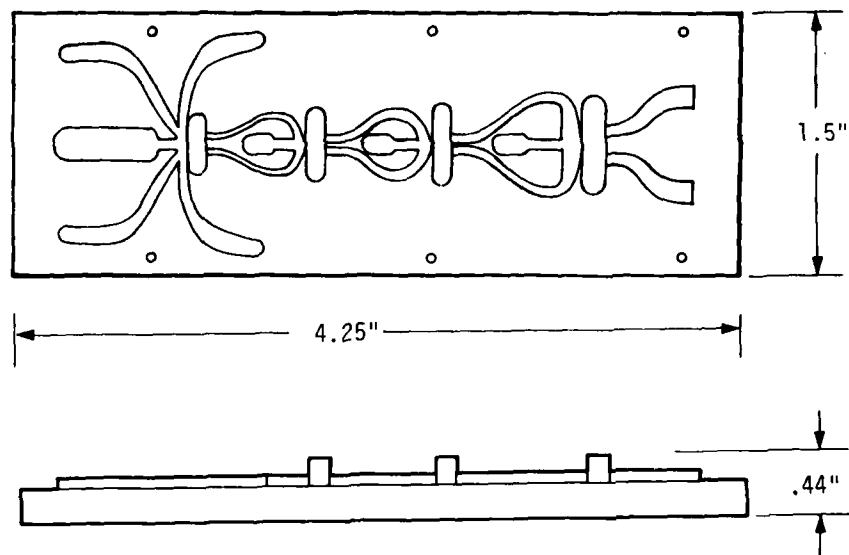
Figure 58. Blocked Actuator Port Pressure Gain, Four-Stage Servocascade at 2000 psi Supply Pressure

For a 0.5 sec mission duration, the oil volume required by the servoactuator is  $12.12 \text{ in}^3$ . For two servoactuators (pitch and yaw), a  $24.24 \text{ in}^3$  volume will be required.

Figure 59 shows a sketch of an electroformed version of the servocascade. The servocascade will be included as a part of the fluidic controller. The actuator and position feedback sensor for the servo loop will be included in the rocket nozzle assembly.

Dynamic Response--The servosystem no-load transfer function can be approximated by the expression:

$$G(s) = \left[ \frac{1}{\left( \frac{d_m}{K_{FB} K_Q} \right) S + 1} \right] \left[ \frac{1}{\left( \frac{\Delta P_o}{\Delta Q_o} \frac{\Delta V}{\beta} \right) S + 1} \right] \frac{\text{rad}}{\text{psid}}$$



NOTES:

1. SERVOCASCADE MOUNTS TO PORTING MANIFOLD CONTAINING SUPPLY, RETURN, OUTPUT, COMMANDS, AND FEEDBACK SIGNAL PORT CONNECTIONS.

Figure 59. Electroformed Four-Stage Servocascade

where:

$G$  = scale factor, rad/psi

$K_{FB}$  = feedback sensor gain, psi/rad

$K_Q$  = servocascade flow gain, cis/psi

$\frac{\Delta P_o}{\Delta Q_o}$  = slope of power amplifier P-Q envelope at average operating point, psi/cis

$\Delta V$  = actuator volume under compression, in<sup>3</sup>

$\beta$  = fluid bulk modulus, psi

The dynamic response will vary from the no-load transfer function depending upon the magnitude of the driven load and the load dynamics. The servoactuator dynamic response will be less than that predicted by the servoactuator no-load transfer function.

A no-load dynamic response prediction is made for a servoactuator with a scale factor of 0.40 deg/psi. This is compatible with the fluidic controller gain. The feedback sensor gain must be 143 psid/rad. Using the pressure gain of 160 psi/psi and flow gain of 1.50 cis/psi and the average actuator displacement of 0.60 in<sup>3</sup>/rad, the transfer function becomes:

$$G(s) = 0.007 \left[ \frac{1}{0.003 S+1} \right] \left[ \frac{1}{0.0032 S+1} \right] \frac{\text{rad}}{\text{psi}}$$

Figure 60 shows a servoactuator closed-loop response plot. This shows a -3 dB bandwidth of about 30 Hz. A description of load dynamics is not available at this time. Based on experience, the loaded servoactuator will have a -3 dB bandwidth of at least 15 Hz with load dynamics.

An estimate of servoactuator small signal tracking accuracy was made. Small signal tracking accuracy will be obtained if the error signal to saturate the servo forward loop is not more than 15 to 20 percent of the signal for full stroke position. This can be expressed as follows:

$$\frac{\Delta P_o}{K_p K_{FB} \theta} = 0.15 \text{ to } 0.20$$

where:

- $\Delta P_o$  = servocascade maximum  $P_o$ , psid
- $K_p$  = servocascade blocked actuator port pressure gain, psi/psi
- $K_{FB}$  = fluidic position feedback sensor gain, psi/rad
- $\theta$  = 1/2 actuator stroke, rad

For our servo, this value is:

$$\frac{800}{(160)(143)(0.349)} = 0.10$$

The servoactuator will have reasonable small signal tracking accuracy. Simulation results indicate that the servoactuator small signal tracking requirement will be easy to meet.

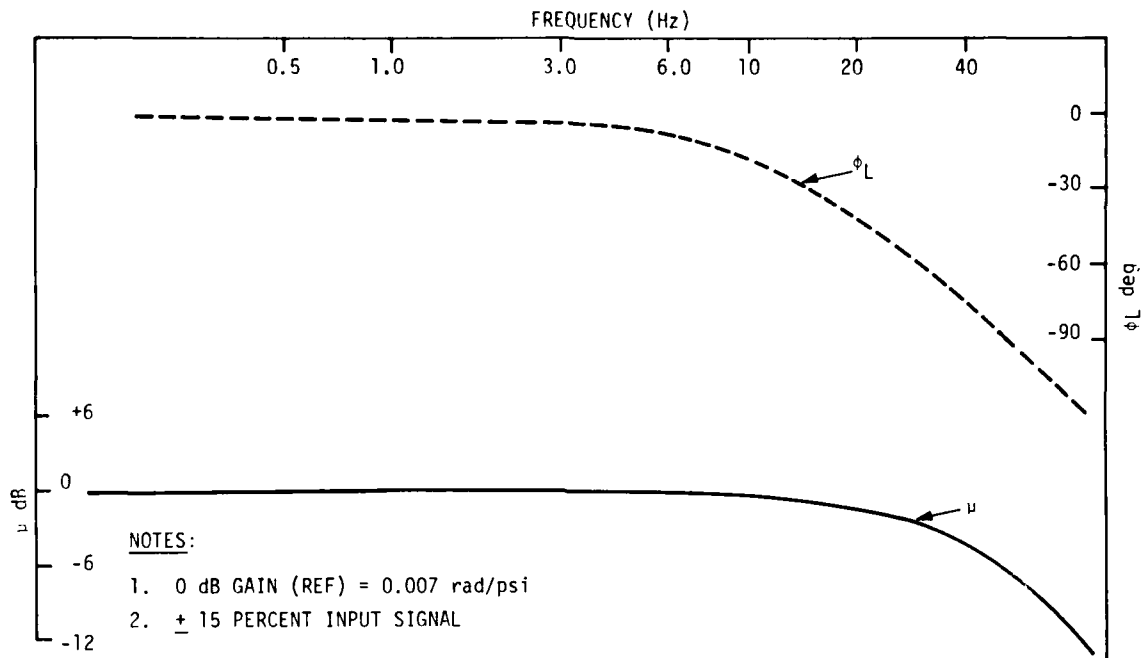


Figure 60. Estimated Dynamic Response--Hydrofluidic Servoactuator

#### HYDRAULIC POWER SUPPLY

The hydraulic power supply for the FTVC is a piston-type accumulator which is pressurized by hot gas. The gas pressure acts against the accumulator to force the hydraulic oil from the accumulator. The FTVC operates with a steady hydraulic flow. It acts as a resistance in the fluid flow path from the source to the exhaust. The hydraulic power source, therefore, is self-regulating.

The accumulator sizing will be determined by the FTVC flow rate, supply pressure, and operating duration. The hot gas pressure and the FTVC supply pressure will be the same value.

### Size Estimate

The yaw and pitch channels of the FTVC have an identical design. The power supply flow rate is twice the single channel flow rate. The power supply size estimate is as follows:

VRS/controller flow rate	1.90 gpm
Servoactuator flow rate	<u>6.29 gpm</u>
	8.19 gpm

For two axes,  $Q_s = 8.19 \times 2 = 16.38$  gpm ( $64.6$  in<sup>3</sup>/sec).

The rocket burn time was given as 0.50 sec. Therefore, the volume of fluid required for 0.5 sec of FTVC operation is:

$$\text{Fluid Volume} = 64.6 (0.5) = 32.3 \text{ in}^3$$

A piston-type accumulator with a 2.5 in inside diameter and a length of 6.5 in will provide the required volume. The estimated size for the accumulator is 2.75 in diameter x 9.0 in length.

### Operating Fluid

Data on high pressure VRS, fluidic controller, and hydrofluidic servoactuator operation indicate that the system will operate successfully over a fluid viscosity range of 7 to 150 centistokes. There is less than 3 dB of gain change within this viscosity range. There is no change in operating performance within a viscosity range of 7 to 50 centistokes.

The FTVC/ball and socket nozzle system will function properly and meet all SOW requirements when soaked at  $-65^{\circ}\text{F}$  or  $+160^{\circ}\text{F}$  and then tested at those temperatures if a fluid is used with low viscosity sensitivity to temperature. A recommended fluid is Dow Corning #510 silicone oil. However, to duplicate the performance of our tests over a temperature range of  $-65^{\circ}\text{F}$  to  $+160^{\circ}\text{F}$ , a modified version of #510 will be necessary. A version of #510 with a viscosity of 12 cs at room temperature should work.

The ball and socket nozzle will have less friction torque at  $-65^{\circ}\text{F}$  than at ambient. The blowout bearing will be filled with a silicone lubricant filled with molybdenum disulfide. The friction torque of the O-rings will decrease because they are harder. Performance at  $+160^{\circ}\text{F}$  is not significantly different from that at  $+70^{\circ}\text{F}$ .

## SECTION 4

### ROCKET NOZZLE AND ACTUATOR DESIGN AND TEST

This section describes the design and performance of the two-axis ball and socket nozzle with its hydraulic actuators. The hydrostatic bearing leads the state of the art in rocket nozzle friction and actuation force. It meets the low power output level of the fluidic servovalve.

#### DESIGN AND PERFORMANCE SUMMARY

The control effector chosen for ejection seat TVC is a solid fuel rocket with a nozzle which can vector 3500 lb of thrust up to 20 deg in two axes. The operating gas pressure is 2000 psi. A hydrostatic bearing was chosen to support the blowout load because of the very low friction level. The total friction is 135 in-lb. The control system will be small due to the low power required to drive the nozzle.

Figure 61 is a photograph of the nozzle mounted to a hydrostatic test base. The nozzle flow passage was not cut out since it was only tested with hydrostatically simulated blowout loads. The actuation pistons are inside the rectangular housing. The pistons rotate the actuator shaft with a crank arm. The actuator shaft rotates the nozzle linkage.

Figure 62 shows cross sections of the hydrostatic bearing and the actuators. The grease trapped between the O-rings supports the ball against the gas blowout load by reaching pressures above 6000 psi. A fluidic position feedback transducer on the actuator shaft puts out a pressure signal proportional to nozzle angle.

The nozzle friction was measured with 1450 psi hydrostatic back pressure under this ball to simulate this 2000 psi dynamic gas pressure. The test simulated ejection conditions by applying this back pressure and the actuator torque within 30 milliseconds after sitting dormant for 24 hours. The initial breakaway torque was 170 in-lb. After the first cycle, this stiction reduced to 135 in-lb or 55 percent above the predicted value. The running friction was only 80 in-lb. These friction levels are about 10 times less than nozzles with carbon or teflon bearings. The actuator O-ring seals contribute 22 percent of the stiction and 28 percent of the running friction.

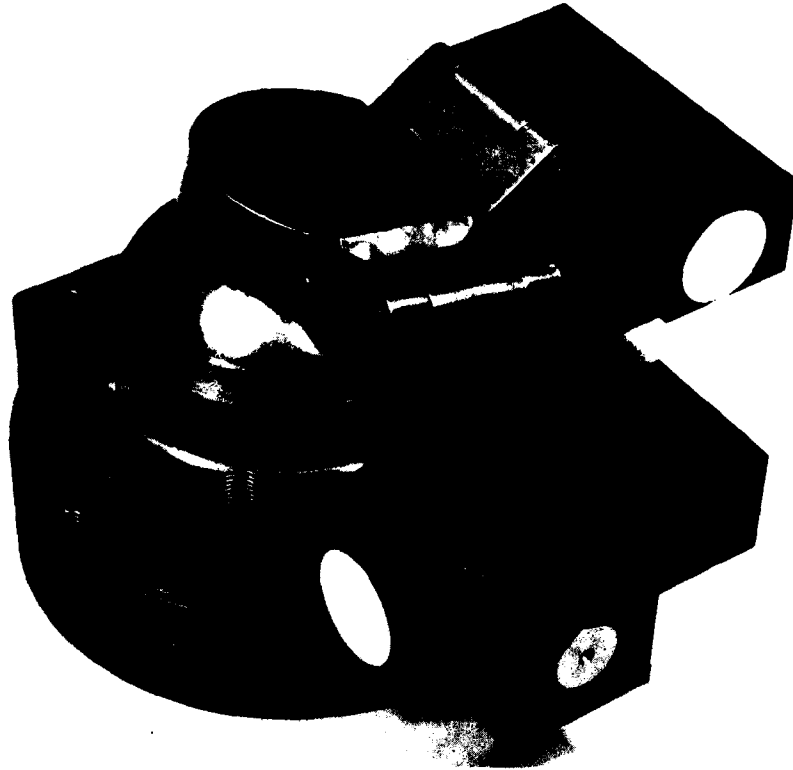


**Figure 61. Nozzle Bearing and Actuator Test Fixture**

The silicone-grease leaks out slowly when operating at 6000 psi. The bearing loses its initial .008 in clearance after about 10 minutes.

The actuator requires 510 psi pressure to produce the 170 in-lb torque. This is well below the 1030 psi maximum pressure available from the fluidic servovalve.

#### **BEARING FRICTION TESTS**

The nozzle actuation force was measured while subjected to a simulated blowout load. Figure 63 shows the hydrostatic pressure test fixture. A pressure of 1450 psi in the fixture base provides the 13,000 lb blowout force the hydrostatic bearing must support. The assembly and test procedure is described below.

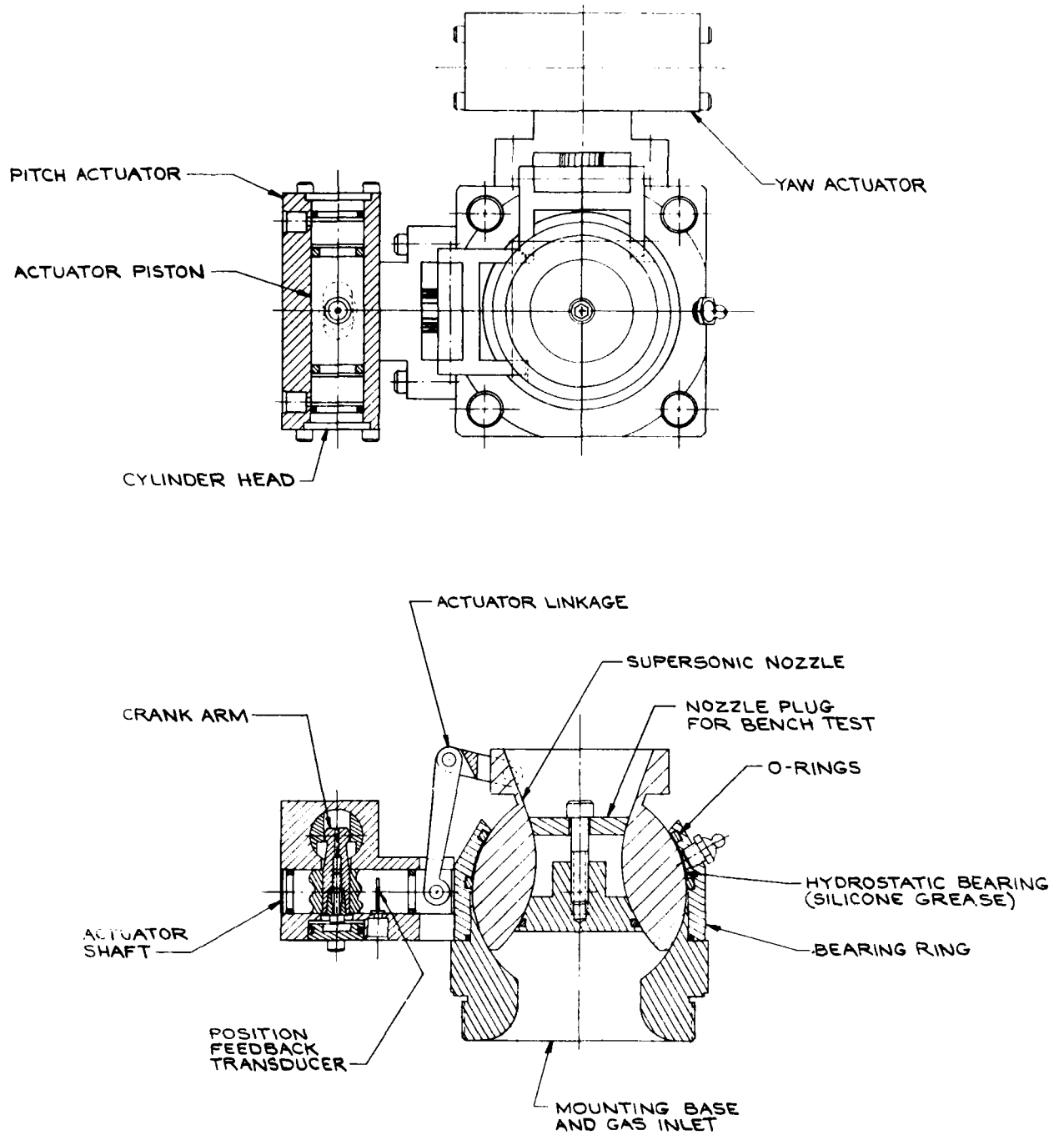


Figure 62. Hydrostatic Ball and Socket Nozzle with Hydraulic Actuators

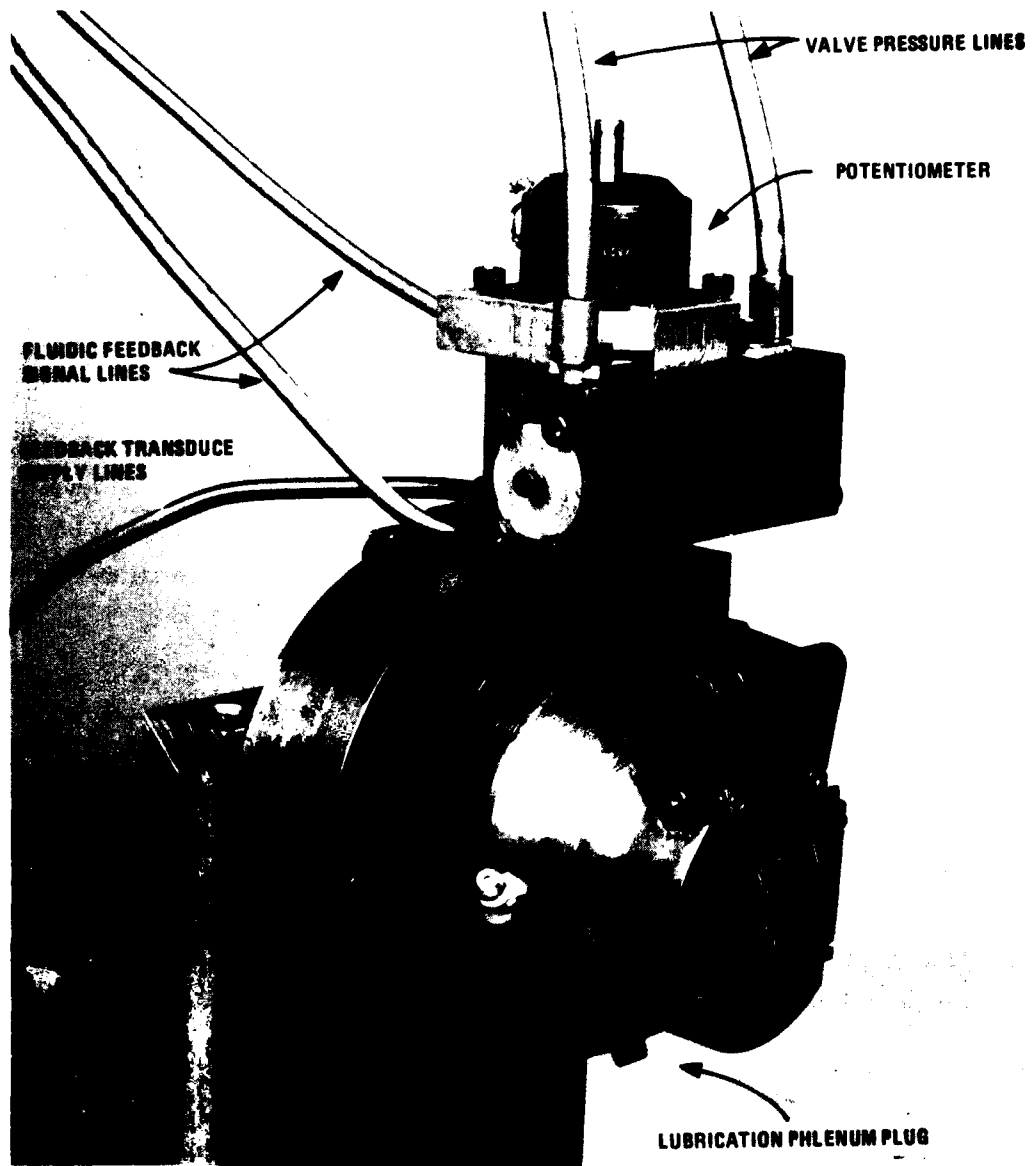


Figure 63. Hydrostatic Bearing Test Fixture

Figure 64 shows a diagram of the instrumentation for the friction test. The solenoid valve on the base hydraulic supply simulates the pressure response of rocket lightoff. The servovalve drives the actuator with a sinusoidal pressure. The actuator pressure and position were recorded with an x-y plotter.

The results of the friction test are shown in Figure 65. The breakaway friction reached 165 in-lb on the initial nozzle cycle. The stiction reduced to 130 in-lb on the second cycle and gradually went down with further cycles. The running friction reduced to 80 in-lb.

Figure 66 shows the friction of the actuator with the nozzle linkage disconnected. Note that the actuator piston seals contribute 28 percent of the friction. This could be reduced at the expense of some leakage.

#### HYDROSTATIC BEARING ASSEMBLY

The position of the ball with respect to the socket is critical to the friction level. This position is controlled by the quantity of grease in the bearing. The ball will bottom out if there is not enough clearance between the ball and socket. The aft O-ring (closest to the nozzle outlet) will extrude if there is too much clearance.

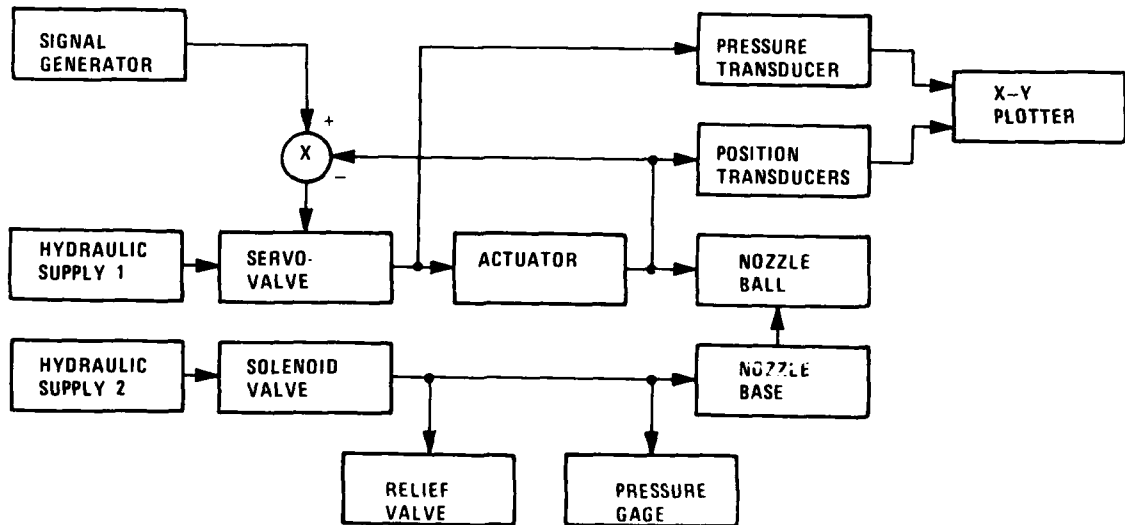


Figure 64. Hydrostatic Bearing Friction Test

THURSDAY 7-5-79 11:05 AM

X = 1V/in. = 200 psid/in.

Y = .5 V/in.

DOW CORNING #3 COMPOUND  
TEFLON-COATED O-RINGS  
BALL .008 INCH FORWARD

TEST #1 FOR 7-6-79

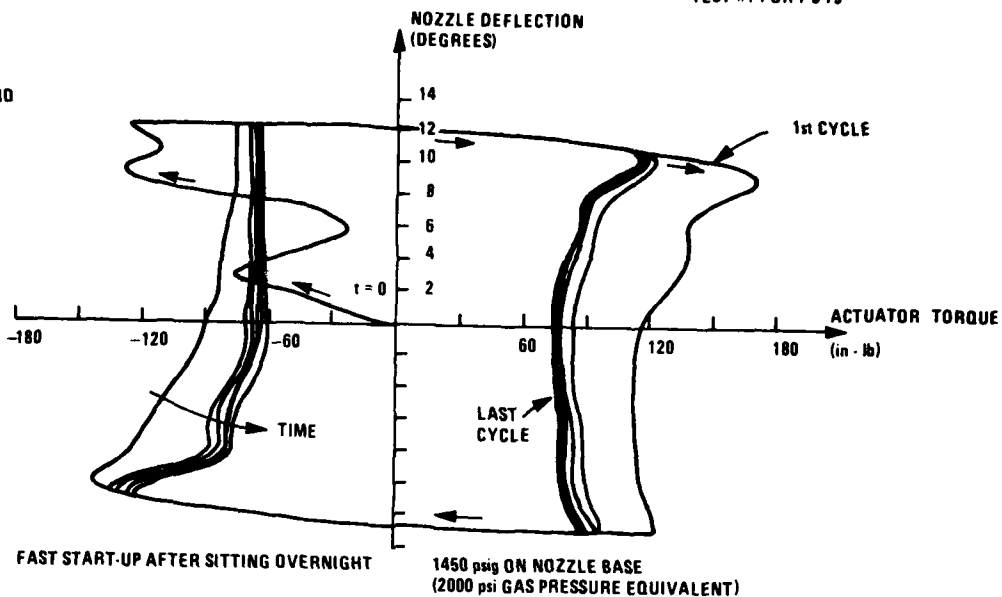


Figure 65. Nozzle Friction Test

TEFLON-COATED O-RINGS  
NO LOAD ON ACTUATOR

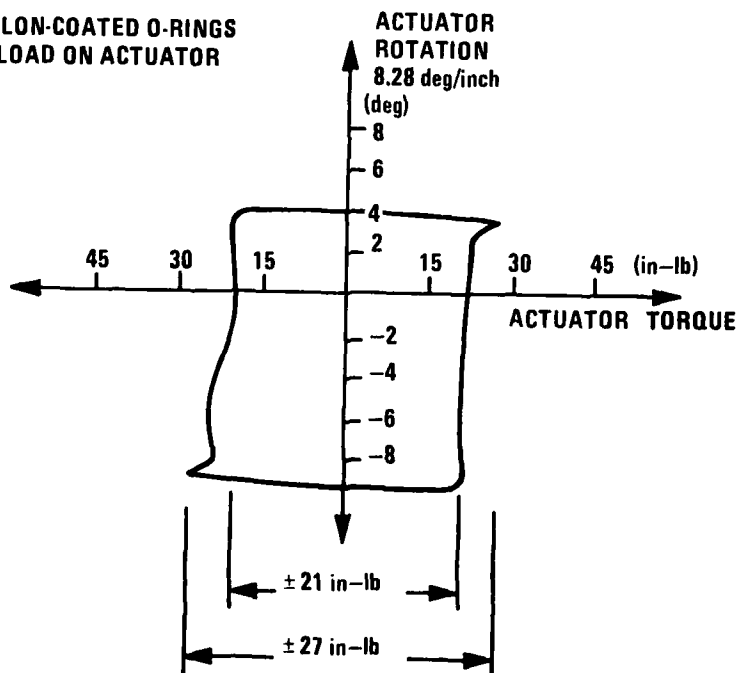


Figure 66. Actuator Piston Seal Friction

A position indicator was used to measure the ball position as the grease was put in the bearing. The grease compressed a predictable amount under pressure. This was accounted for when the grease was installed. The position of the ball under pressure was set at 0.007 in from full aft. The ball moves 0.001 in aft for each 100 psi of base pressure. Therefore, the grease was applied until the ball was 0.021 in from full aft while there was 100 psi on the base. When the 1450 psi was applied, the ball moved to 0.007 in from full aft.

No air can be allowed in the grease cavity because it will compress, causing the ball to bottom out in the socket. The procedure used to assemble the bearing is described in Table 17.

#### HYDROSTATIC BEARING DESIGN

The hydrostatic bearing and nozzle design shown in Figure 61 was configured for light-weight, minimum envelope, and minimum actuation torque. Design compromises were required in the areas of nozzle expansion ratio, actuation torques, and servovalve flow rate requirements. Design analyses were associated, primarily, with bearing friction torques (lubrication and actuator seal friction) and the fluid flow rates required to vector the nozzle at a slew rate of 700 deg/sec. Design areas affecting control port pressure requirements which were not addressed by these analyses include the following:

1. Internal aerodynamic torque--This torque phenomena is a function of the axial displacement of the nozzle throat relative to the equatorial plane of the bearing (pivot point) and the design of the plenum chamber upstream of the nozzle entrance section. Internal aerodynamic torque can be neglected in this design, providing the plenum chamber is designed for uniform gas flow into the nozzle.
2. Position feedback transducer friction--Position feedback transducer design concepts were provided; however, the resistance torques of these devices were not investigated in the nozzle study.
3. Jet damping torque--Classical theory for this phenomena indicates jet damping resistance torque would be less than 1 percent of the predicted lube seal and actuator seal friction torques. It was therefore assumed to be less than the margin of error in areas of primary interest and was ignored.

Table 17. Procedure for Assembling the Hydrostatic Bearing

1. Install lubrication plenum plug and zerk fitting.
2. Pack grease between O-rings and smooth with fingers.
3. Drop ball into socket and attach actuator linkages.
4. Attach base with screws lightly.  
Note: Too much pressure from the base screws causes the aft O-ring to extrude.
5. Remove the lube plenum plug and tighten base screws.
6. Apply 100 psi base pressure to drive ball full aft.
7. Install indicator on ball and set to zero.
8. Install lube plenum plug.
9. Inject lubrication into zerk fitting until ball is 0.021 in forward.
10. Apply 1450 psi base pressure and note ball position (0.007 in).
11. Remove base pressure.

4. Inertial torque--This torque phenomena was ignored because of the low mass of the nozzle and the noncritical perturbation it imposes on the design of the fluidic servocontrol system.

In summary, the lubrication seal static friction torque was predicted to be 57.5 in-lb and the kinetic friction torque to be 51.9 in-lb.

## HYDROSTATIC BEARING ANALYSIS

A hydrostatic bearing was designed to support the hot gas blowoff load with as little friction as possible.<sup>7</sup> The bearing consists of two O-ring seals which trap grease between the ball and the socket. Under load, the seals compress and the ball is supported by the static pressure of the grease. The analysis below shows that a static pressure of 6000 psi will be required to support a load of 13,000 lb. The seal friction force required to turn the nozzle under load is under 60 in-lb. The bearing schematic is shown in Figure 67.

### Seal Pressure

The forces acting on the nozzle are shown in Figure 67. A sum of the forces gives the following equation:

$$F_c + F_t = F_t + F_1 + F_{sc}$$

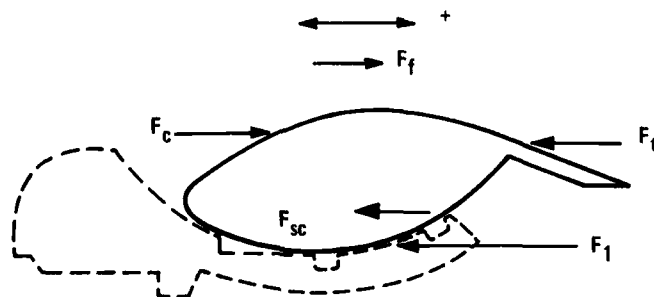


Figure 67. Free-Body Diagram of Axial Forces

<sup>7</sup>T. E. Bolner, "Design Report for Moveable Nozzle for a Seat Ejection Stabilization System," Thiokol Chemical Co., Huntsville, Alabama, January 1977.

where:

- $F_c$  = chamber pressure-induced force
- $F_f$  = drag forces from gas flow through the nozzle
- $F_t$  = exit cone pressure-induced forces
- $F_{sc}$  = aft lubricating seal axial compressive force  
(the forward lubrication seal is in equatorial plane)
- $F_1$  = lubrication pressure-induced force

In previous bearing/nozzle designs, the aft lubrication seal compressive force exceeds the drag forces on the nozzle by an order of magnitude. Typical values for nozzles of this throat diameter, operating at a chamber pressure of 1000 psia, were drag forces of 29 lb and seal compression forces of 525 lb. In this design the seal compression forces are much less in the interest of reducing seal friction (therefore less squeeze on the lubrication seals) to an absolute minimum. In addition, the spherical radius of this bearing is smaller, thereby resulting in a smaller lubrication seal and lower compression forces. It therefore appears reasonable to equate the drag forces in this design, with a chamber pressure of 2000 psia, to the seal compressive forces and assume they cancel each other in the freebody diagram.

The chamber pressure causes blowoff force on the nozzle. This force is balanced (reacted) by the lubrication pressure. If we assume that the pressure in the bearing splitline is equal to the free stream pressure across the entrance insulation, and that this same pressure exists from the nose of the nozzle to the throat plane of the nozzle, we can then calculate the chamber pressure-induced force as follows:

Free stream pressure x axial projected area = chamber pressure force

Free stream pressure = 1826 psia (hot gas), 1788 psia (cold gas)

Axial projected area =  $\pi (r_o^2 - R_t^2) = \pi (1.553^2 - 0.622^2) = 6.361 \text{ in}^2$

where the terms are as defined in Figure 68.

The chamber pressure-induced force is therefore  $\approx 11,610$  lbs (hot gas) and  $\approx 11,373$  lbs (cold gas).

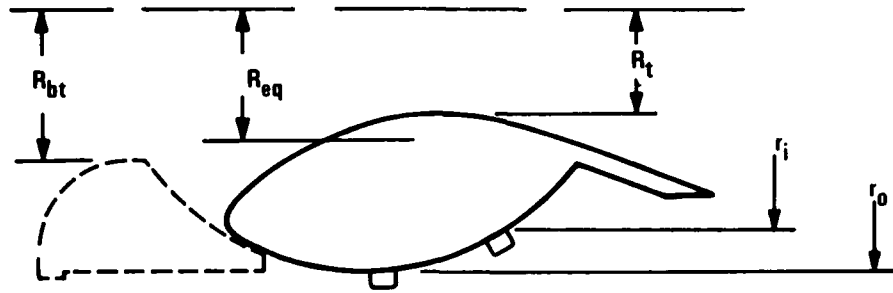


Figure 68. Projected Axial Area Geometry

Summing the chamber pressure forces, we obtain a blowoff force of 12,725 lb for the rocket motor. This force is reacted by a lubrication effective area (axial projected area) of:

$$A_1 = \pi(r_o^2 - r_i^2) = (1.55^2 - 1.33^2) = 1.991 \text{ in}^2$$

Therefore, the lubrication pressure:

$$= 12,725/1.991 = 6391 \text{ psi (hot gas)}$$

$$= 12,488/1.991 = 6272 \text{ psi (cold gas)}$$

### Bearing Friction

The seal friction predicted below is remarkably low. The experimental factor in the design equations was obtained from extensively developed seal design. Factors which influence seal friction are materials, seating, and support ring design. Teflon-coated elastomers have been successful in reducing friction.

The design equation developed for friction calculations is as follows:

$$T_f = (r_s) (k) (A_{LS})$$

where:

$r_s$  = spherical radius of the bearing inner race

$k$  = friction constants derived from experimental data presented in Figure 69. These data are valid for bearing surfaces, lubrication, O-ring materials, and O-ring squeeze and are identical to that in the experimental hardware. The friction constant incorporated in these calculations is based upon this assumption

$A_{LS}$  = lubrication seal footprint (contact area) on the bearing inner race.

Figure 69 is a plot of friction force as a function of lubrication pressure. Breakaway, static, and kinetic friction forces are indicated in these data. For this system we are concerned only with static and kinetic data; breakaway friction forces are generated by aft movement of the inner race during motor ignition. The lubrication seal footprint, in this experimental bearing, was  $6.442 \text{ in}^2$ . Therefore the friction constant ( $K$ ) is derived by reading the friction force value at the predicted design lubrication pressure. This friction force is then ratioed to the lubrication seal footprint of the experimental

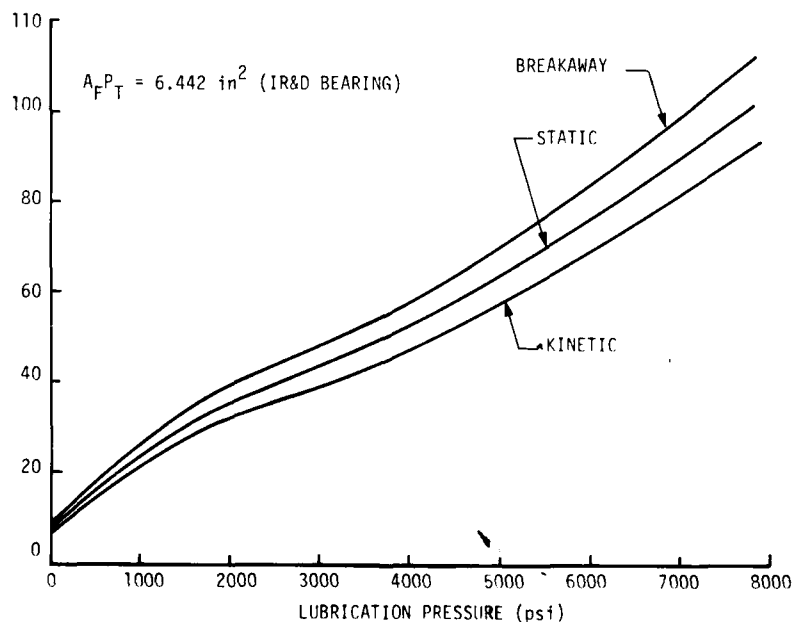


Figure 69. Friction Forces as a Function of Lubrication Pressure

bearing to generate a friction constant in units of pounds per square inch of footprint.  
 For this system the friction constant is calculated as follows:

$$\text{Predicted lubrication pressure} \approx 6400 \text{ psi}$$

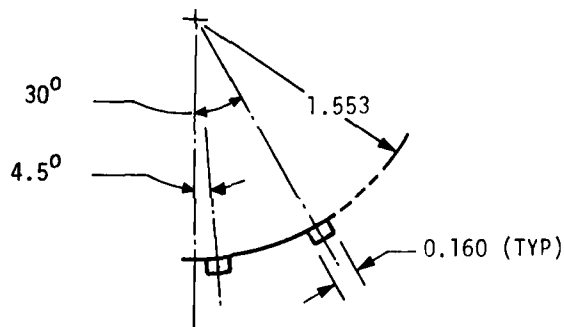
Therefore from Figure 69, the static friction force = 82 lbs and the kinetic friction force = 74 lbs. Then:

$$K_{fs} = 82 / 6.442 = 12.73 \text{ lbs/in}^2$$

$$K_{tk} = 74 / 6.442 = 11.49 \text{ lbs/in}^2$$

The lubrication seal footprint for this system is:

$$\begin{aligned} A_{LS} &= 2 \pi (.160) (1.553) \cos 4.5^\circ + 2 \pi (.160) (1.553) \cos 30^\circ \\ &= 1.556 + 1.352 = 2.908 \text{ in}^2 \end{aligned}$$



The lubrication seal friction torque is then calculated as follows:

$$T_{ts} = (1.553) (12.73) (2.908) = 57.5 \text{ in-lb force}$$

$$T_{tk} = (1.553) (11.49) (2.908) = 51.9 \text{ in-lb force}$$

## ACTUATOR DESIGN

The actuator shown in Figure 70 must match the load torque and speed requirements with the servovalve pressure and flow output. The displacement of the actuator was chosen to be  $0.3 \text{ in}^3/\text{rad}$  as a compromise between small actuator size and maximum torque level.

Figure 71 shows the maximum power curve required by the load. The operating point chosen for the actuator is:

Actuator Displacement:	$D = 0.3 \text{ in}^3/\text{rad}$
Required Slew Rate:	$\dot{\theta} = Q/D = 12.2 \text{ rad/sec (700}^\circ/\text{sec)}$
Required Flow Rate:	$Q = 3.66 \text{ in}^3/\text{sec}$
Required Torque:	$T = \Delta PD = 150 \text{ in-lb}$
Required Pressure:	$\Delta P = 500 \text{ psi}$
Maximum Stall Torque:	$T_m = 309 \text{ in-lb}$
Maximum Slew Rate:	$\dot{\theta}_m = 21.67 \text{ rad/sec (1241}^\circ/\text{sec)}$

@  $T = 80 \text{ in-lb}$

The actuator could have been bigger and still meet the slew rate requirement. That would allow more stall torque margin to allow for unexpected friction loads. The smaller size was chosen for space considerations. This design has a stall torque margin of 106 percent. Torque margin is necessary in high friction loads to prevent jitter. Jitter occurs when a large error signal is required to drive the output valve to full torque. High feedback gain also reduces jitter.

## ROCKET MOTOR DESIGN

Two rocket motor configurations were designed to produce 3500 lb thrust. The first is 2.75 in diameter and 36 in long to fit on the back of the seat. The second is 5.5 in diameter and 9 in long to fit on the bottom of the seat. Both use low energy propellant to keep temperatures and pressures down. Low temperature and pressure reduce the adverse effects of erosion and blowout load on the manifold and nozzle.

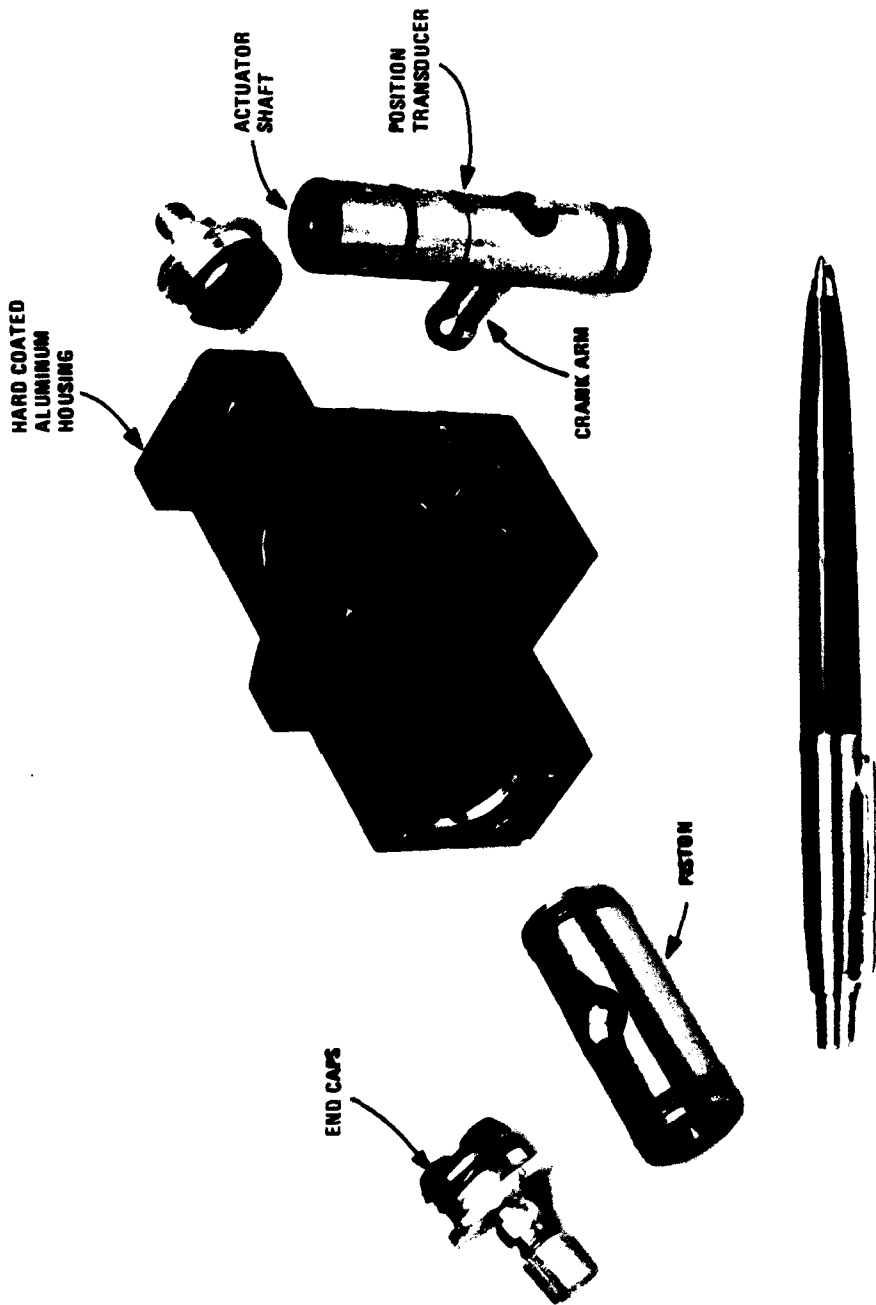


Figure 70. Rocket Nozzle Actuator

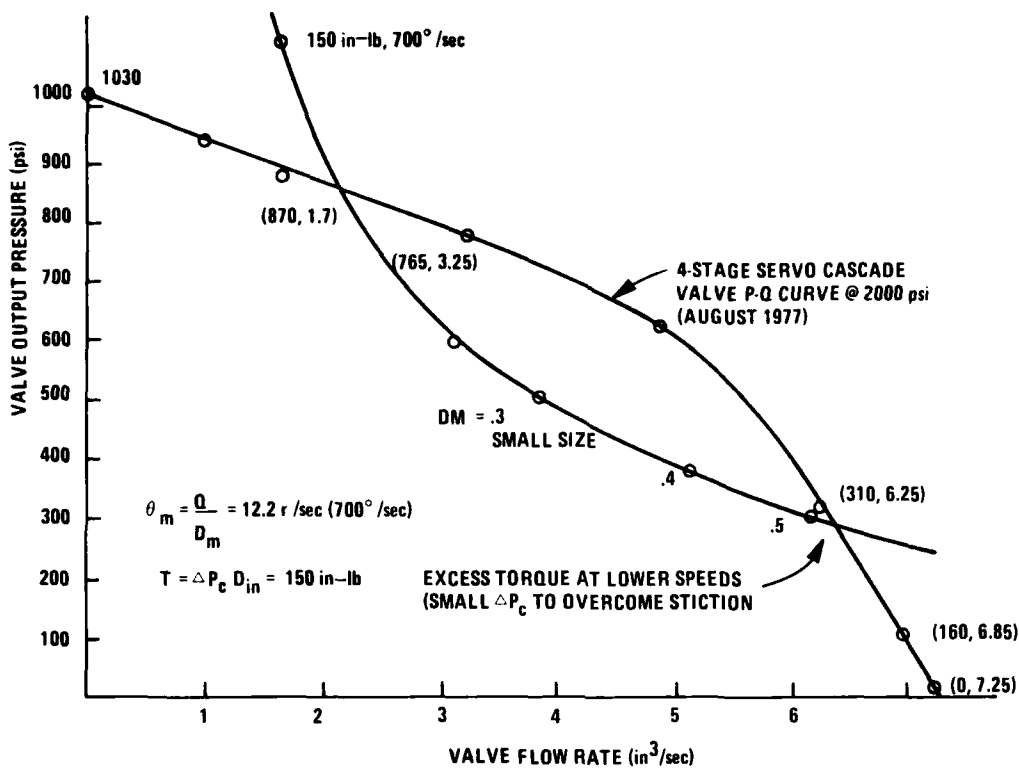


Figure 71. Actuator Displacement Selection

The detailed design parameters for both motors are listed in Tables 18 through 21. Their thrust and pressure histories are shown in Figure 72. Figure 73 is a design curve which shows how the total impulse and propellant might vary with grain length for the 5.5 in diameter motor. Table 18 describes the motor performance parameters. The 2.75 in motor uses slightly higher energy propellant. It uses less propellant and burns at 5 percent higher pressure. Table 19 lists their dimensions, weights, and material, and Table 20 describes the sea level ballistics. Note the specific impulses of 228 and 212, respectively. Table 21 describes the properties of the two propellants.

Table 18. Motor Performance Parameters  
(at Sea Level and 70° F)

Parameter	2.75 in motor	5.5 in motor
Web Burning Time, sec	0.500	0.500
Average Thrust, lb	3500	3500
Average Pressure, psia	2100	2000
Web Impulse, lb-sec	1750	1750
Total Impulse, lb-sec	1750	1941

Table 19. General Specifications

Parameter	2.75 in motor	5.5 in motor
<u>Dimensions, in</u>		
Propellant Grain Length, in	35.6	*
Outside Diameter	2.75	5.500
<u>Weigh.s, lb</u>		
Propellant	7.63	9.13
Chamber	*	*
Nozzle	*	*
Nozzle Adapter	*	*
Liner and Insulation	*	*
Igniter	*	*
Attachments	*	*
TOTAL WEIGHT	*	*
<u>Propellant Geometrical Parameters</u> (Configuration--Case Bonded, Internal Burning, C.P. W/3 Longitudinal Slots)		
Propellant Outside Diameter, in	2.574	5.214
Volumetric Loading Density, percent	0.677	*
Web Fraction	0.450	0.207
Geometrical Web Thickness, in	0.579	0.539
Nominal Liner Thickness, in	0.010	0.010
Average Burning Surface/Throat Area	189.9	204.4
Length Average Port Area/Throat Area	1.692	2.60
<u>Chamber</u>		
Material	Aluminum, 7075-T6	
Ultimate Uniaxial Strength, psi	76,000.	76,000.
Specific Weight, lb/in <sup>3</sup>	0.10	0.10
Nominal Thickness, in	0.078	1.33
Minimum Thickness, in	0.073	0.128
Maximum Expected Operating Pressure (MEOP), psia	2,706.	2,359.
Hydrostatic Test Pressure, psia	2,976.	2,595.
Burst Pressure, psia	4,060.	3,539.
Hydrotest Pressure/MEOP	1.10	1.10
Burst Pressure/Hydrotest Pressure	1.36	1.36
Burst Pressure/MEOP	1.50	1.50
<u>Nozzle</u>		
<u>Geometry</u>		
Type (THIOVEC)	Moveable	Moveable
Expansion Section Configuration	Conical	Conical
Number of Nozzles	One	One
Throat Diameter, in (initial)	1.204	1.244
Exit Diameter, in (initial)	2.250	2.250
Throat Area, in <sup>2</sup> (average)	1.138	1.215
Expansion Ratio (average)	3.493	3.271
<u>Insert</u>		
Material	Graphite ATJ	Graphite ATJ

\* Not calculated

Table 20. Ballistics (at Sea Level)

Parameter	2.75 in motor	5.5 in motor
Average Thrust, lb		
40°F	3253	3395
70°F	3500	3500
100°F	3766	3608
Average Pressure, psia		
40°F	1954	1941
70°F	2000	2000
100°F	2257	2061
Maximum Expected Instantaneous Pressure, psia		
100°F ( $\frac{3}{P} = 0.09$ )	2706	2359
Web Burning Time, sec		
40°F	0.537	0.514
70°F	0.537	0.500
100°F	0.466	0.486
(1) Thrust Coefficient, $C_F$		
40°F $m$	1.462	1.439
70°F	1.464	1.440
100°F	1.466	1.440
(2) Propellant Specific Impulse, lb-sec/lb		
40°F	228.6	212.05
70°F	229.2	212.48
100°F	229.8	212.90
Total Impulse, lb-sec		
40°F	1745	1937
70°F	1750	1941
100°F	1755	1945

(1) Assumed Average Thrust Efficiency Factor,  $C_m = 0.960$   
 Divergence Loss Factor,  $N = 0.970$

(2) Assumed Pressure Decay Loss Factor,  $C_{TO} = 1.00$

Table 21. Properties and Ballistics of TP-H8239 Type Propellant at 70°F

Parameter	2.75 in motor	5.5 in motor
Characteristic Velocity, $c^*$ (ft/sec)	5037	4865
Specific Weight, $\delta_f$ , (lb/in <sup>3</sup> ), effective	0.061	0.060
Temperature Coefficient of Pressure, $K' ( / ^\circ\text{F})$	0.240	0.100
Temperature Coefficient of Burning Rate, $K' ( / ^\circ\text{F})$	0.235	0.095
Ratio of Specific Heats,	1.161	1.22
Burning Rate Equation, $r = a_t P_c^n$	$0.02168 (P_c)^{.52}$	$0.0839 (P_c)^{0.336}$
Burning Rate at 1000 psia, in/sec	0.787	0.855

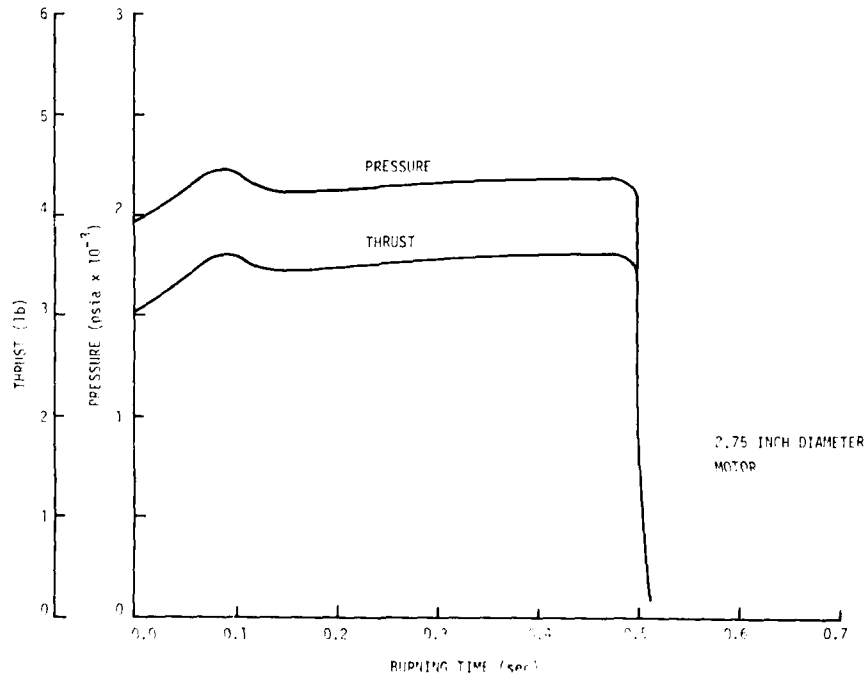


Figure 72. Pressure and Thrust versus Time at Sea Level and 70°F

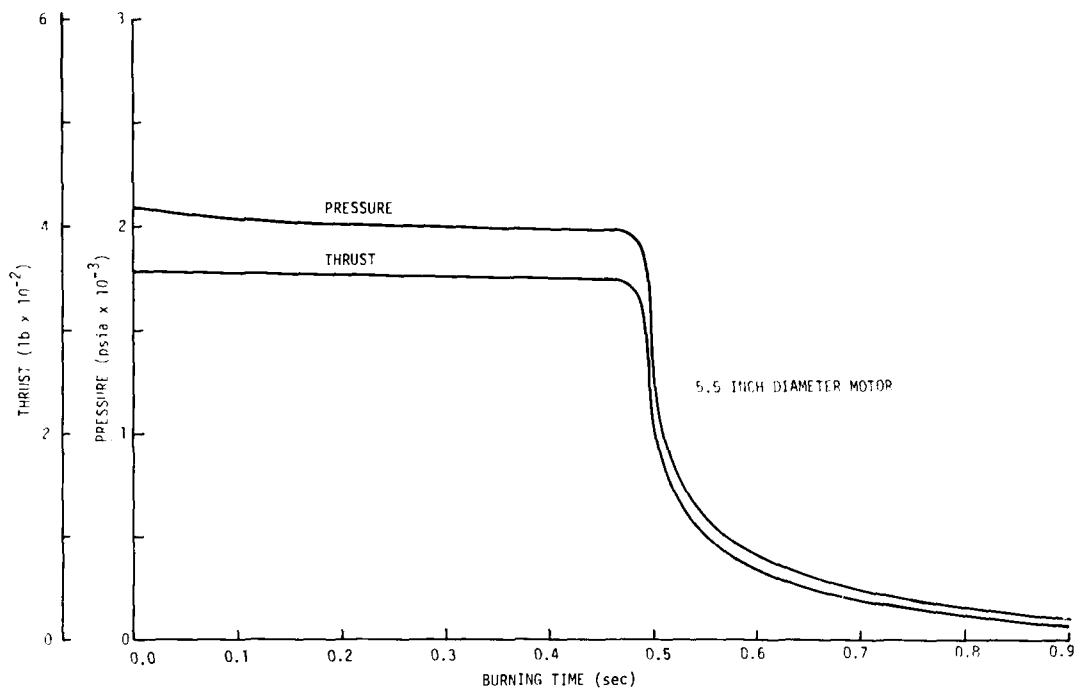


Figure 72. Pressure and Thrust versus Time at Sea Level and 70°F (concluded)

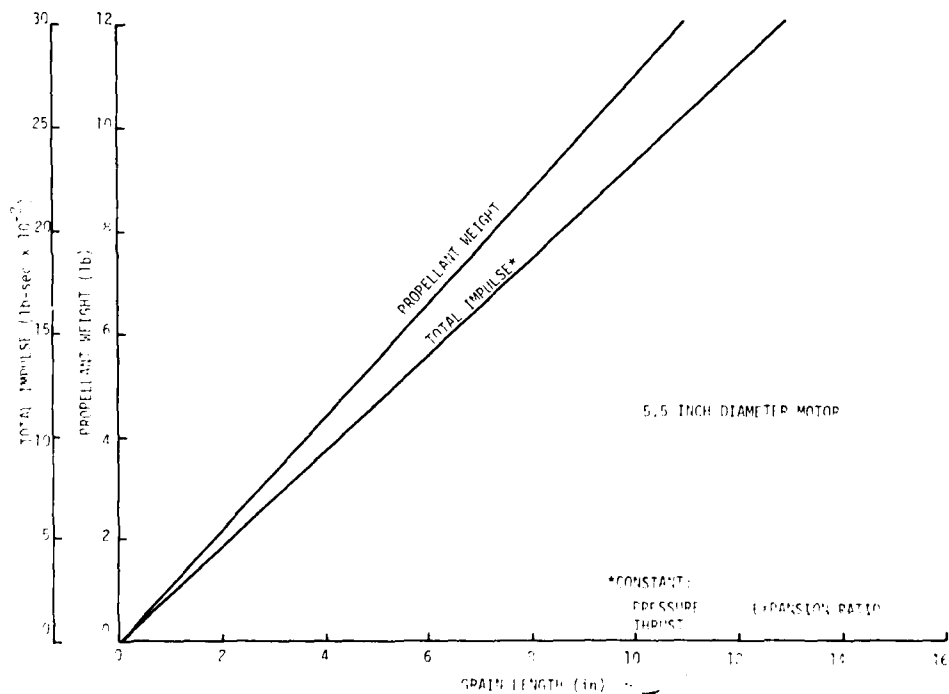


Figure 73. Propellant Weight and Total Impulse at 70°F versus Grain Length

## SECTION 5

### ESCAPE SYSTEM FLIGHT SIMULATOR

We developed an escape system flight simulator to measure the transient response of the control system. The simulator duplicates the pitch or yaw attitude transient of a seat flight. The objective was to duplicate the nozzle transient response obtained from the 6 DOF SAFEST computer simulation.

#### SIMULATOR DESCRIPTION

Figure 74 shows the flight simulator and its hydraulic power supply. Its components include a precision servo table, hydraulic power supply, solenoid valve, and digital controller. The servo table is designed to produce over 400 ft-lb of torque at 1000 deg/sec to duplicate the large acceleration that a seat experiences in high-speed ejection. The solenoid valve is designed to turn on the hydraulic power as quickly as a rocket lighting off. The digital controller is programmable to deliver any attitude history. The digital controller can also be replaced by an analog signal generator or servo-analyser to perform frequency response analysis. A block diagram illustrating the test setup is shown in Figure 75. The FTVC system and rocket are mounted on the rate table with the input axis of the channel to be tested aligned with the table output axis. A 30 gpm hydraulic test bench powers both the rate table and the FTVC system. A high-speed solenoid valve in the FTVC supply line simulates the time delay between ejection initiation and rocket ignition. The signal to open it comes from the digital controller.

The digital controller also drives the rate table to simulate seat trajectories. The controller is programmed to command seat attitude as a function of time. The trajectory can be changed by reprogramming the controller.

Position transducers attached to the rate table and rocket nozzle measure table motion and nozzle position during the tests. These signals are recorded by a multi-channel strip chart recorder.

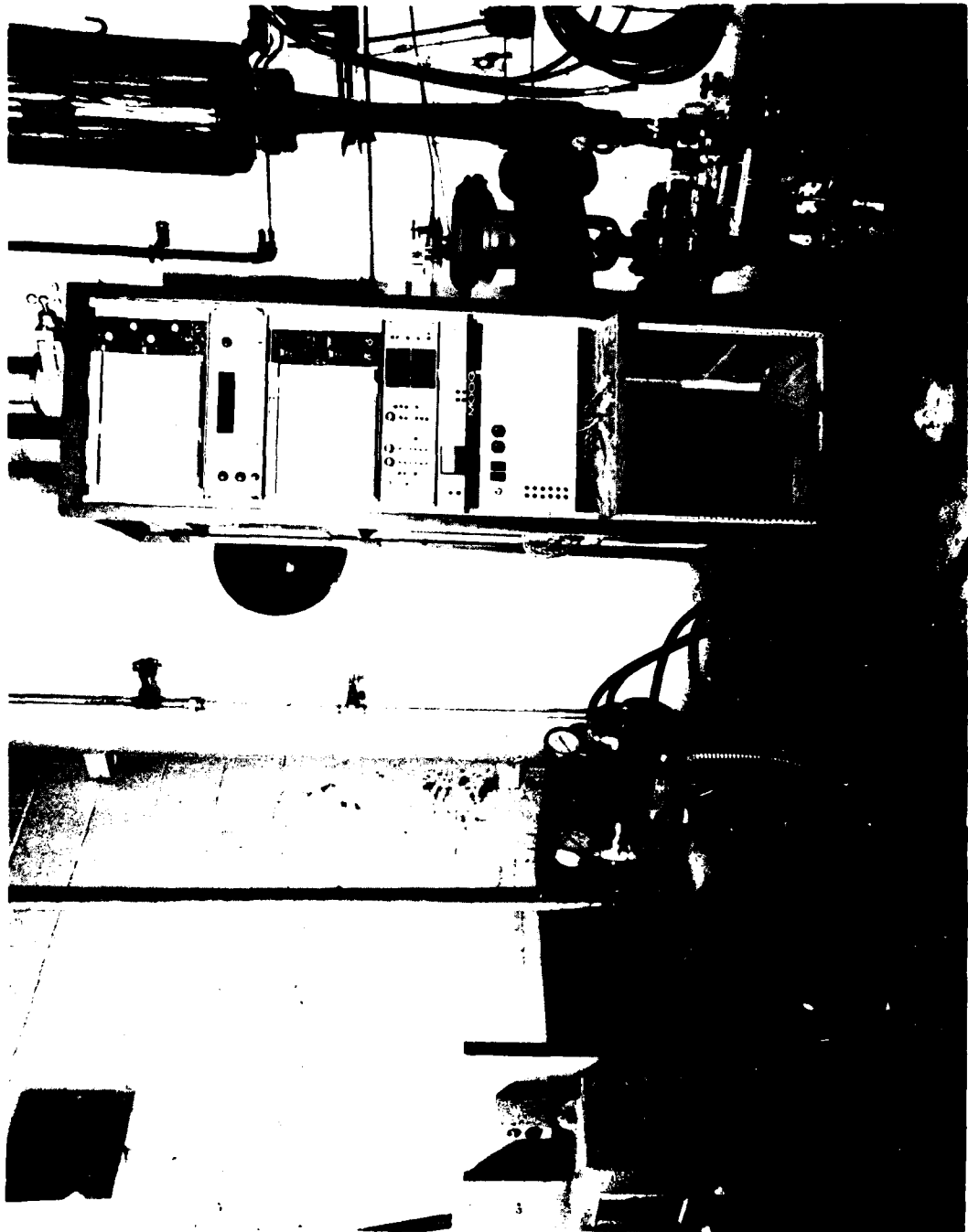


Figure 74. Escape System Flight Simulator

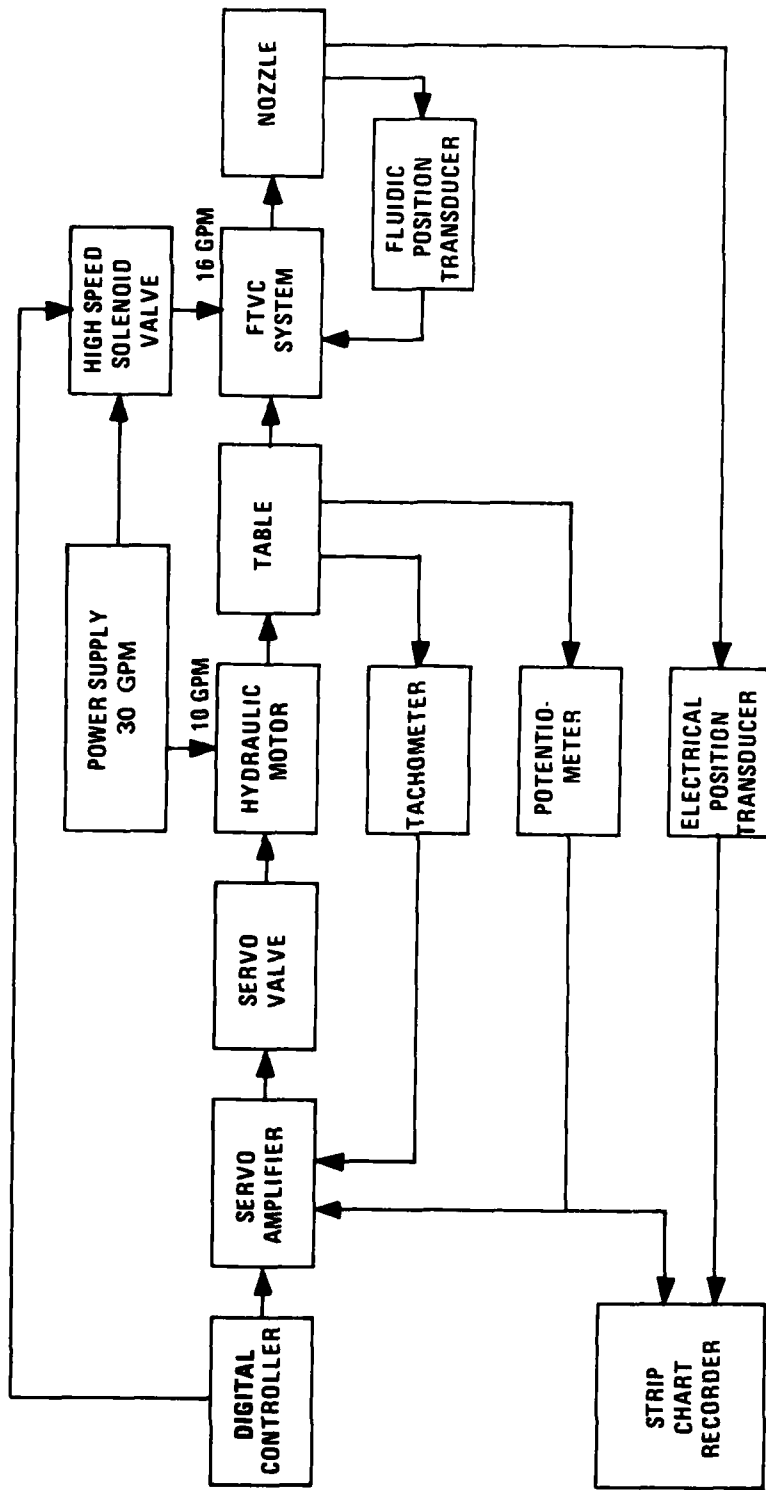


Figure 75. Simulated Escape Test System Diagram

## ESCAPE SYSTEM SIMULATION DESCRIPTION

The FTVC system is mounted on the testbed with the pitch input axis aligned with the table output axis. The attitude bias is set to 60 deg. The analog controller is programmed with the low-speed pitch attitude trajectory shown in Figure 76.

The FTVC initialization flag in the controller is set to open the supply solenoid valve at the time indicated. The nozzle bearing is pressurized to 1450 psi to simulate hot gas blowout load. After the run is complete the controller is reprogrammed with the high-speed pitch attitude trajectory shown in Figure 76 and the test repeated.

The FTVC system is reoriented on the testbed so that the yaw input axis is aligned with the table output axis and the test repeated using the yaw attitude trajectories shown in Figure 77.

The FTVC system must duplicate the nozzle trajectories obtained from computer simulation. The maximum allowable error at any time is  $\pm 2$  deg.

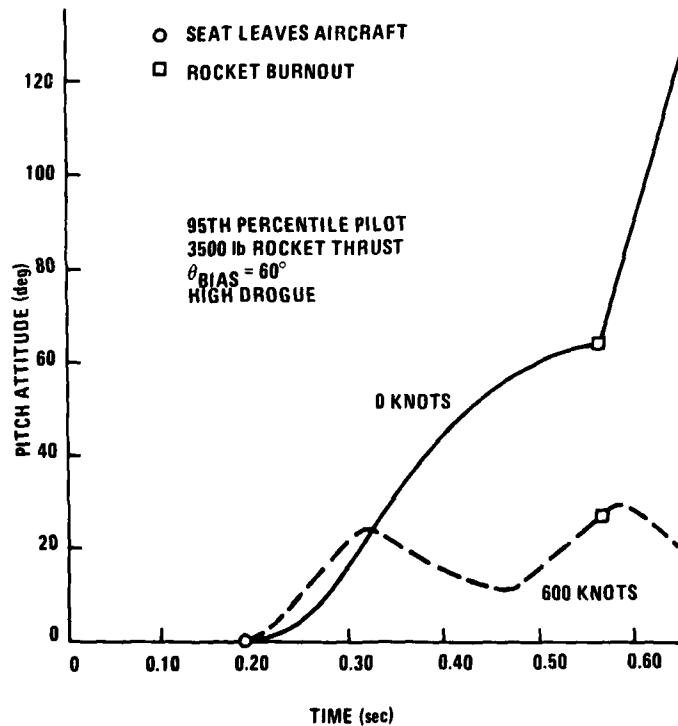


Figure 76. Pitch Attitude Trajectories

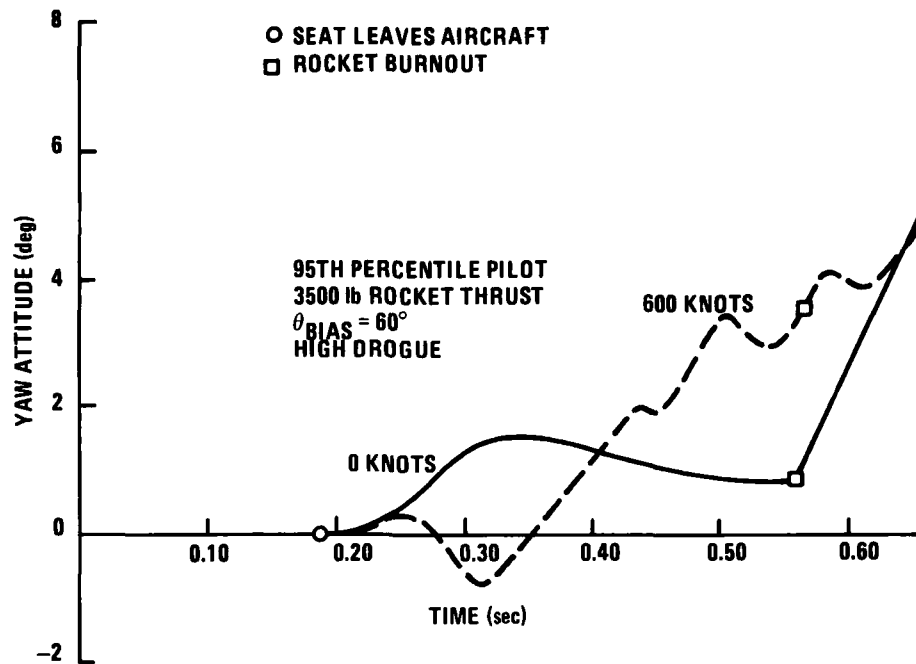


Figure 77. Yaw Attitude Trajectories

#### PRECISION SERVO TABLE

We developed a precision servo table to perform frequency response and transient response tests for the seat control system. It is designed to develop high torque and speed to duplicate the transient seat rotation during high-speed ejections. Its dynamic response had to be faster than the fluidic control system so it would not influence the latter's transient response.

The servo table is shown in Figure 78. Its components include a rotary actuator, pressure control servovalve, potentiometer, and tachometer. The table and its power supply are described in Figure 79. Figure 80 is a schematic of the hydraulic power supply.

Table 22 lists the performance specifications of the servo table. The dynamic response data is shown in Figure 81.

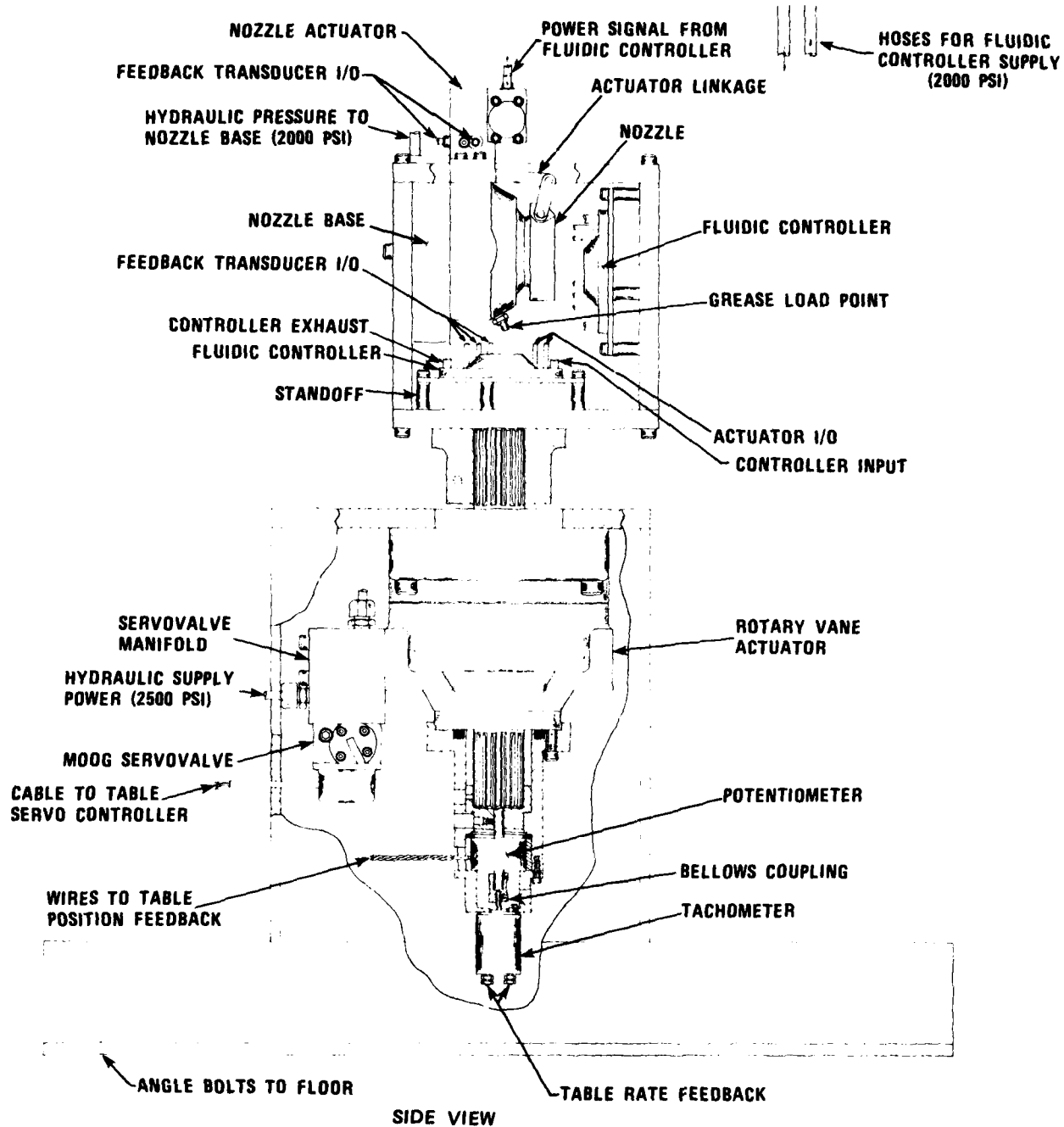


Figure 78. Hydraulic Rate Table for Fluidic Controller Tests

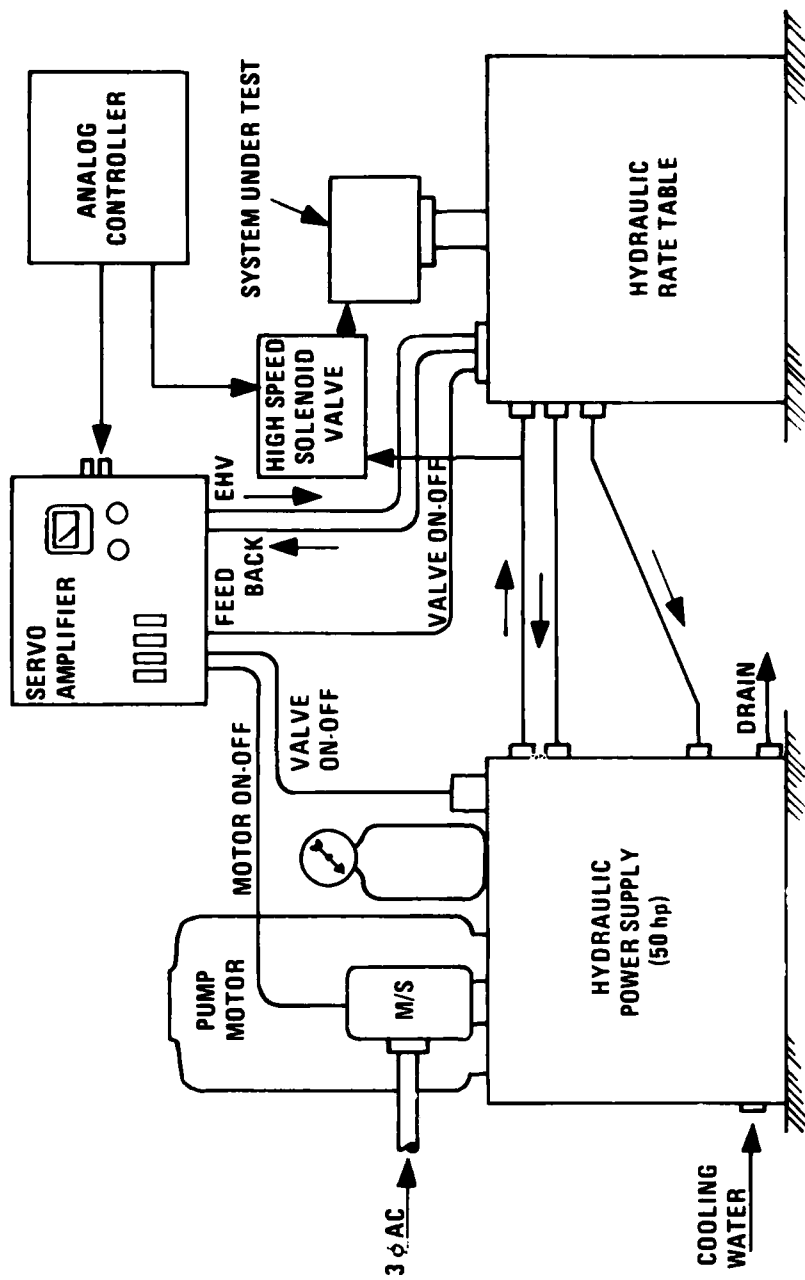


Figure 79. Hydraulic Rate Table Power and Control System

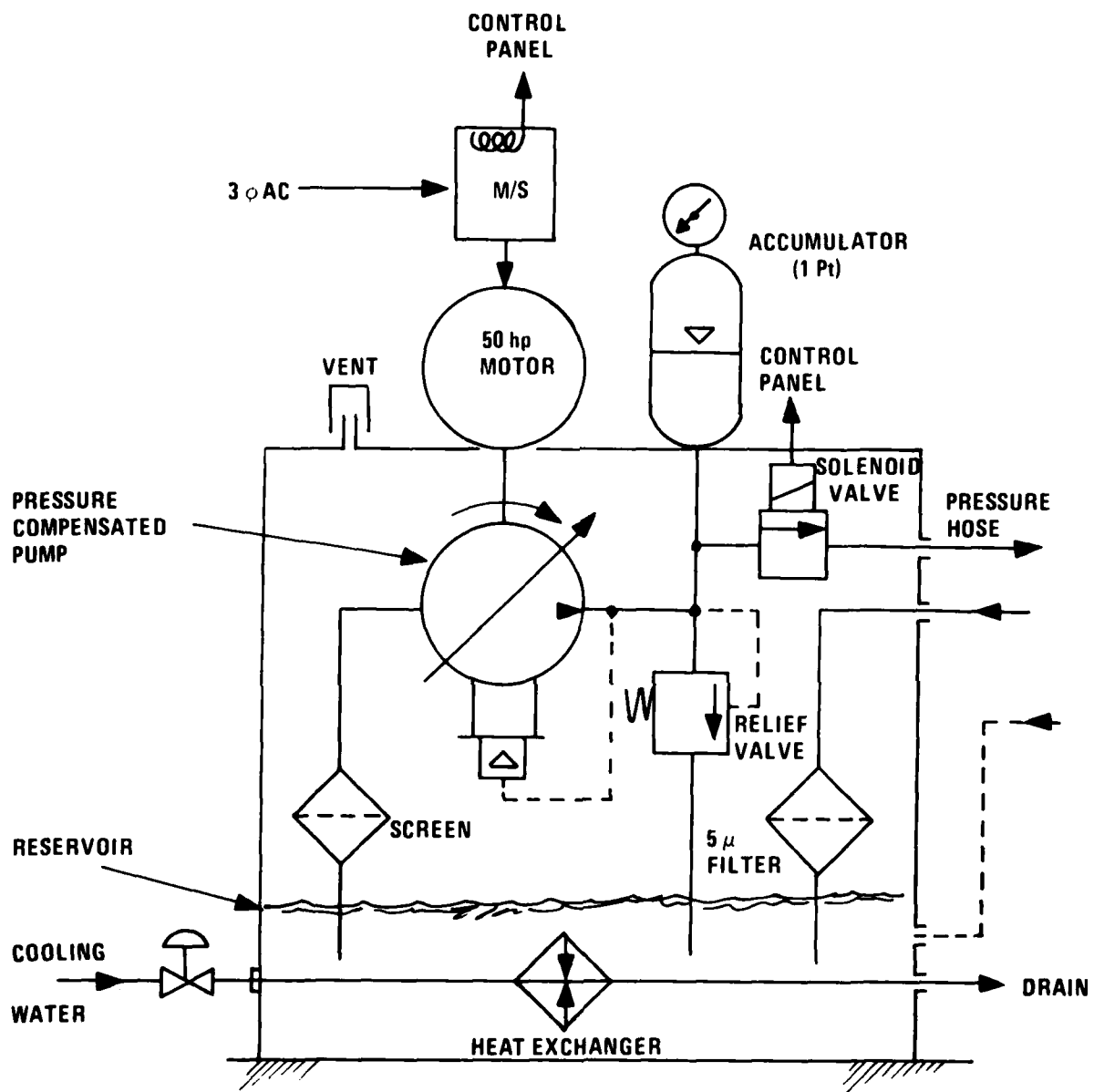


Figure 80. Hydraulic Power Supply

Table 22. Precision Servo Table Performance Specifications

	Required	Capability
Maximum Torque (ft-lb)	350	477
Maximum Speed (deg/sec)	1000	1500
Maximum Power (ft-lb, deg/sec)	350 @ 500	350 @ 900
Bandwidth (Hz)	15	16
Attitude Precision (deg)	1/2°	1/3°
Maximum Supply Pressure (psi)	2200	3000
Maximum Flow Rate (cis)	----	55
Actuator Displacement (in <sup>3</sup> /rad)	----	1.91

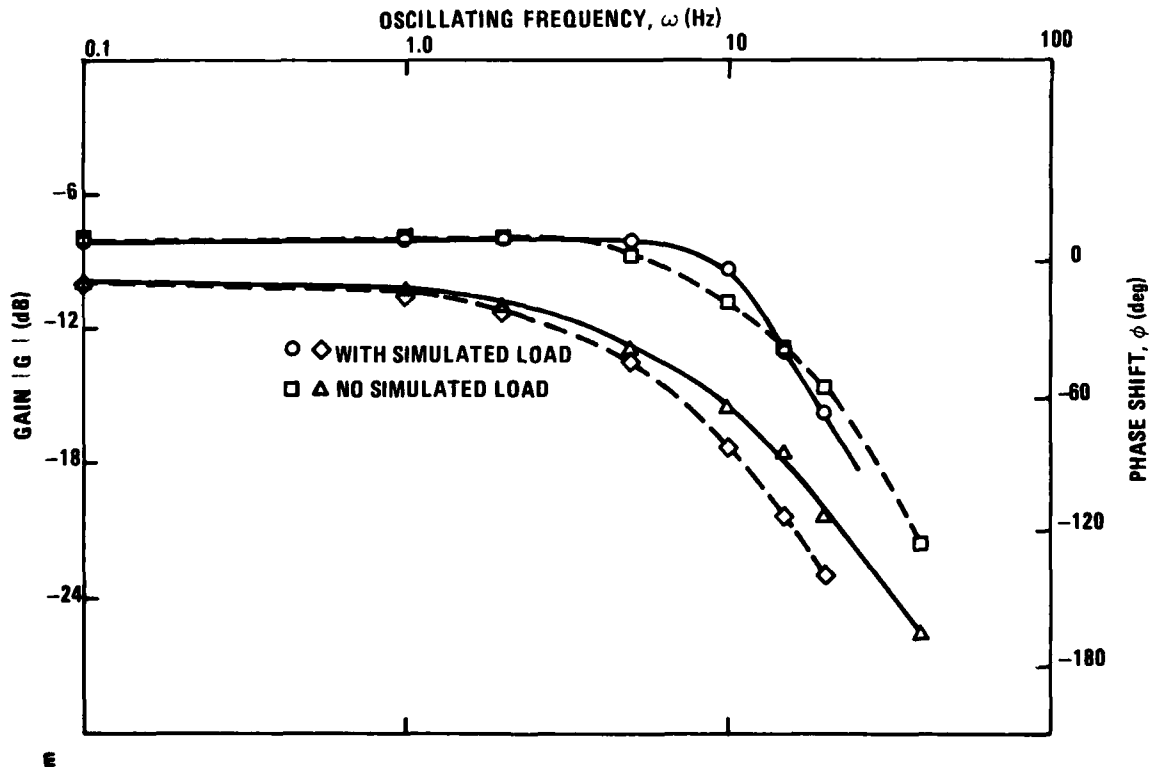


Figure 31. Table Frequency Response

## DIGITAL CONTROLLER

We used an IASIS 7301 computer to command the servotable with programmed seat trajectories. The computer program and seat trajectories were stored on cassette tape. The operation of the controller and the programs are described in a users guide.\* The signal generator commands the table servoamplifier and the hydraulic supply solenoid valve to simulate a seat ejection sequence. The solenoid valve simulates the power supply initiation of the solid fuel rocket.

---

\* Ron Reitan, "FTVC Digital Signal Generator Users Guide"  
Honeywell Memorandum, November 1978.

## SECTION 6

### CONCLUSIONS

A two-axis TVC system has definite benefits for ejection seats. The 90 percent reduction of yaw angles will significantly reduce pilot injury at higher speed and reduce line entanglement at all speeds. Sixty percent reduction of pitch rates will also improve g loads by keeping them away from the spinal axis. Trajectory height is improved at low speed because the seat is stabilized with the rocket thrust near vertical during rocket burn.

The hydrofluidic control system is ideally suited for the ejection seat application because it is small, reliable, and requires no maintenance. The large power consumption of fluidic components is not important because of the short mission. The fluidic rate sensor is the most advantageous component since it is not delicate and can start up faster than any other rate sensor.

The full advantage of TVC is not utilized because of the fast chute deployment. A vertical seeking TVC can handle high sink rates with much less altitude. The system designed above can seek vertical by interfacing a vertical sensor with an attitude reference.

The ability of the control system to stabilize the seat at high speed was limited by the large aerodynamic torque at zero angle of attack. The drogue chute tries to hold the seat at zero angle of attack where the pilot can take the most g's. However, because the seat has more surface area below the cg, the seat wants to pitch forward and hence fights the drogue. If the seat could be designed with zero aerodynamic torque at zero angle of attack, the system would be much more stable.

Electroforming integrated circuits is a low-cost production process once the mold has been perfected. However, component modifications during research and development are more costly. Separately electroformed amplifiers are more flexible during development programs.

Temperature sensitivity is a major problem with all fluidic systems. System development should include efforts to develop an oil with lower viscosity sensitivity to temperature.

## REFERENCES

1. R. B. Beale, "Fluidic Thrust Vector Control for the Stabilization of Man/Ejection Seat Systems," AFFDL-TR-75-105, Honeywell, Inc., Minneapolis, Minnesota, September 1975.
2. I. L. Clinkenbeard and E. O. Cartwright, "Study and Design of an Ejection System for VTOL Aircraft," AFFDL-TR-70-1, Air Force Flight Dynamics Laboratory, Wright-Patterson Air Force Base, Dayton, Ohio, May 1970.
3. H. R. Moy, "Advanced Stabilized Ejection Seat Development Program," SEG-TR-67-51, Aeronautical Systems Division, AFSC, Wright-Patterson Air Force Base, Dayton, Ohio, January 1968.
4. Darroll Bengston, Thomas Dickovich, and Robert Helfenstein, "Roll-Axis Hydrofluidic Stability Augmentation System Development," USAAMRDL-TR-75-43, Honeywell, Inc., Minneapolis, Minnesota, September 1975.
5. Military Specification MIL-S-9479B(USAF), General Specification for Aircraft Upward Ejection Seat Systems, March 1971.
6. R. V. Burton and R. B. Beale, "Development of a Hydrofluidic Vernier Rocket Control System for Ejection Seat Stabilization," NASC N00019-C-0374, Honeywell, Inc., Minneapolis, Minnesota, December 1976.
7. T. E. Bolner, "Design Report for Moveable Nozzle for a Seat Ejection Stabilization System," Thiokol Chemical Co., Huntsville, Alabama, January 1977.